

Numerical Hydrodynamic Modelling of the Derwent Estuary

Final Report

M. Herzfeld, J. Parslow, N. Margvelashvili, J.R. Andrewartha
and P. Sakov

CSIRO
Hobart

March 2005

Contents

1. Introduction.	3
3. Model Domain.	6
4. Field Measurements	9
5. Input Data.	17
5.1 Wind Forcing.	17
5.2 Surface Elevation.	19
5.3 Temperature and Salinity.	20
5.4 River Flow.	21
5.4.1 Derwent River Flow	21
5.4.2 Huon River Flow	22
5.5 Bathymetry	23
6. Model Output.	25
6.1 Background	25
6.2 Model Calibration	25
6.3 Sensitivity	32
6.4 Annual simulations	35
7. Model Solutions	38
7.1 General Solutions	38
7.2 Residual Flow	47
7.3 Momentum Balance	51
7.4 Flushing Times	60
7.5 Mixing Zones	78
7.6 Connectivity	84
8. Conclusions	88
9. References	91

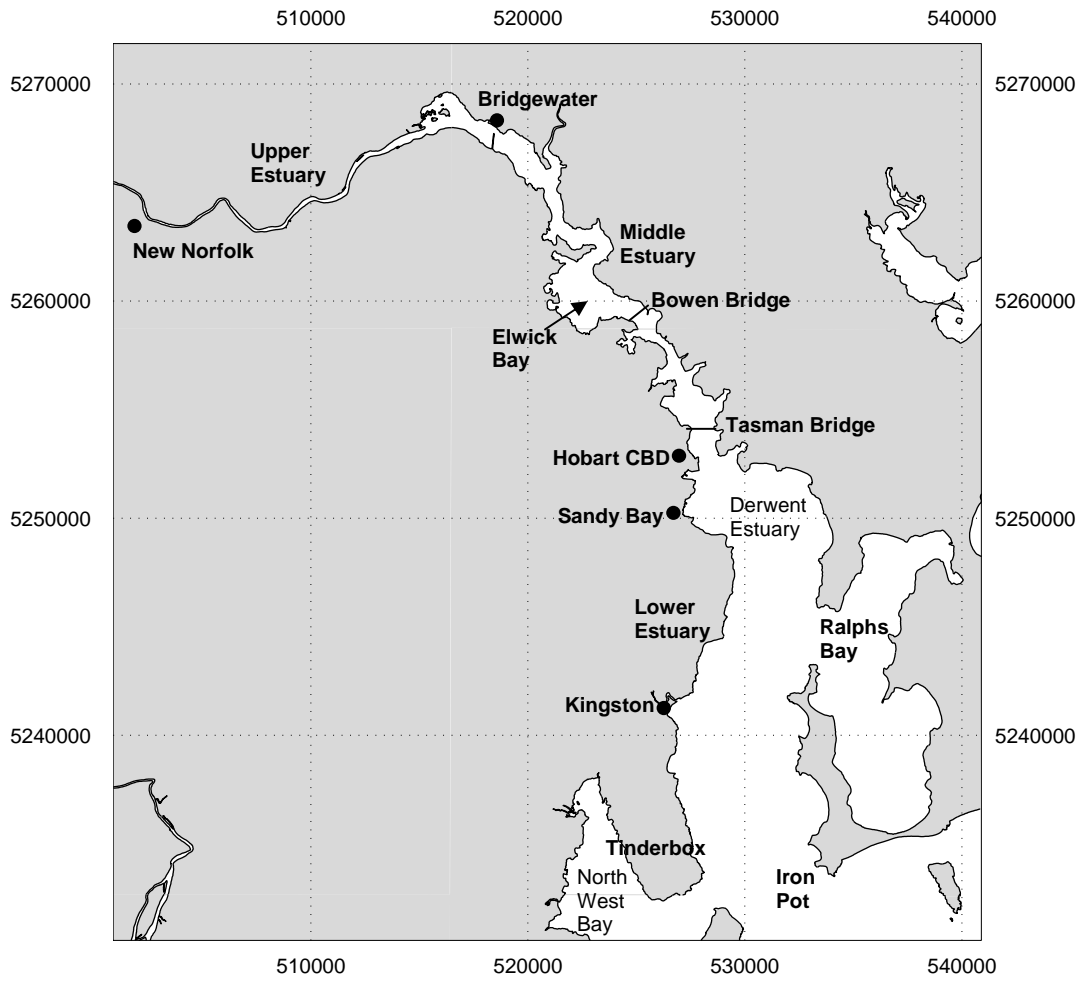
1. Introduction.

The Derwent Estuary Program (DEP) has identified the need for predictive capacity to augment a decision support system for the Derwent Estuary (Figure 1.1). This management system is designed to aid effective decision making regarding environmental issues, and predictive models play an integral role in assessing management scenarios and achieving system understanding. Of particular importance is the issue of heavy metal pollution, and coupled hydrodynamic, sediment and heavy metal prognostic models are important tools that may assist the formulation of management strategies. Hydrodynamic models have been previously applied to the upper Derwent (Parslow et al, 2001) to investigate the fate of contaminants from a point source, and recently larger scale models, encompassing the Derwent Estuary, have been produced within the Aquafin CRC. The experience gained in these studies provides a foundation upon which a dedicated modelling suite for the DEP may be constructed.

The goal of the hydrodynamic component of the DEP is to provide a hydrodynamic model that may assist in management strategy evaluation within a management framework, and provide understanding into the physical dynamics of the estuary (water transports, mixing regimes and temperature / salinity distributions) and the relationship between process occurring on different time and space scales. The hydrodynamic model forms a base into which sediment, contaminant or biogeochemical models may be coupled. This report outlines the development of the hydrodynamic model.

The model was forced with river flow from the Derwent River, wind stress and surface elevations, temperature & salinity on the seaward limits of the estuary. These seaward boundary conditions were derived from a larger scale model of the region and direct measurement. The hydrodynamic model is introduced in Section 2 and the model grid used described in Section 3. Data collected for calibration purposes is presented in Section 4 followed by presentation of data used to force the model in Section 5. Finally the modeling approach is described in Section 6, followed by presentation and analysis of model output in Section 7.

Figure 1.1 : Geography of the Derwent Estuary Region



2. The Hydrodynamic Model.

The hydrodynamic model used to simulate the physics of the Derwent Estuary is SHOC (Sparse Hydrodynamic Ocean Code, Walker and Waring, 1998). This model has been developed by the Environmental Modelling group at CSIRO (Commonwealth Scientific and Industrial Research Organization) Division of Marine Research over the last decade. SHOC is intended to be a general purpose model applicable to scales ranging from estuaries to regional ocean domains, and has been successfully applied to a variety of applications encompassing these scales to date. SHOC is a three-dimensional finite difference hydrodynamic model based on the primitive equations. Outputs from the model include three-dimensional distributions of velocity, temperature, salinity, density, passive tracers, mixing coefficients and sea level. Inputs required by the model include forcing due to wind, atmospheric pressure gradients, surface heat and water fluxes and open boundary conditions (e.g. tides). SHOC is based on the three dimensional equations of momentum, continuity and conservation of heat and salt, employing the hydrostatic and Boussinesq assumptions. The equations of motion are discretized on a finite difference stencil corresponding to the Arakawa C grid.

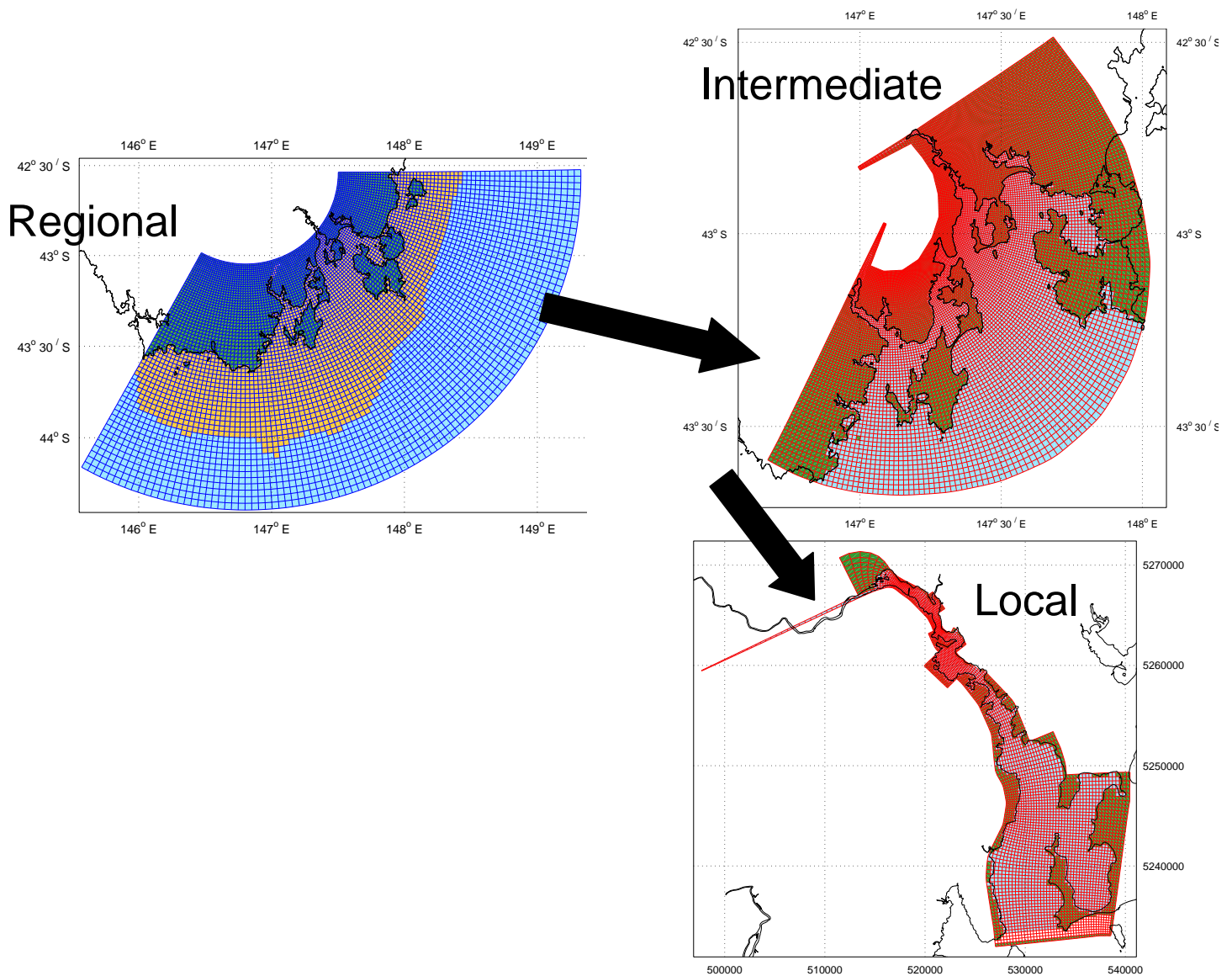
The model uses a curvilinear orthogonal grid in the horizontal and a choice of fixed 'z' coordinates or terrain following σ coordinates in the vertical. The curvilinear horizontal grid was particularly useful in this application since it enabled high resolution to be specified in areas of the study region where small scale motions were present and larger resolution where they were not. The 'z' vertical system allows for wetting and drying of surface cells, useful resolving the surface layer in the presence of moderate tides. SHOC has a free surface and uses mode splitting to separate the two dimensional (2D) mode from the three dimensional (3D) mode. This allows fast moving gravity waves to be solved independently from the slower moving internal waves allowing the 2D and 3D modes to operate on different time-steps, resulting in a considerable contribution to computational efficiency. Long period simulations were required (>1 year) to assess the impact of contaminants on the aquatic environment, and these simulations required acceptable run time ratios of greater than 100:1 (i.e. 100 model days in 1 day real time). The model uses explicit time-stepping throughout except for the vertical diffusion scheme which is implicit. The implicit scheme guarantees unconditional stability in regions of high vertical resolution. A Laplacian diffusion scheme is employed in the horizontal on geopotential surfaces. Smagorinsky mixing coefficients may be utilized in the horizontal.

SHOC can invoke several turbulence closure schemes, including k- ϵ , Mellor-Yamada 2.0 & 2.5 and Csanady type parameterizations. A variety of advection schemes may be used on tracers and 1st or 2nd order can be used for momentum. This study used the QUICKEST advection scheme for tracers (Leonard, 1979) in conjunction with the ULTIMATE limiter (Leonard, 1991). This scheme is characterized by very low numerical diffusion and dispersion, and yielded excellent performance when resolving frontal features, which often occurred in the salinity distribution during times of high flow of the Derwent River. SHOC also contains a suite of radiation, extrapolation, sponge and direct data forcing open boundary conditions. Input and output is handled through netCDF data formatted files, with the option of submitting ascii text files for simple time-series forcing. The netCDF format allows input of spatially and temporally varying forcing and initialization data in a grid and time-step independent manner. SHOC is capable of performing particle tracking and may be directly coupled to ecological and sediment transport models.

3. Model Domain.

A nested modelling system is employed for the Derwent region whereby small scale models are successively nested within larger scale models until the local Derwent Estuary domain can be adequately resolved. This nesting involves the local Derwent domain, an intermediate domain encompassing Storm Bay, the Tasman Peninsula and D'Entrecasteaux Channel and a regional domain covering the south east Tasmanian shelf and slope (Figure 3.1). This nesting strategy allows basin scale phenomena to be communicated into the local domain through the open boundaries and minimizes over-specification problems on the open boundaries. Also, this strategy is often the only way that open boundary data can be specified in the absence of field-derived temperature, salinity and surface elevation measurements (open boundaries are the limits of the domain beyond which no information is available for the model, and hence for which data must be explicitly supplied).

Figure 3.1 : Nesting Procedure



The local Derwent Estuary domain is displayed in Figure 3.2. The Derwent Estuary domain extends ~50km from New Norfolk at the upstream limit to Iron Pot at the seaward boundary. The deepest region of the estuary lies in the lower limits near Kingston, and reaches ~30m depth. Further up the estuary towards the Tasman Bridge depth decreases to 20m or less and the middle estuary consists of a relatively narrow channel 5 – 7m deep surrounded by shallow flats and wetlands. A deep hole of ~40m exists at the Tasman Bridge. Above Bridgewater the estuary forms a meandering river of average depth ~5m punctuated by deep holes 10 -15m deep. The domain was discretized using a curvilinear grid with variable resolution, resulting in minimum resolution above Elwick Bay of ~140m and maximum near Kingston at ~400m. The model uses 23 'z' layers in the vertical with 0.5m resolution to 8m depth. There exist 11024 (212 x 52) surface cells in the grid, only 2810 (25%) of which are wet; i.e. the majority of this grid is associated with dry land. The model grid is displayed in Figure 3.3. Above Bridgewater the river was straightened and resolved in 2-dimensions to reduce computational pressures imposed by the stability constraints if the cross-river dimension were resolved. Using this grid, time steps of 40 and 5 seconds were used for the 3D and 2D components of the model respectively, yielding a run time ratio of greater than 100:1 which allowed long term simulations to be performed (e.g. 1 year simulations in approximately 3 days real time) .

Figure 3.2 : Derwent Estuary Domain

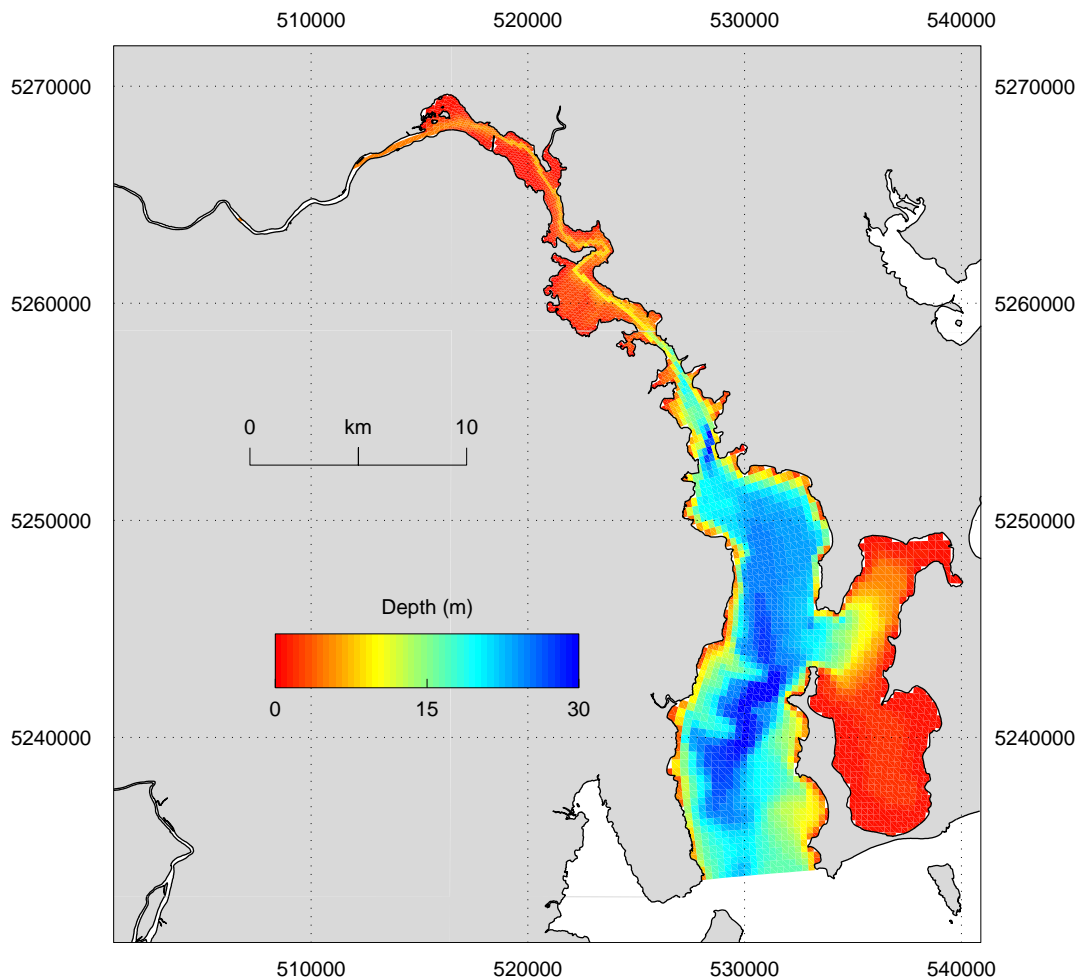
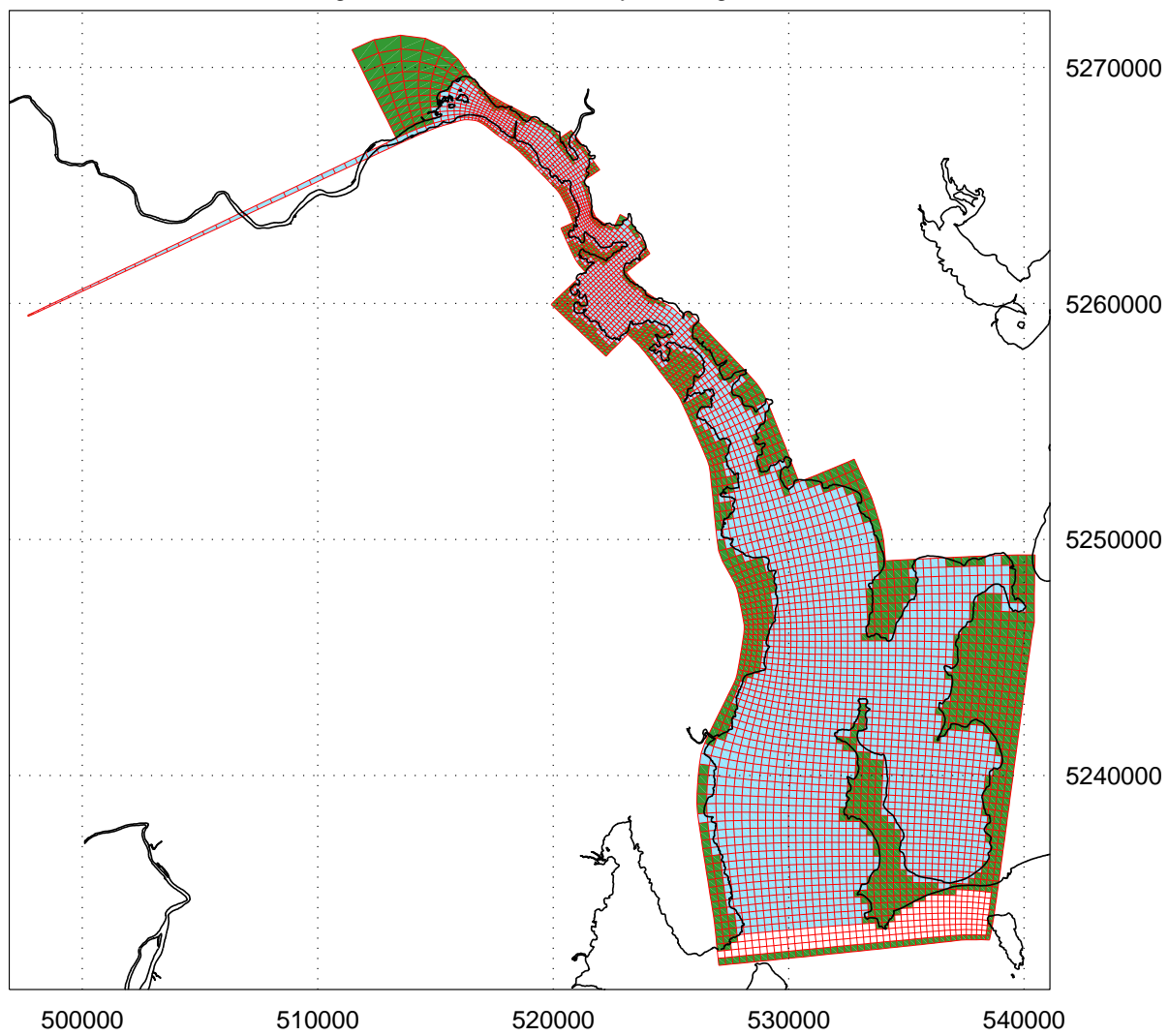


Figure 3.3 : Derwent Estuary model grid.



4. Field Measurements

During December 2003 to March 2004 equipment was deployed to measure temperature, salinity and currents for the purpose of calibration and boundary condition specification at the seaward boundary. CTD (conductivity, temperature, depth) instruments were moored at the bottom of the seaward boundary and at the surface either side of the estuary. These moorings supplied temperature and salinity open boundary conditions. A re-locatable mooring consisting of CTD and ADCP (acoustic dopplar current profiler) was successively moved up-estuary at intervals of 2-4 weeks and provided data for model calibration and system characterization. The locations of these moorings are described in Figure and Table 4.1.

Figure 4.1 : Mooring sites

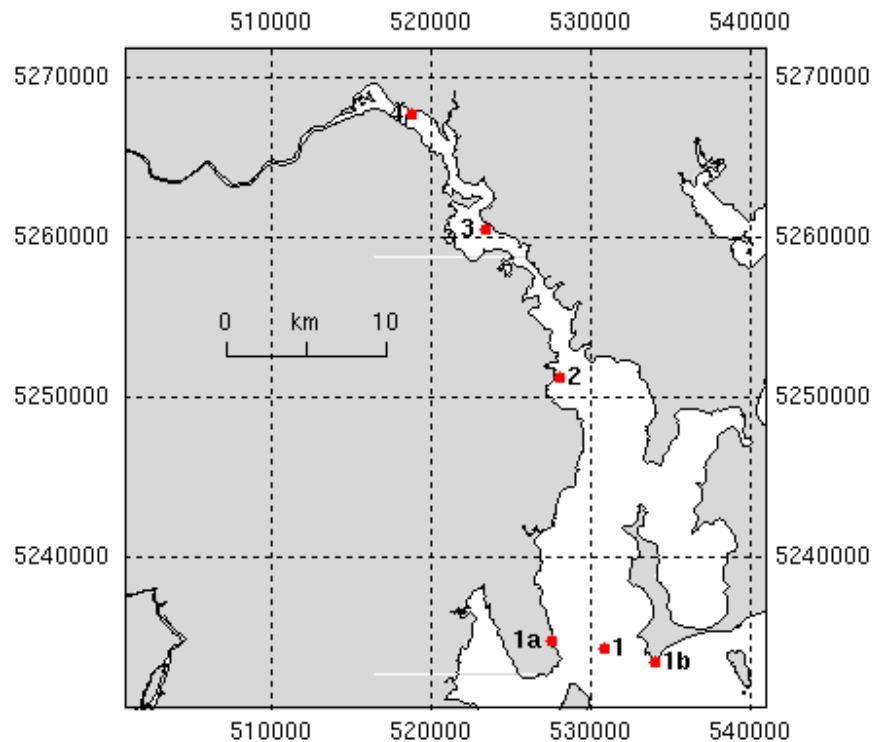


Table 4.1 : Mooring locations

Mooring	Latitude	Longitude	Depth (m)	Mean Depth* (m)	Duration
Reloc 1 : Iron Pot	43.04302	146.37891	16.1	15.6	17/12 – 20/1
Reloc 2 : Sandy Bay	42.89092	146.34318	23.8	22.9	21/1 – 5/2
Reloc 3 : Elwick Bay	42.80762	146.28538	8.1	6.4	5/2 – 17/02
Reloc 4 : Bridgewater	42.74323	146.22984	6.5	3.7	17/02 – 11/03
Boundary 1a	43.03916	146.33772	1.9	-	17/12 – 11/03
Boundary 1b	43.05093	146.41716	1.6	-	17/12 – 11/03
Boundary 1	43.04286	146.37841	16.3	15.8	17/12 – 11/03

The mean depth is the depth of the CTD determined by the mean of the measured sea level over the period sampled.

The re-locatable mooring consisted of a SeaBird SBE36 CTD and a Nortek 1MHz Aquadopp ADCP configured in the manner displayed in Figure 4.2. The ADCP contained a side-looking transducer which allowed current measurements to begin very close to the sea bed. In order not to interfere with the ADCP measurement the CTD was positioned ~30m to the side, and sat ~2.5m above the bottom. This means that there existed ~2m depth difference between the CTD and ADCP measurement depths. The mooring was retrieved via acoustic release.

Figure 4.2 : Re-locatable mooring configuration



The temperature, salinity and currents at the depth of the CTD (i.e near bottom currents) obtained from the moorings is displayed in Figures 4.3 to 4.8. Elevations in Figures 4.6 – 4.9 have the mean from Table 4.1 subtracted.

Figure 4.3 : Re-locatable mooring temperature and salinity

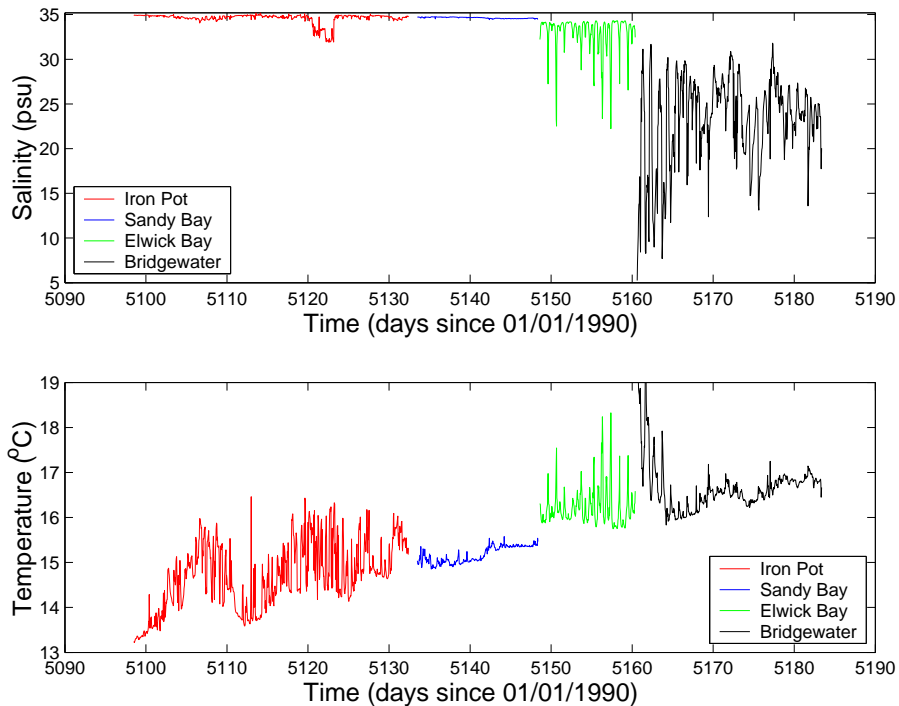


Figure 4.4 : Iron Pot boundary temperature and salinity

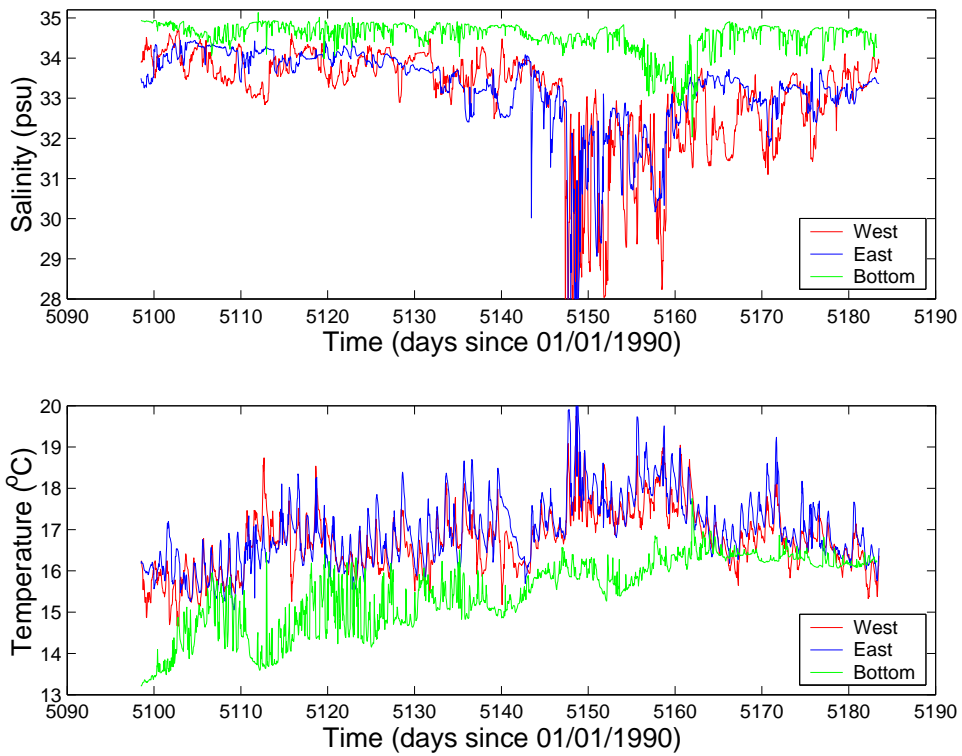


Figure 4.5 : Comparison of CTD and ADCP temperature

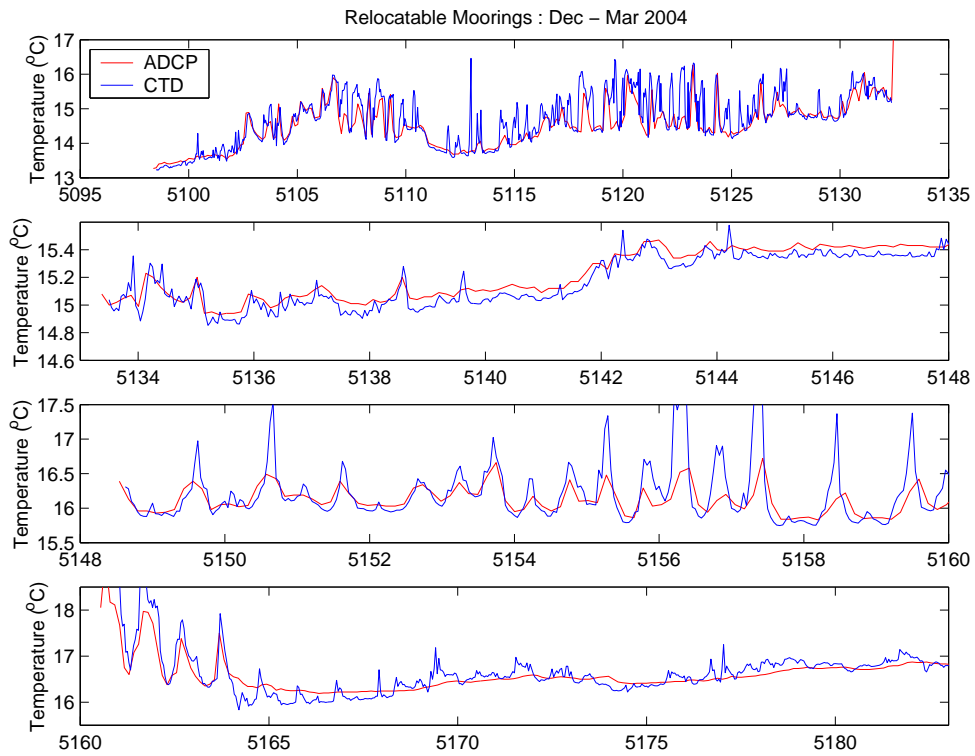
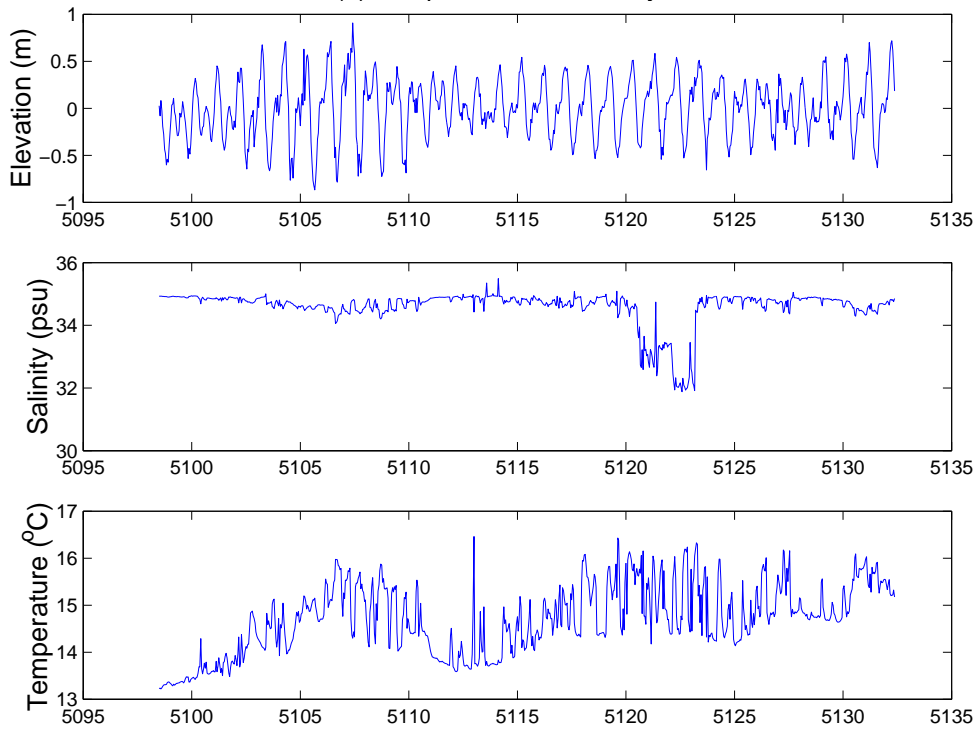


Figure 4.6 : Re-locatable mooring, Iron Pot
(a) Temperature and salinity



(b) Velocity

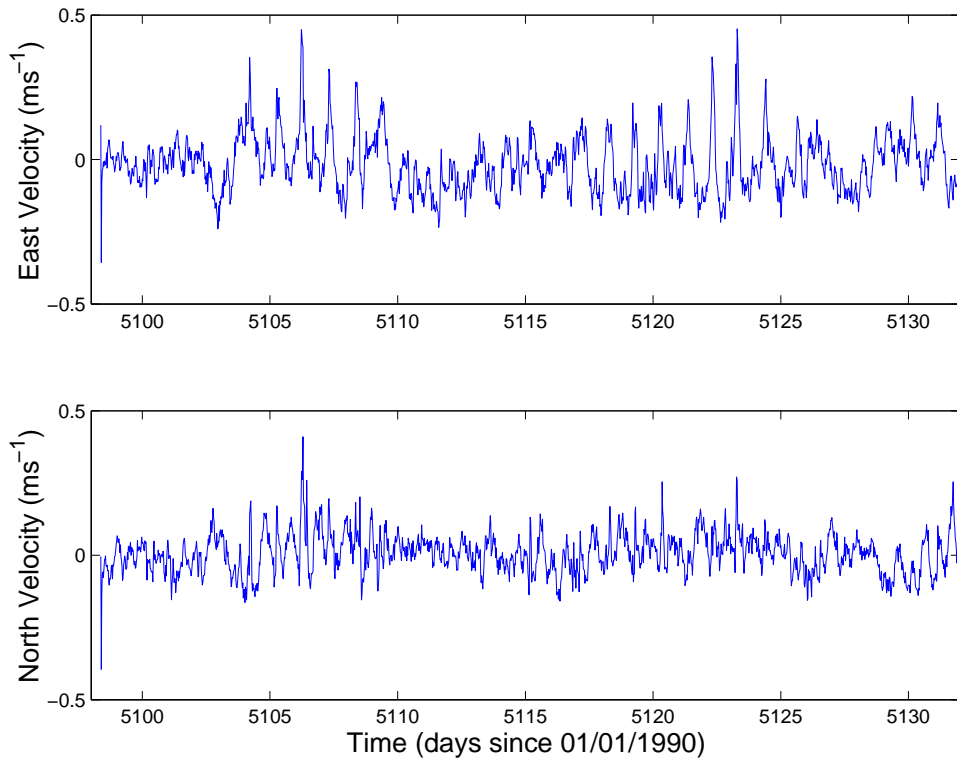
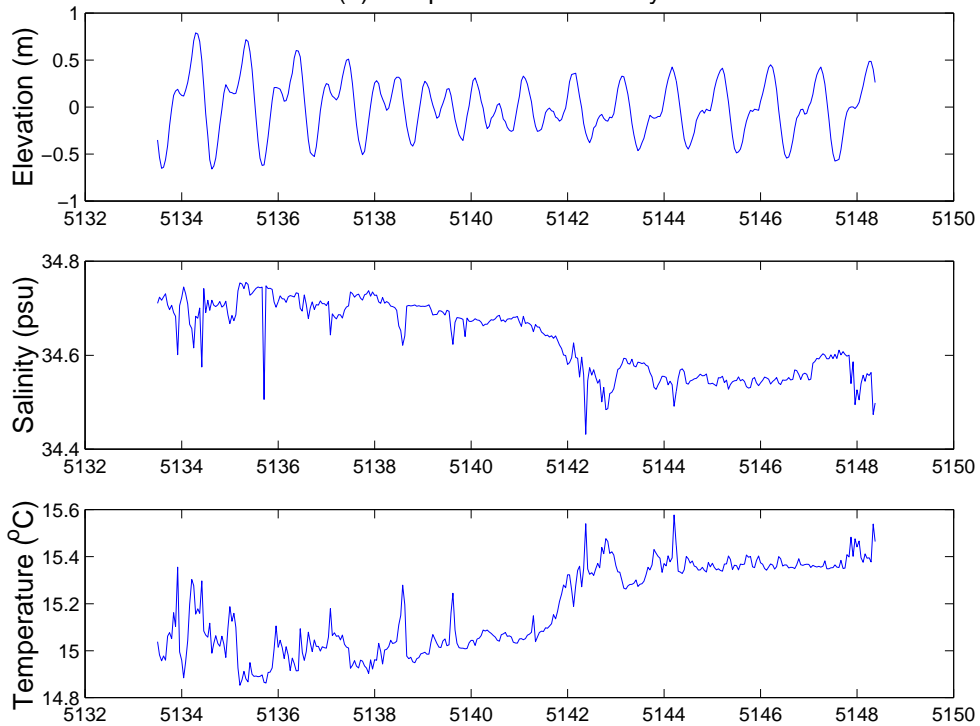


Figure 4.7 : Re-locatable mooring, Sandy Bay
(a) Temperature and salinity



(b) Velocity

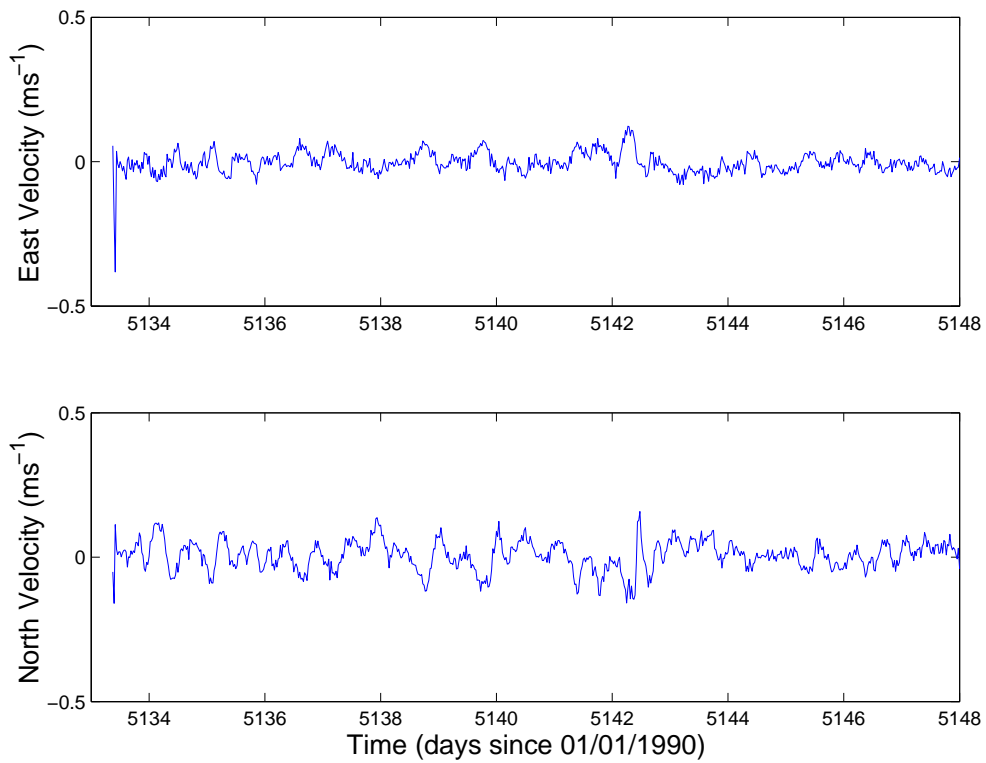
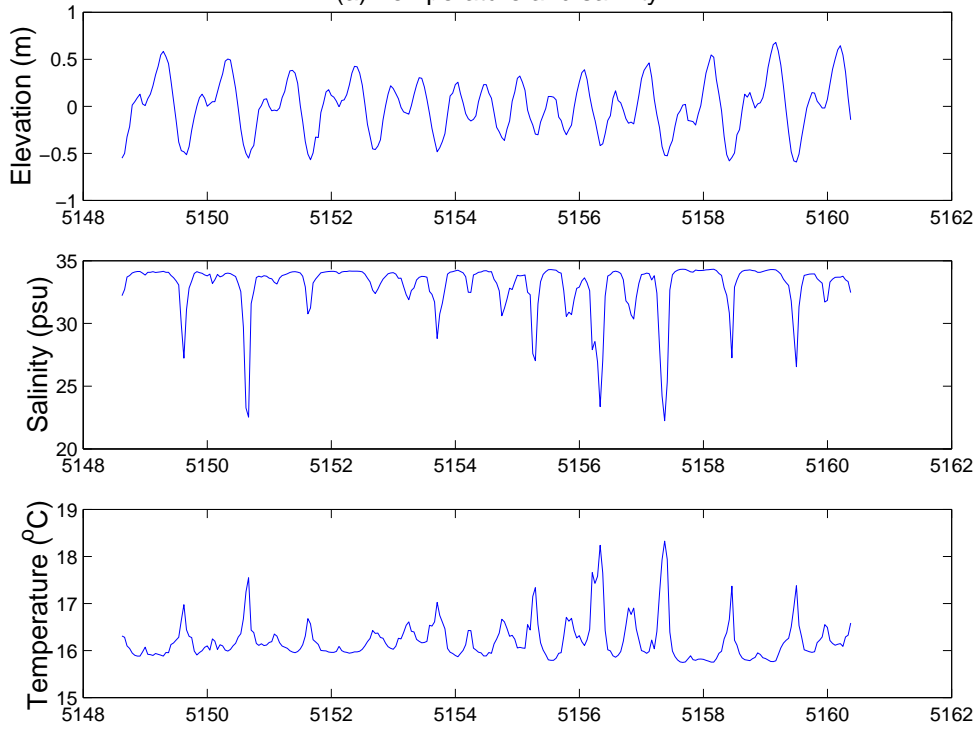


Figure 4.8 : Re-locatable mooring, Elwick Bay
(a) Temperature and salinity



(b) Velocity

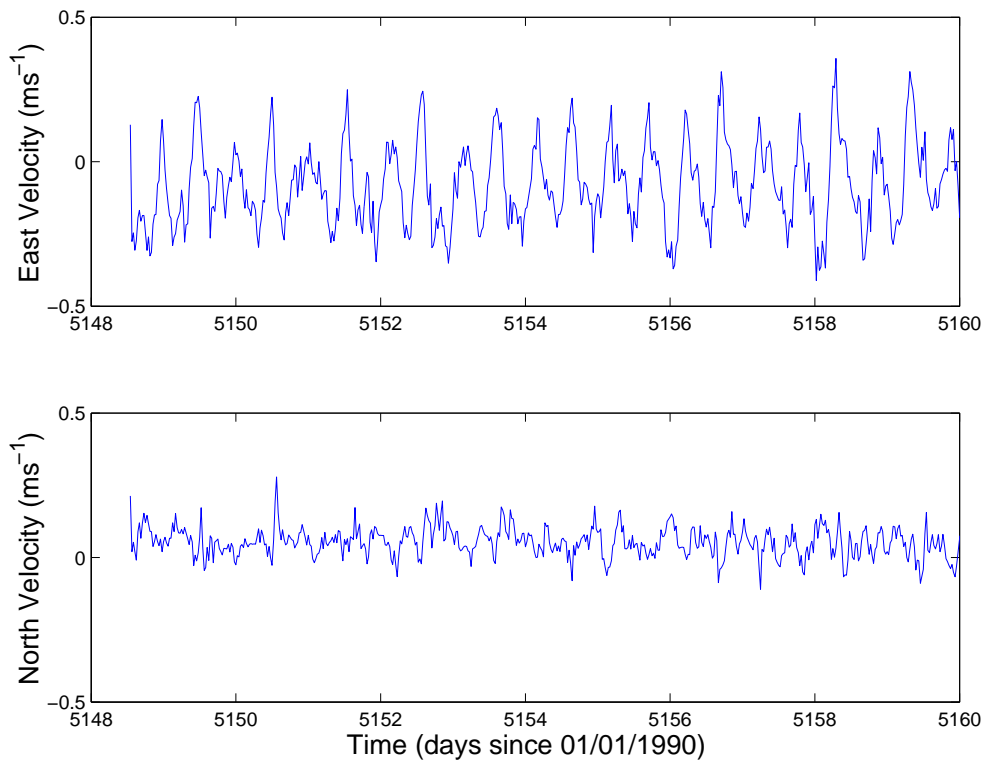
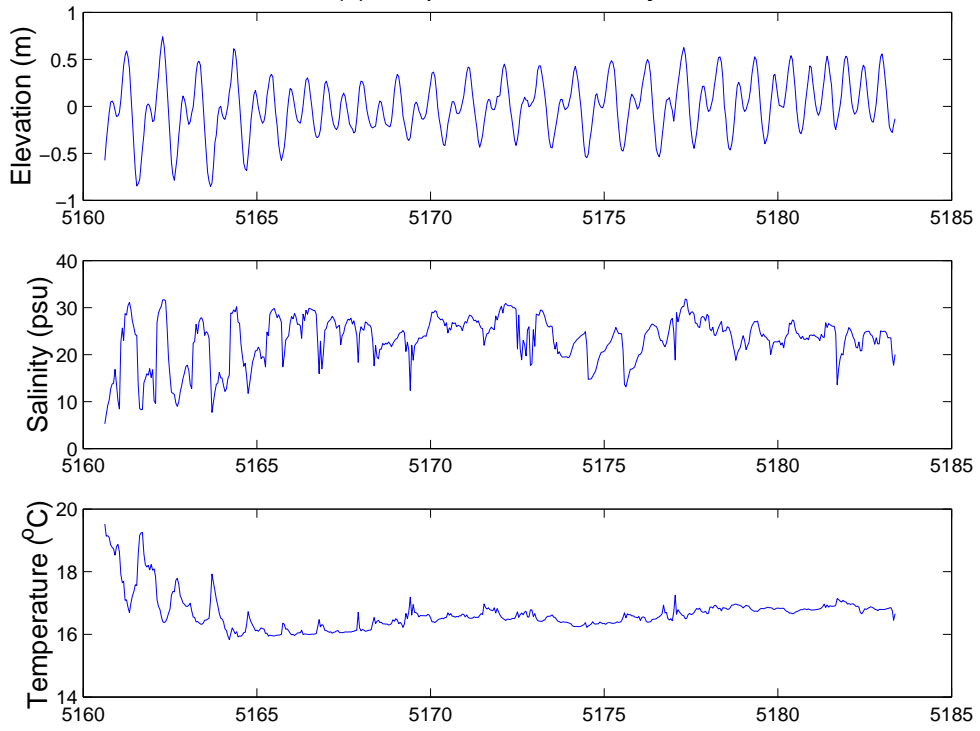
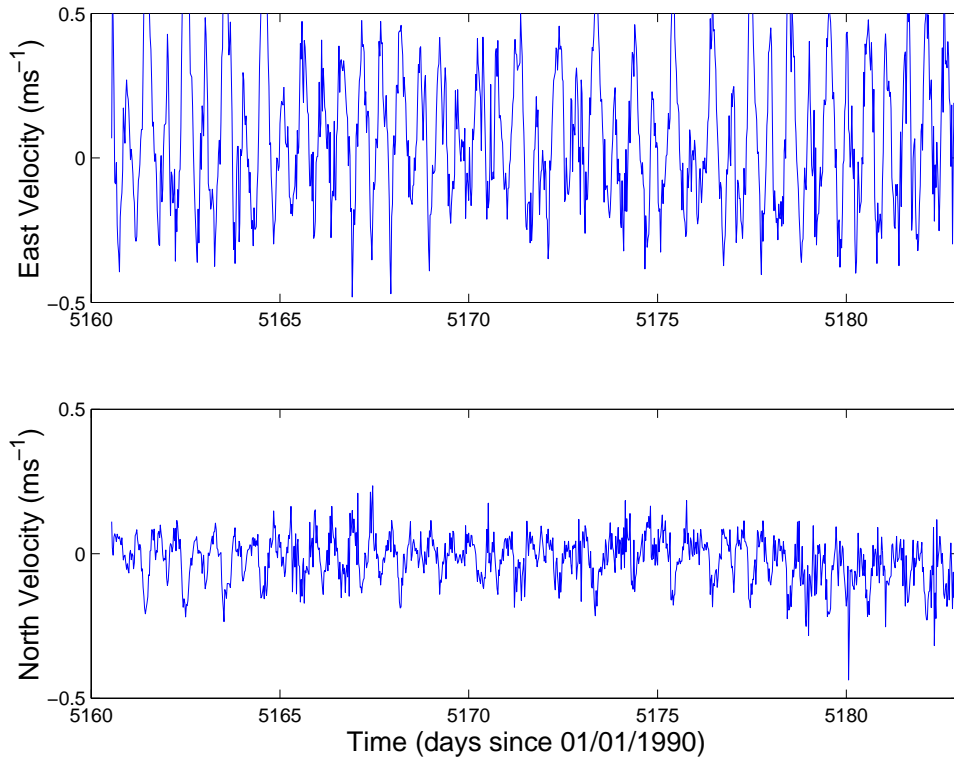


Figure 4.9 : Re-locatable mooring, Bridgewater
(a) Temperature and salinity



(b) Velocity



Tidal range is ~1m during spring tides and 0.5m during neap tides. The tide exhibits a progression from diurnal character to semi-diurnal character quantified by the form factor $F = \text{ratio of diurnal to semi-diurnal amplitudes} (F = K_1 + O_1 / M_2 + S_2)$, which in the case of the Derwent ~1.5 verifying that the tide is of predominantly diurnal mixed character. The river becomes fresher and warmer heading up-estuary, and more variability is observed in the salinity towards Bridgewater. At Iron Pot bottom water is colder and saltier than surface water and variability is observed between the western and eastern sides of the estuary. Salinity and temperature in the upper estuary also show a pronounced pulsing at the tidal frequency, where bottom waters become fresher and warmer on the ebb tide (Figure 4.8a). This effect is diminished closer to the river bed (Figure 4.5; the ADCP measured temperature ~2m deeper than the CTD. The ADCP was not equipped with a salinity sensor.) The river channel is approximately oriented in a north-west direction at Elwick Bay and Bridgewater, hence the along-channel velocity is a vector sum of the components displayed above. However, it can be observed that appreciable tidal currents occur at Elwick Bay of several 10s of centimeters, and strong currents occur at Bridgewater, presumably due to the constriction caused by the causeway at this location.

5. Input Data.

The model was forced with wind, river flow from the Derwent River and elevation, temperature and salinity at the two oceanic open boundaries. The sources of these forcings are detailed below.

5.1 Wind Forcing.

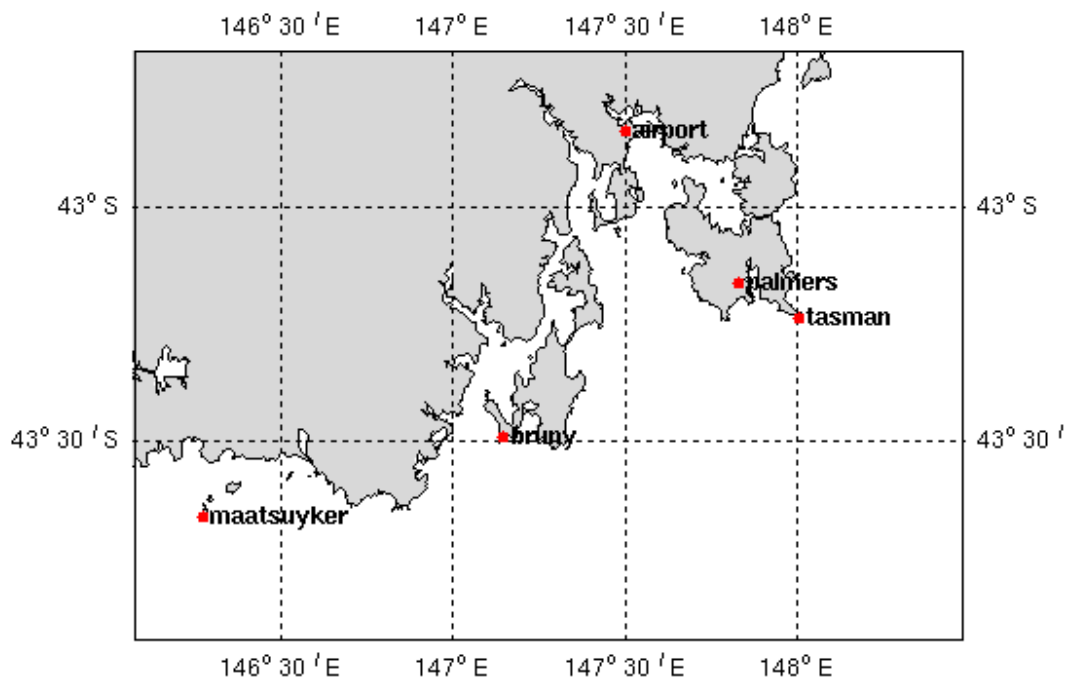
Wind speed and direction data were obtained from the Bureau of Meteorology (BOM) at the following locations and interpolated onto the regional and local domains to provide a temporally and spatially varying wind-field.

Wind measurement sites are summarized in Table 5.1 and Figure 5.1.1.

Table 5.1 : Wind Measurement Sites

Site	Latitude (deg S)	Longitude (deg E)	Mean Speed (ms^{-1})
Hobart Airport	42.8389	146.4992	5.2
Palmers Lookout	43.1650	146.8317	4.3
Cape Bruny	43.4903	146.1447	6.3
Maatsuyker Island	43.6578	146.2711	10.4
Tasman Island	43.2397	148.0025	6.2

Figure 5.1.1 : Wind Measurement sites



A sample of the wind-field at these sites is shown in Figure 5.1.2 (a) and (b) for the 17 Dec 2003 to 11 Mar 2004. The mean for this period is oriented at 214°T with speed of 6.7 ms^{-1} .

Figure 5.1.2 (a) : Wind Speed at Measurement Sites

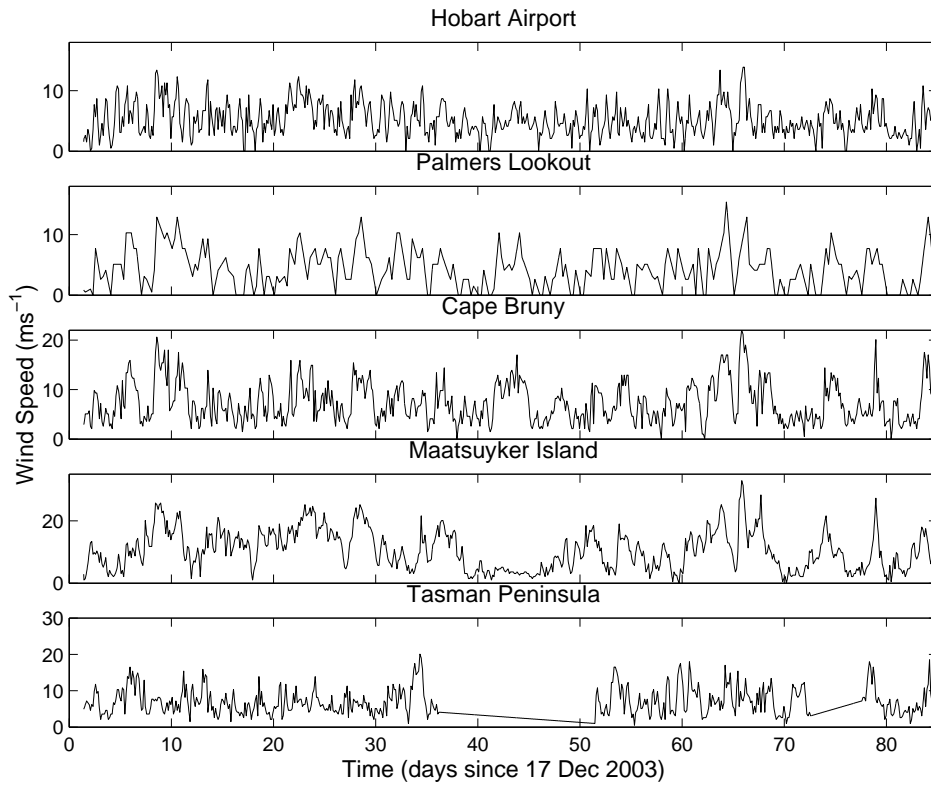
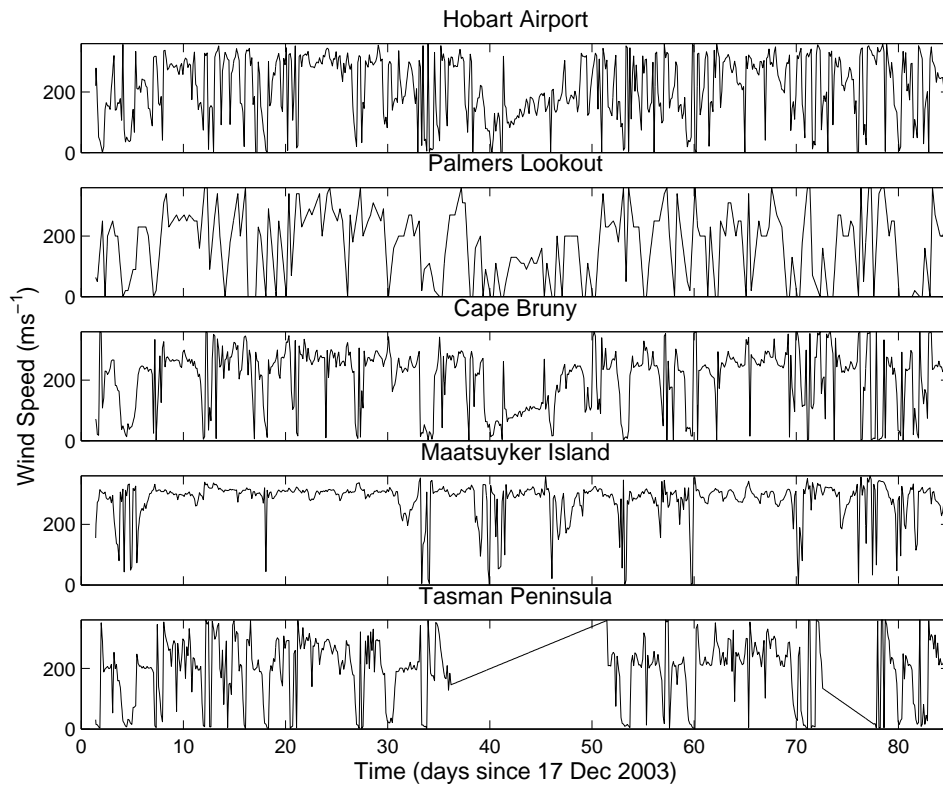


Figure 5.1.2 (b) : Wind Direction at Measurement Sites



5.2 Surface Elevation.

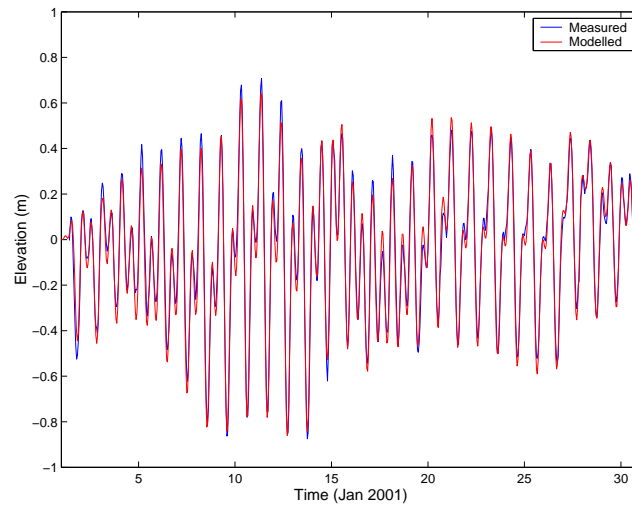
The surface elevation for the local Derwent Estuary domain was supplied from output of the nested intermediate and regional models. The elevations used in the region model consist of a high frequency component (tidal component with frequencies < 1 day) and a long period component with frequencies of days to weeks. The tidal component applicable to the regional domain was constructed from a global tidal model (Cartwright and Ray, 1990). This global model did not perform well in the vicinity of the north-eastern cross-shelf boundary, so a yet larger domain was created to encompass the regional grid upon which the model was run in barotropic (2D) mode only to yield time series of surface elevation on this boundary. These time series were then decomposed into the tidal constituents, which were subsequently used to force the tidal component in the regional model. This approach provided better results than directly imposing the global tidal model constituents on the north-eastern boundary. The tidal constituents are presented in Table 5.2 with the ranges of amplitude encountered. Note that these constituent's amplitude and phase vary spatially around the open boundary perimeter.

The long period component was extracted from low passed elevation records collected at Port Arthur on the Tasman Peninsula (courtesy of J. Hunter, UTAS) and Spring Bay on the east coast (from National Tidal Facility). The Port Arthur signal was lead by 0.5 days and applied at the western open boundary of the regional model with no change in amplitude. The Spring Bay long period component was applied directly to north-eastern boundary. These long period components are applicable to the coast only, and an offshore profile was imposed on the amplitude to correctly specify the long period wave over the shelf. The resulting modelled surface elevations were compared to those measured at Hobart to validate the forcing, as illustrated in Figure 5.2.1.

Table 5.2 : Tidal Harmonics for the Regional Model

Name	Western Boundary Amplitude (m)	Offshore Boundary Amplitude (m)	NE Boundary Amplitude (m)
Q1	0.028 - 0.029	0.022 – 0.028	0.022
O1	0.119 - 0.125	0.099 – 0.119	0.099 - .113
P1	0.054 - 0.058	0.049 – 0.054	0.049 – 0.058
S1	0.001	0.001	0.001 – 0.002
K1	0.165 - 0.176	0.150 – 0.165	0.151 – 0.172
2N2	0.008 - 0.010	0.008 - 0.014	0.014
MU2	0.009 - 0.011	0.009 - 0.016	0.017
N2	0.031 - 0.034	0.031 - 0.083	0.085
NU2	0.005 - 0.006	0.005 - 0.015	0.016
M2	0.119 - 0.120	0.119 - 0.325	0.330 – 0.332
L2	0.003 - 0.004	0.003 - 0.006	0.006
T2	0.004 - 0.005	0.003 – 0.004	0.002 – 0.003
S2	0.074 - 0.087	0.038 – 0.074	0.035 – 0.039
K2	0.022 - 0.026	0.008 – 0.022	0.008

Figure 5.2.1 : Segment of Surface Elevation at Hobart.



The elevations provided by the regional model were then used in the higher resolution nested grids. Obviously these elevation signals contained both the diurnal and long period fluctuations.

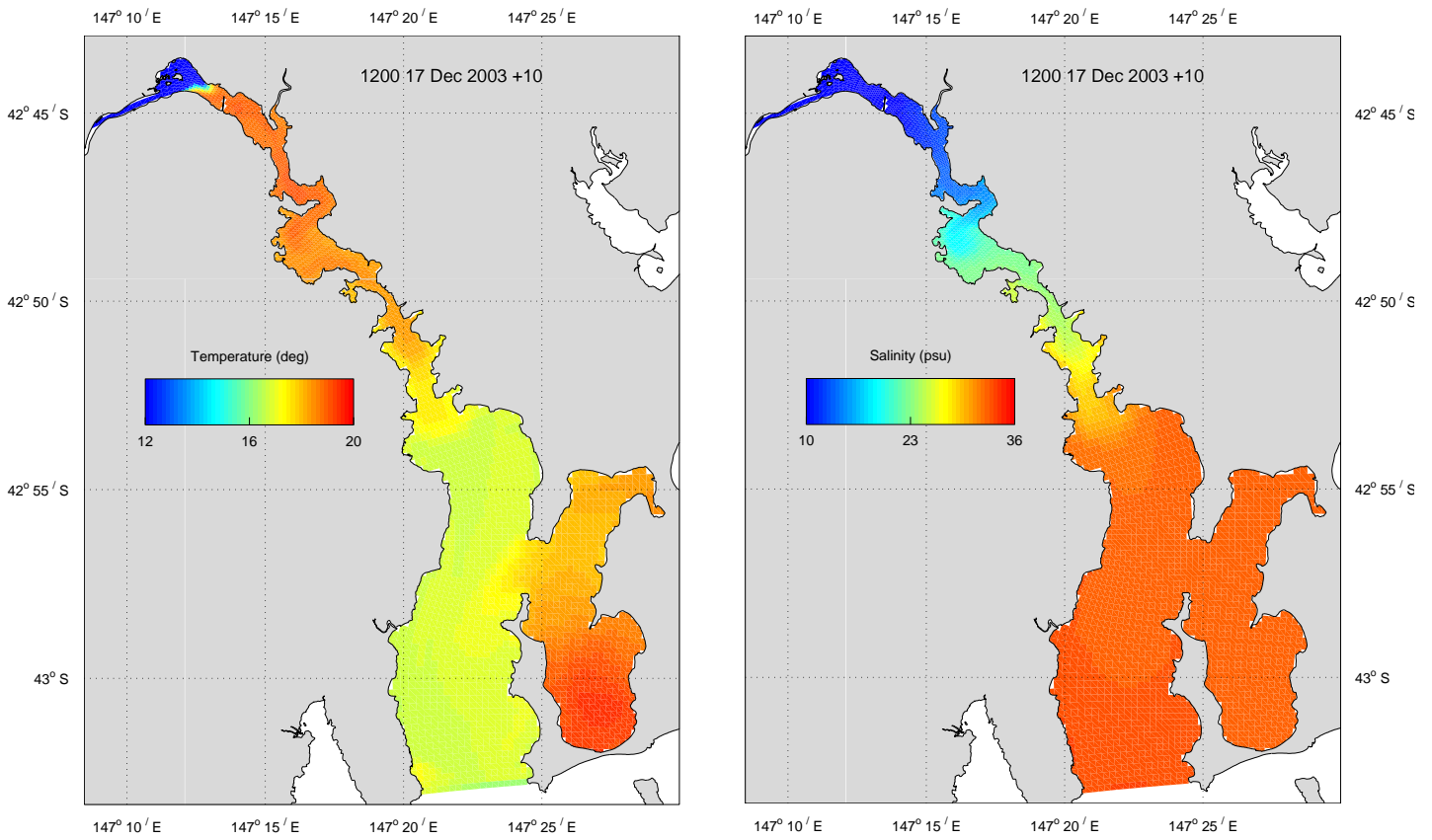
5.3 Temperature and Salinity.

The temperature and salinity distribution in the regional model was initialized with annual mean distributions provided by the CARS atlas (Climatological Atlas of Regional Seas, Ridgway et al 2002). These data provide a mean annual cycle of temperature and salinity output at 10 day intervals on a 1/8 degree grid. The open boundaries of the regional domain were also forced with the CARS climatology. The intermediate model was forced with river discharges from both the Derwent and Huon Rivers in addition to boundary forcing from the regional model, and a surface heat flux was also applied. The intermediate model was run from Jan 2003 to Mar 2004, and temperature and salinity solutions from this were used as initial conditions for the local model. Initial temperature and salinity distributions are displayed in Figures 5.3.1.

The mooring temperature and salinity data (Figure 4.4) were used as boundary conditions for the local model. Since measurements were only made at the surface and bottom, these data were required to be interpolated over the full depth range. A strategy was employed whereby the T/S measurements were scaled to the actual density profile predicted by the model a certain number of cells into the model interior (5 cells), then applied over the full depth range at the boundary. This allowed surface and bottom mixed layers to be resolved in time and space, and required one bottom measurement at the deepest location and several surface measurements.

Figure 5.3.1 : Initial conditions at 17 Dec 2003
(a) Temperature

(b) Salinity

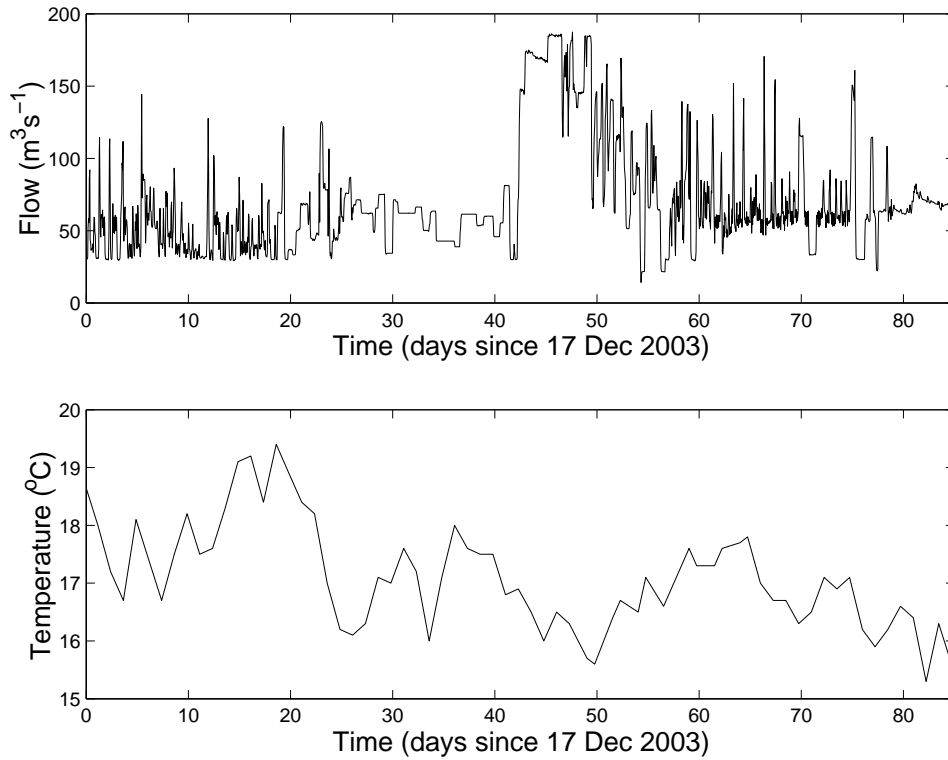


5.4 River Flow.

5.4.1 Derwent River Flow

Derwent River flow was input as the boundary condition at New Norfolk in all the models in the nesting suite. Hourly flow was obtained from the Tasmanian Hydro below Meadowbank. River temperature was obtained via Dept. of Primary Industries, Water and Environment (DPIWE) for the same interval at random times and interpolated to hourly data. The salinity of the Derwent inflow is assumed to be fresh (i.e. 0 psu). River flow and temperature are displayed in Figure 5.4.1. Note that the Derwent River is a regulated flow so there exist periods where flow rate does not change.

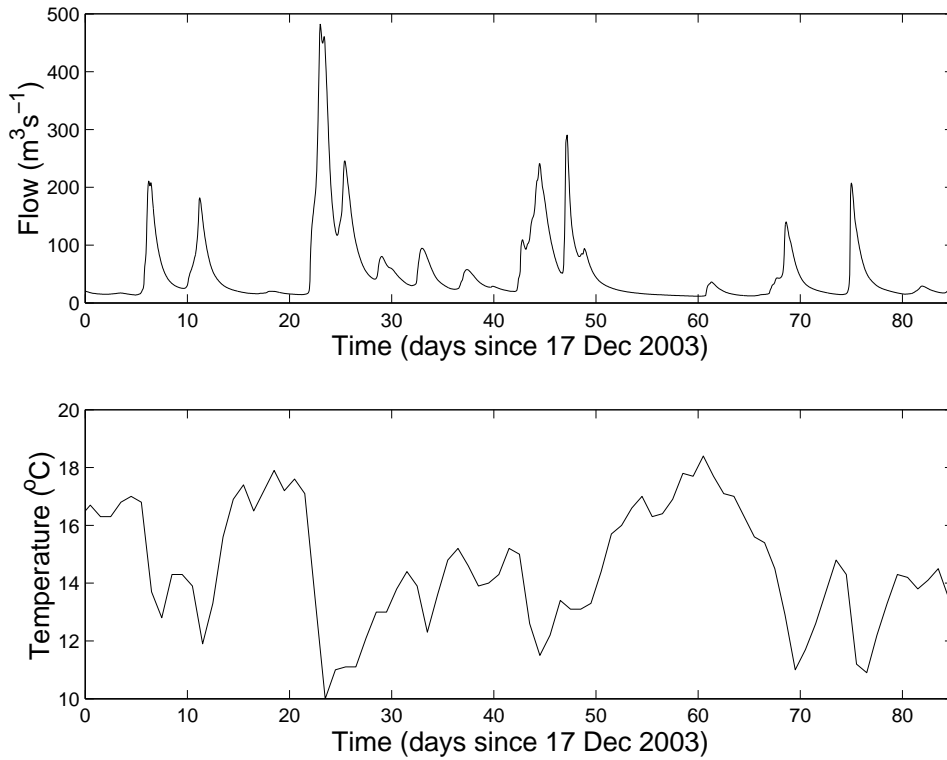
Figure 5.4.1 : Derwent River characteristics at New Norfolk



5.4.2 Huon River Flow

Huon River flow was required as the boundary condition at Huonville to force the intermediate and regional models. Hourly river flow records were obtained at Frying Pan Creek (courtesy of DPIWE) and multiplied by a scaling factor of 1.2 to allow for catchment area contributing to flow below this location, resulting in flow applicable to Huonville. The salinity of the Huon inflow is assumed to be fresh and the temperature was obtained from daily measurements at Judbury (DPIWE). Time series of the Huon flow and temperature is presented in Figure 5.4.2.

Figure 5.4.2 : Huon River characteristics at Huonville



5.5 Bathymetry

There existed no reliable bathymetry measurements in the region between Bowen Bridge and Bridgewater. Additional data was made available courtesy of A. Jordan (TAFI). These samples were mostly concentrated along the river edges and did not resolve the channel particularly well. An additional 350 samples were taken using the echo sounder on CSIRO Explorer and a GPS unit in an attempt to define the channel. The coverage resulting from these data gathering exercises is displayed in Figure 5.5.1 (a) and (b). These data were incorporated into the existing data set and the original and improved bathymetries are displayed in Figure 5.5.2. The channel is still not adequately resolved which is anticipated to lead to calibration issues.

Figure 5.5.1 : Additional bathymetry coverage
 (a) TAFI (b) Field sampled

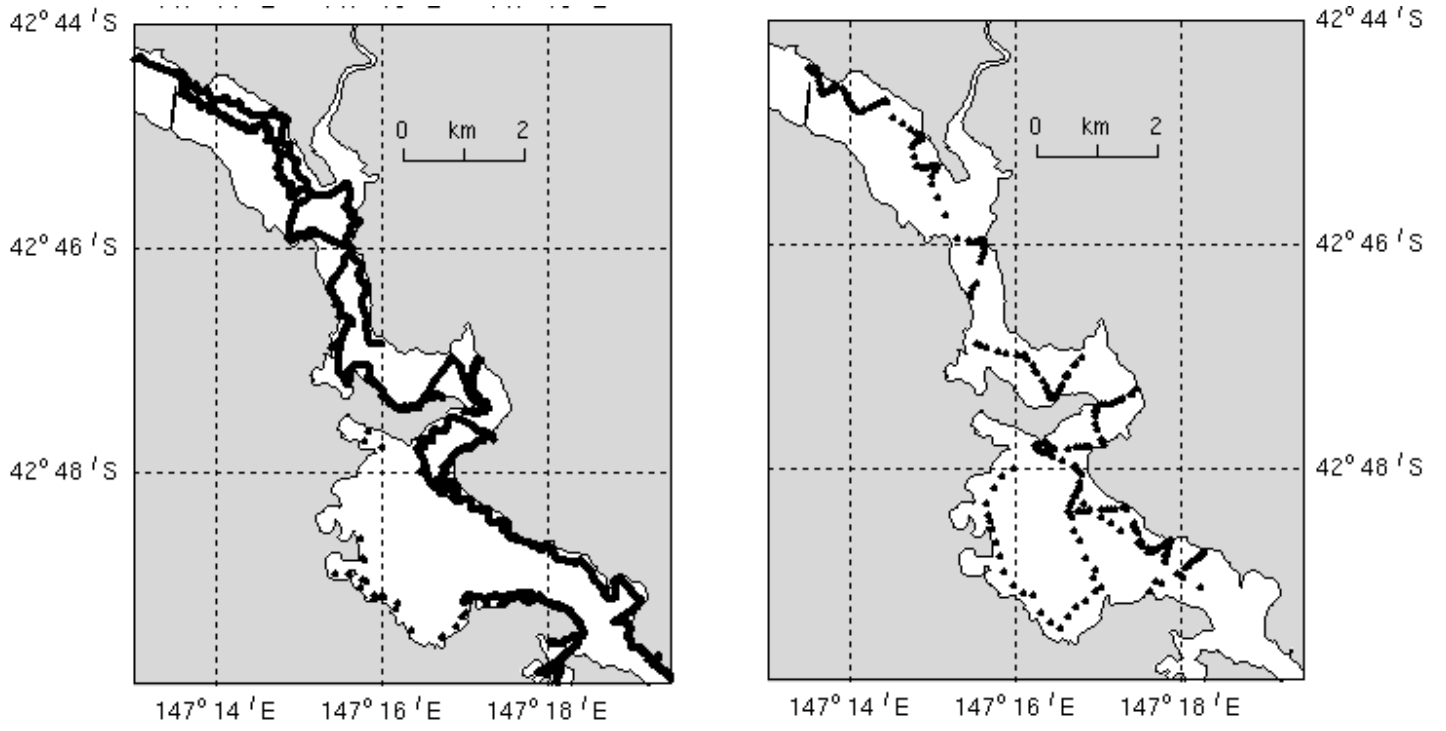
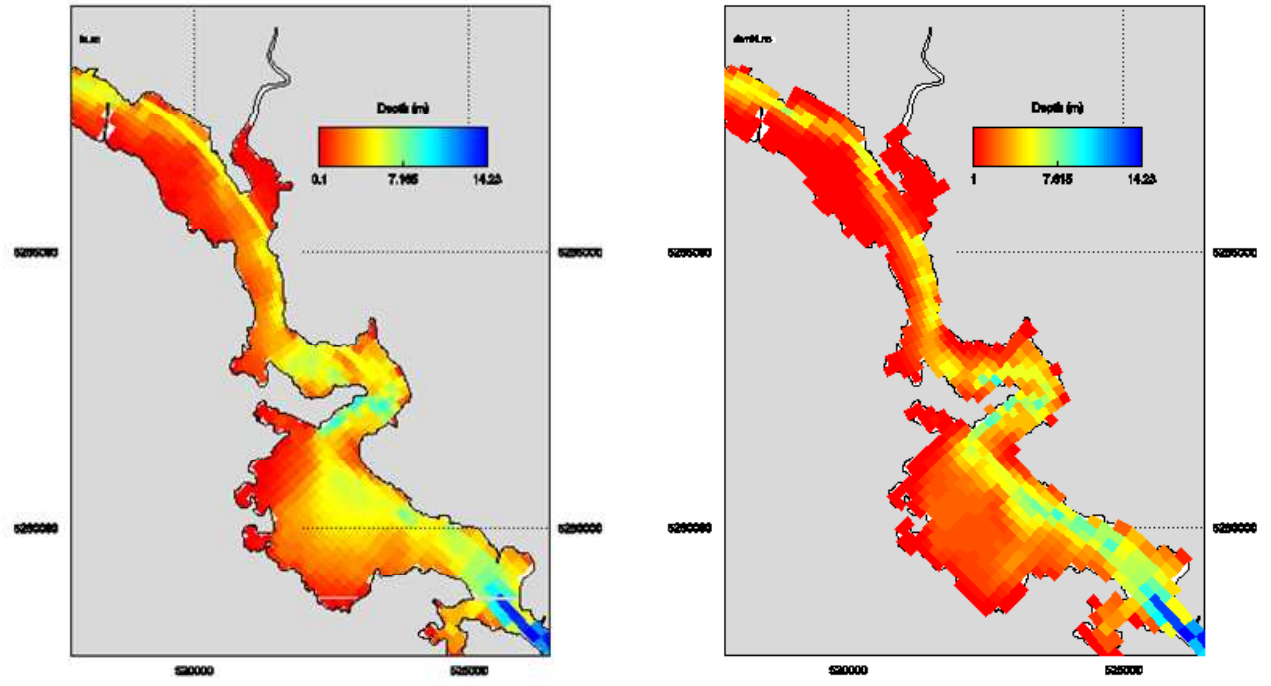


Figure 5.5.2 : Bathymetry coverage field measurement.
 (a) Before (b) After



6. Model Output.

6.1 Background

The Derwent Estuary is classified as a micro-tidal salt wedge estuary. The head of the salt wedge is located near New Norfolk during periods of low flow and is pushed downstream past Bridgewater under flows higher than $\sim 150\text{m}^3\text{s}^{-1}$ (Thompson & Godfrey, 1985). Mixing is predominantly wind driven with tidal mixing occurring in the upper reaches. Tides undergo a neap spring cycle with a period of ~ 14 days and the tide is of diurnal (daily) mixed character where the diurnal tide is greater than the semi-diurnal. The freshwater plume favours the eastern shore upon exiting the estuary and the flushing time is estimated to be ~ 15 days (Green and Coughanowr, 2003).

6.2 Model Calibration

The modelled and measured sea level at Hobart (courtesy of Hobart Ports Corporation) is displayed in Figure 6.2.1. The modelled sea level and that measured by the CTD on the relocatable mooring (with the mean from Table 4.1 subtracted) is displayed in Figure 6.2.2. These Figures show that the model performs well in terms of sea level, capturing the mixed diurnal tidal character and neap spring cycles.

Figure 6.2.1 : Modelled and measured sea level at Hobart

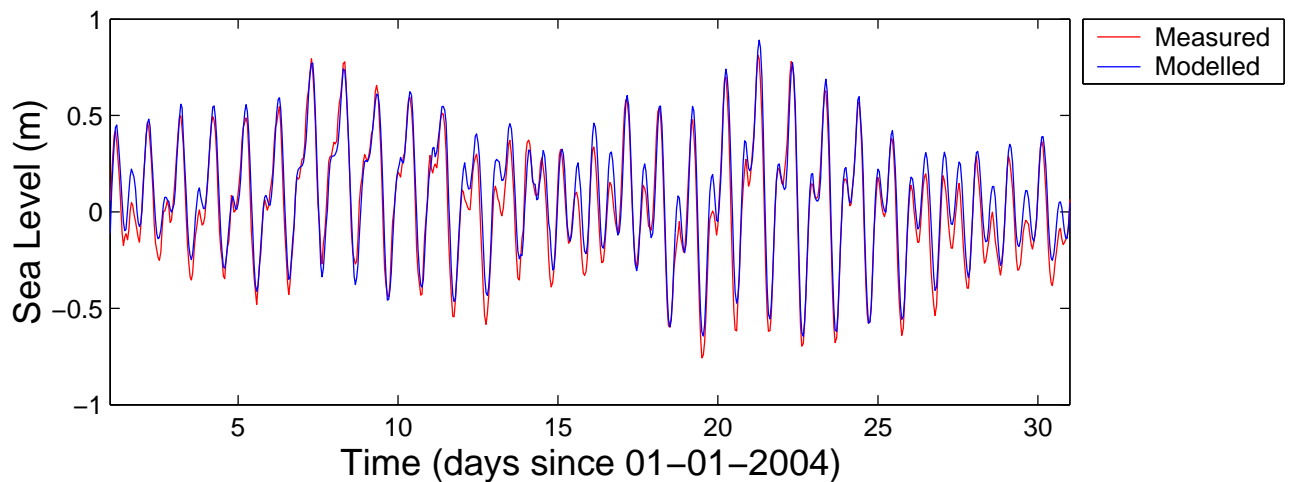
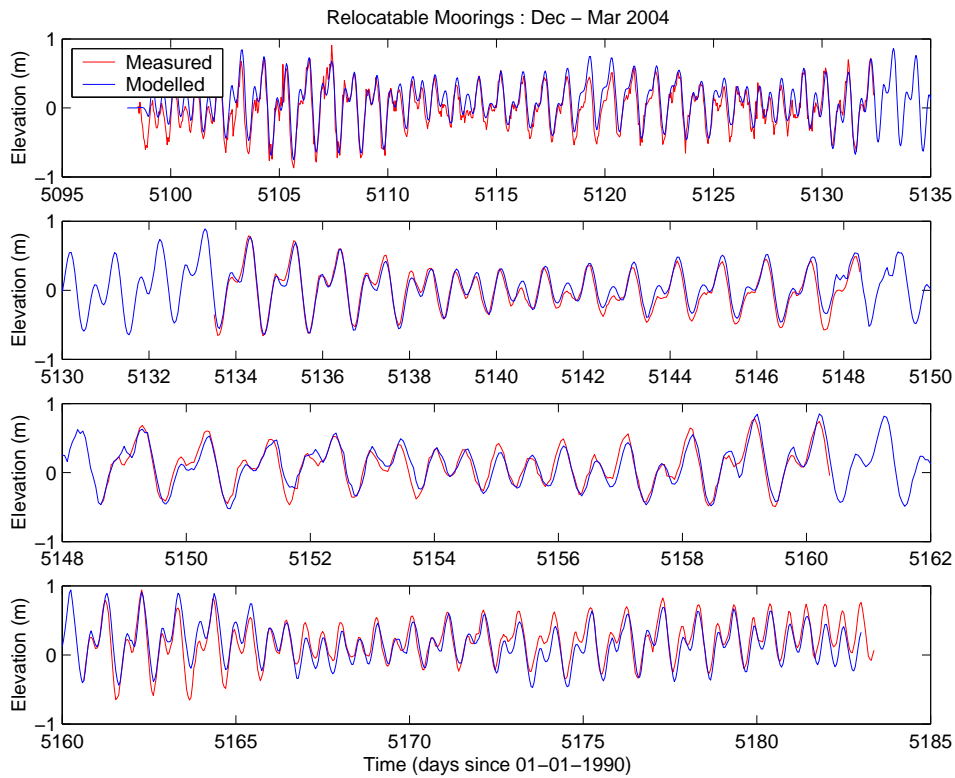


Figure 6.2.2 : Modelled and CTD sampled sea level

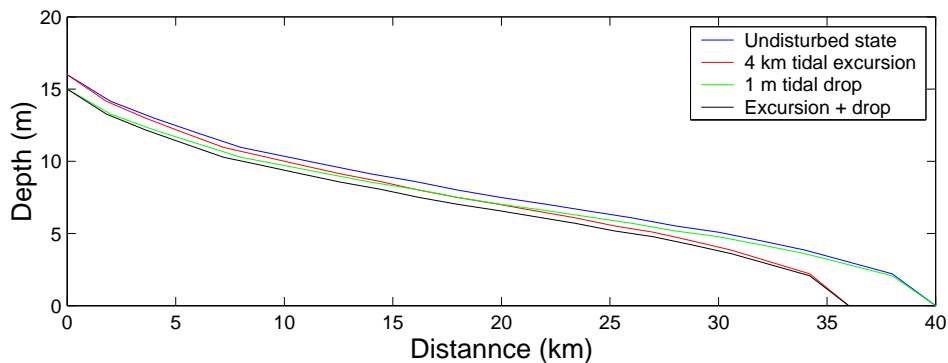


In Section 4 it was noted that the salinity and temperature signals exhibit diurnal oscillations at Elwick Bay and Bridgewater, where salinity may undergo changes of ~ 10 psu and temperature of $\sim 2^\circ\text{C}$ over the diurnal cycle (Figures 4.8 and 4.9 (a)). Maximum temperature and minimum salinity occur at low water (Figure 4.8 (a)). These oscillations decrease in magnitude closer to the bottom (Figure 4.5). Obviously the pycnocline must be moving past the location where the measurements were made for such large changes in T/S to be recorded. Purely vertical motion of the pycnocline due to its rise and fall with the tide cannot account for these salinity oscillations since the pycnocline is typically located at $\sim 2\text{m}$ and the maximum tidal range is $\sim 1\text{m}$, placing the maximum depth of the pycnocline well above the depth the oscillations were observed. Similarly, purely horizontal motion of the salt wedge head with the tidal excursion ($\sim 4\text{ km}$) is less than the distance between Elwick Bay and Bridgewater ($\sim 13\text{ km}$), where the oscillations were simultaneously observed, hence cannot explain this phenomena.

Keulegan (1966) performed laboratory experiments which revealed the shape of the salt wedge in terms of the ratios h/h_0 vs L/L_0 (where h is the height of the salt wedge at any location L along the wedge, and h_0 and L_0 are the height at the mouth and total length of the salt wedge respectively) are independent of river flow, mixing and river dimension (depth and breadth). Keulegan (1966), Table 11.1, tabulates these ratios, which can be used to construct a salt wedge so that the influence of horizontal tidal excursion (4 km), vertical drop in halocline depth due to tidal motion (1 m) and combination of these can be investigated (Figure 6.2.3). It is assumed the thickness of the wedge at the mouth is 16 m and the wedge propagates 40 km upstream. This scenario is of course idealized, where change in river geometry along the course of the estuary is unaccounted for (i.e. slope of the sea bed), however, it shows that the salt wedge interface is unlikely to pass through a point several meters above the bottom at locations 10 km or more downstream from the head of the wedge. Keulegan (1966, Eqn 11.78) also showed that the length of the salt wedge, L_0 , is dependent on river flow, depth at the tip of the wedge, density

differences between saline and fresh water and the Reynolds number. Prandle (1985, eqn 46) relates salt wedge intrusion for channels of constant breadth and depth to density difference, water depth, bottom stress, river flow, and tidal amplitude and period. It follows that the ratios L/L_0 and the height of the interface, h , are also dependent on these parameters. Prandle (1981) found that the salinity distribution is highly sensitive to the ratio of freshwater velocity and a longitudinal dispersion coefficient, and that cross-sectional area was a fundamental parameter in determining the estuarine mixing pattern. Farmer and Morgan (1953) examined estuaries of constant depth and breadth with no mixing between layers (i.e. stratified estuaries) and found that salt wedge thickness was dependent on interfacial Froude number (ratio of current speed to internal wave speed), water depth and drag coefficient. Ippen and Harleman (1961) found salt wedge intrusion lengths in partially mixed tidal estuaries was proportional to reduced gravity, river flow and energy dissipation rate. Dyer (1997) states that to obtain reasonable predictions of salt wedge length, the river flow, density difference between layers and bathymetry must be known with considerable accuracy. These studies indicate that salt wedge interface position is very sensitive to a number of parameters, which makes calibration difficult, since small variations in the mixing regime (bottom, interfacial and surface stress), tidal forcing, river flow and bathymetry can result in significant changes to the observed salinity pulses.

Figure 6.2.3 : Pycnocline movement with the tide



The displacement of the salt wedge interface over a tidal cycle can be observed in model salinity solutions of a transect along the estuary channel. Transects are shown at times of maximum flood (0.8m spring) and ebb (-0.43m) during a flow of $\sim 56 \text{ m}^3\text{s}^{-1}$ in Figures 6.2.4 and 6.2.5 respectively. The halocline shows large displacement at Elwick Bay (at approximately 13.5km along the transect) and Bridgewater (0.25km along the transect) with associated salinity changes of ~ 3 and 15 psu respectively. Note the 28psu contour has been displaced by $\sim 4\text{km}$ horizontally. As noted above, it is unlikely tidal oscillation of the interface is responsible for this large variation and there must be another mechanism present responsible for moving the halocline past the CTD location. This is investigated in the next section.

Figure 6.2.4 : Salinity transect at flood tide

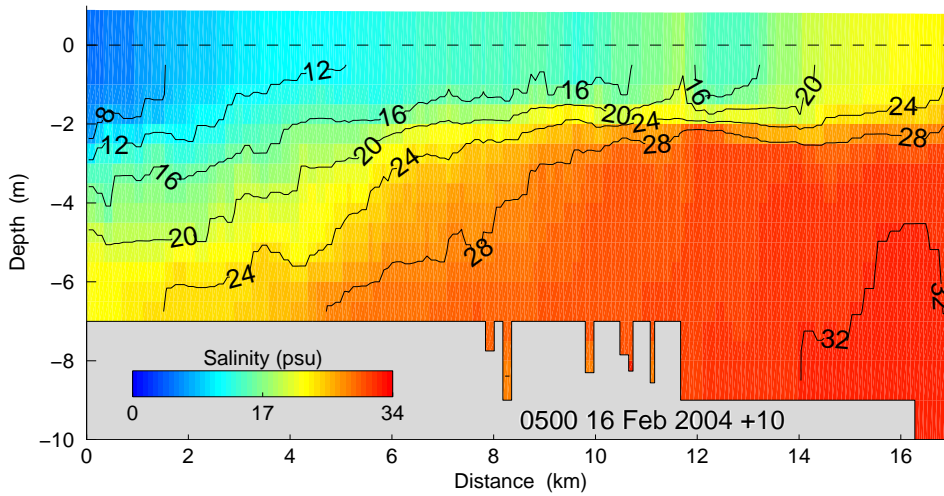
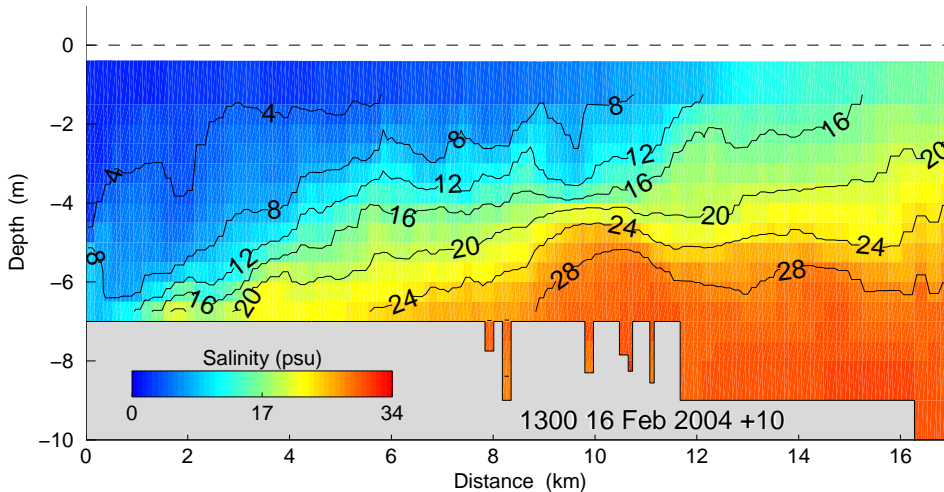


Figure 6.2.5 : Salinity transect at ebb tide



The temperature and salinity from the calibrated model simulation are compared to measured time series data in Figure 6.2.6 and 6.2.7 respectively. Note that the Iron Pot site is too close to the open boundary to be of much use for comparison purposes. The general trends captured in the measurements are evident in the model solutions. Temperature and salinity compare well to observation at Sandy Bay. Further up-river the amplitude and maximum of the T/S oscillations are underestimated, especially for salinity. If the modelled time series were taken higher in the water column (by 1.67m) at Elwick Bay, then solutions improve, emphasizing the critical positioning of the pycnocline (Figure 6.2.8). Maximum salinity also appears slightly low in bottom layers at Elwick Bay and Bridgewater. These discrepancies are most likely due to under-specified forcing (e.g. wind and its impact on mixing, depth distribution of T/S at the open boundary) and incorrect bathymetry. However, the low salinity pulses are evident in the solutions and show good phase agreement with the measurements.

Figure 6.2.6 : Modelled and measured temperature solutions

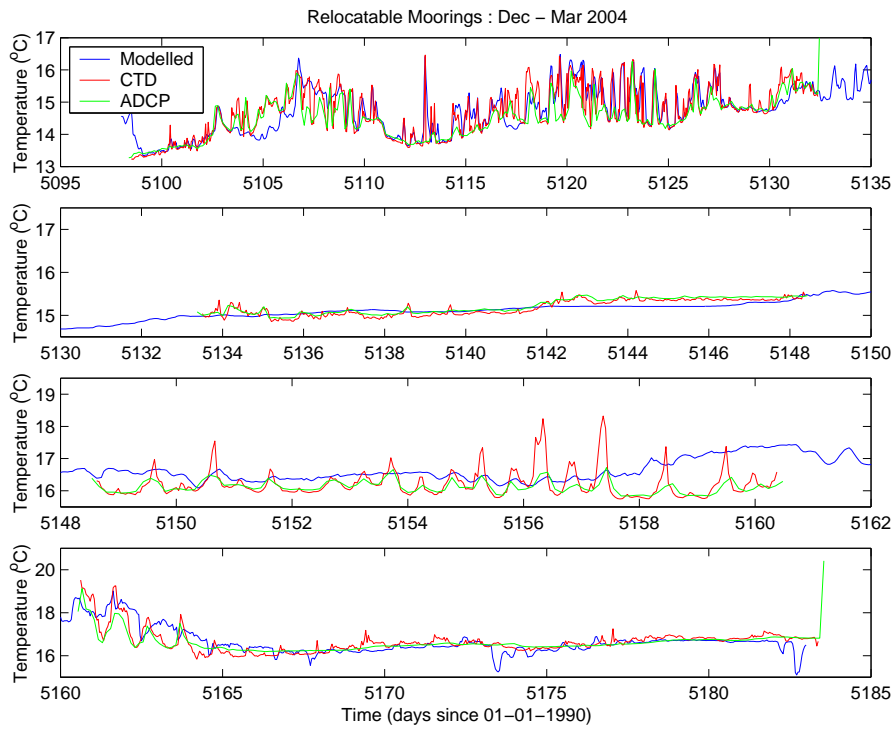


Figure 6.2.7 : Modelled and measured salinity solutions

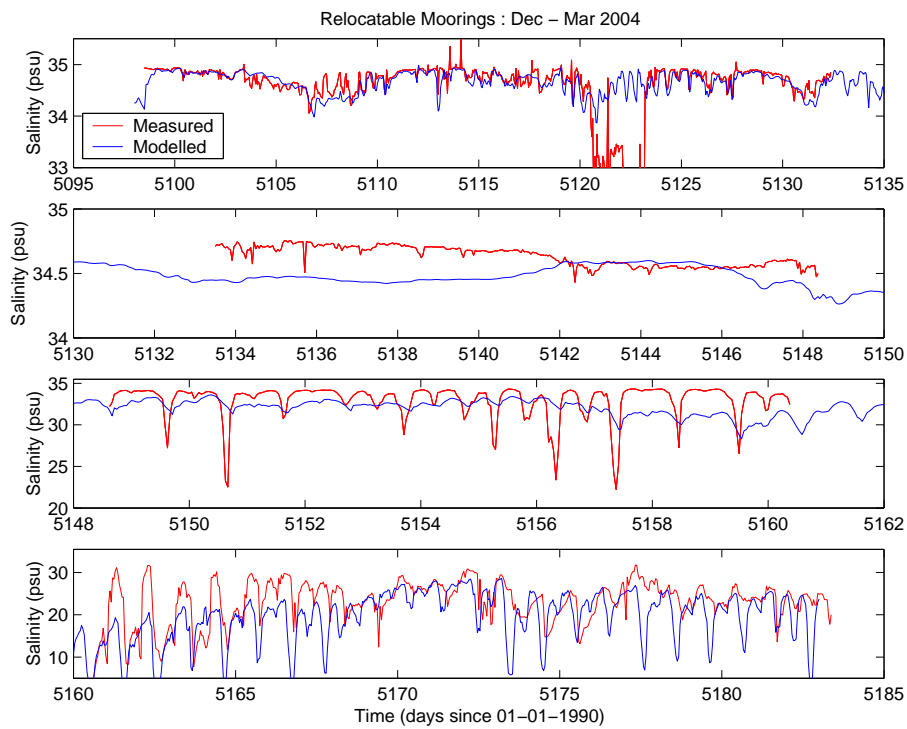
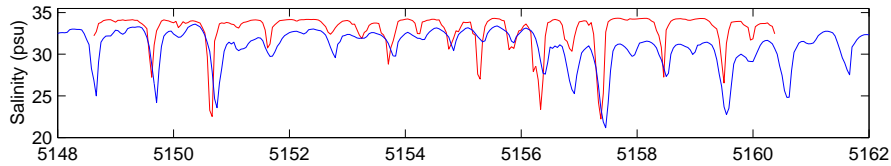
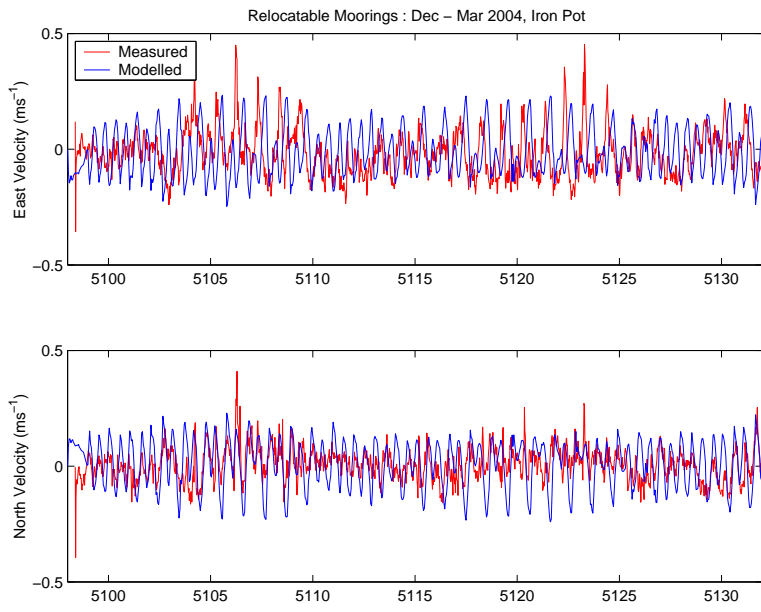


Figure 6.2.7 : Modelled and measured salinity solutions at Elwick Bay.
Modelled data taken at 4.75m depth.

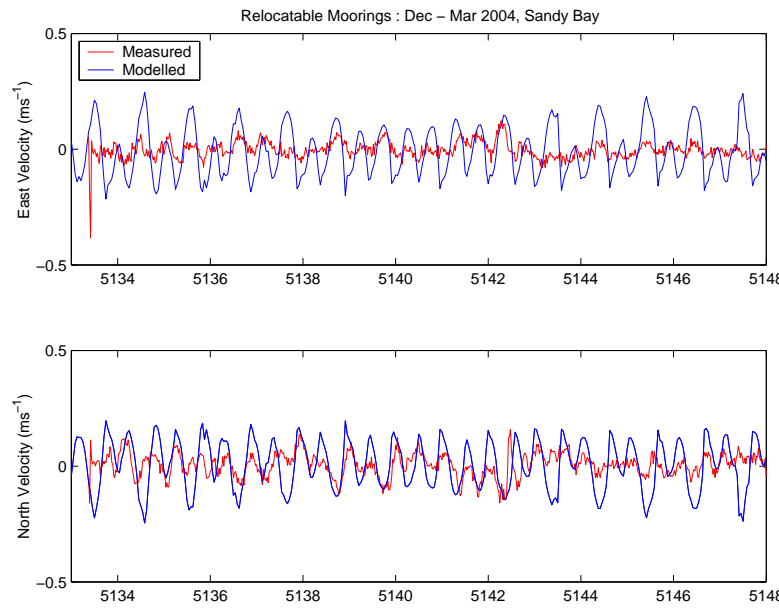


Modelled and measured velocities are shown in Figures 6.2.8 (a) – (d) for each of the sampling sites respectively. Velocity is overestimated at Sandy Bay and north / south velocity underestimated at Bridgewater. The latter is not surprising, since the resolution of the model did not allow as narrow a constriction at the causeway as was required, and consequently flow is not channelled to as large a degree. Current speed at other sites compares reasonably to measurement, and again there is good phase correlation. Velocity comparisons present a tough test, since velocity is usually influenced by small temporal and spatial scale processes (e.g. high frequency wind variations, bathymetry gradients and small scale turbulent mixing) that cannot be captured by the model. The larger scale fields of temperature and salinity, whose distribution is controlled more by the large scale transport processes constitutes a more robust comparison measure. Nevertheless, the model does a reasonable job of reproducing in-situ velocity.

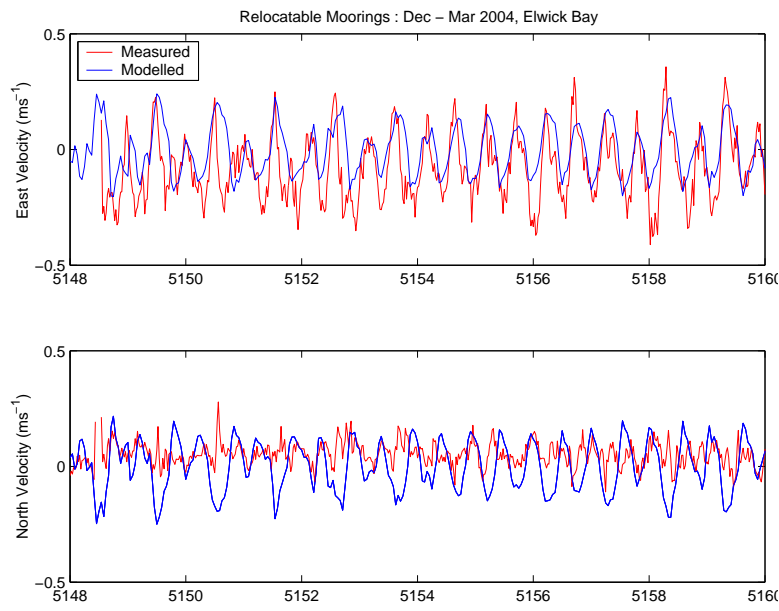
Figure 6.2.8 : Modelled and measured velocity
(a) Iron Pot



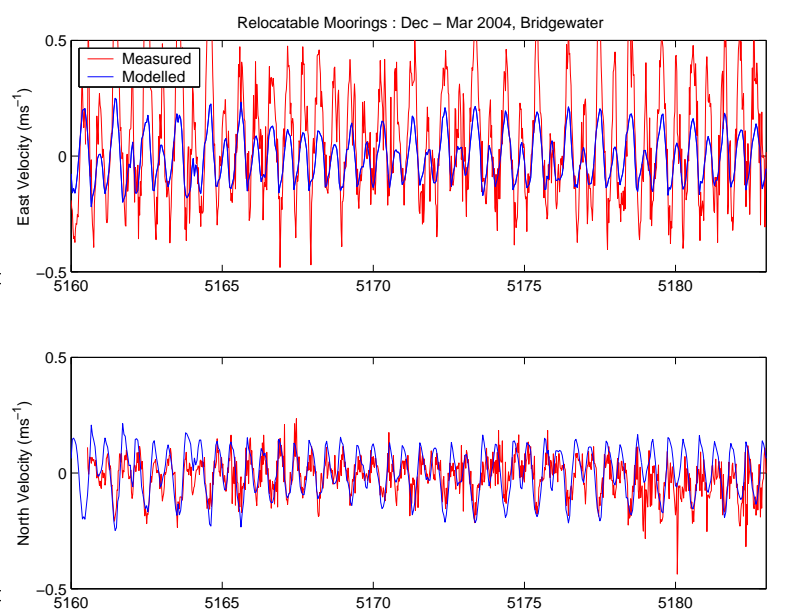
(b) Sandy Bay



(a) Elwick Bay



(b) Bridgewater



6.3 Sensitivity

During the calibration procedure an assessment of the sensitivity of model parameters and processes was made. The model was found to be most sensitive to bathymetry changes, surface heat flux, background vertical viscosity and horizontal viscosity. Without a surface heatflux imposed the temperature solution compared unfavourably with observation. Temperature solutions compared well to observation when a heatflux was included using the bulk scheme of Kondo (1975) with non-depth dependent shortwave radiation input. Changes in background vertical viscosity altered the absolute salinities and magnitudes of salinity oscillations, with larger coefficients decreasing the salinity and increasing the oscillation at Elwick Bay (Figure 6.3.1). The model was relatively insensitive to changes in background vertical diffusivity (Figure 6.3.2). Similarly low sensitivity was observed to changes in bottom friction, although these parameters affected the stability of the model. Horizontal friction affected both stability and accuracy, with higher viscosity resulting in lower salinity at Bridgewater (Figure 6.3.3). A Smagorinsky formulation of horizontal mixing coefficients (i.e. shear dependent formulation rather than a constant) was used with a scaling parameter of 0.5 which gave the best overall calibration. Lowering this scaling parameter effectively lowered horizontal mixing, with a corresponding increase in salinity at Bridgewater (Figure 6.3.4). The mixing scheme used was the Mellor-Yamada level 2.0 scheme (Mellor and Yamada, 1982); using more sophisticated schemes either resulted in instability or an unfavourable calibration (Figure 6.3.5 using $k-\omega$, Umlauf *et al*, 2003). The depth of the main channel in the upper estuary influenced the propagation of the salt wedge upstream, hence the magnitude of bottom salinity at Bridgewater. A channel one cell wide of depth 7m was required to be included in order for the salt wedge to propagate sufficiently well upstream (compare Figure 6.3.6 and 6.3.7).

Figure 6.3.1 : Salinity calibration with high background vertical viscosity

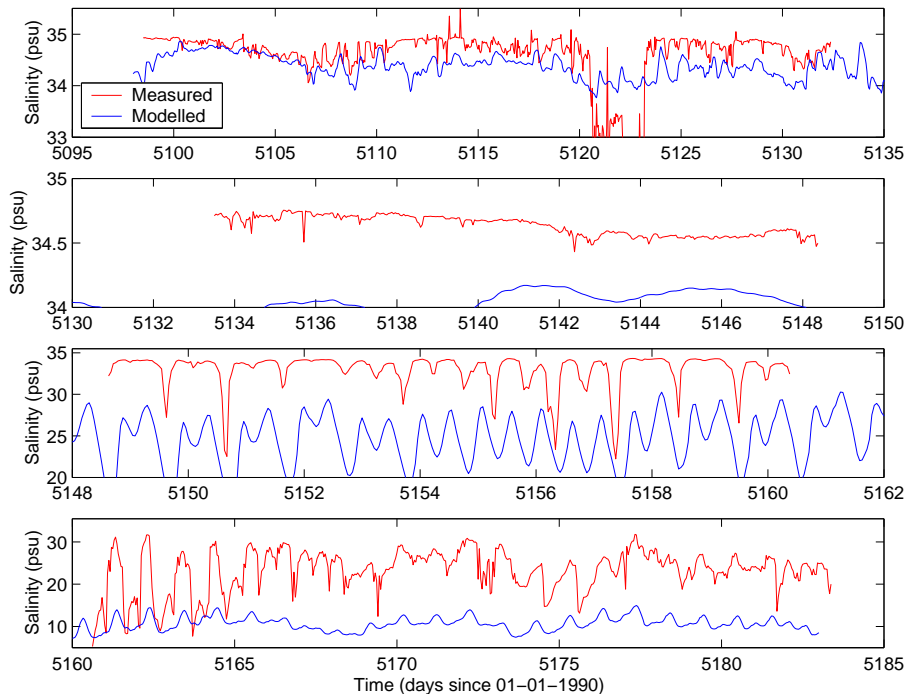


Figure 6.3.2 : Salinity calibration at Elwick Bay with variable background vertical diffusivity
(a) $K_z = 1 \times 10^{-6} \text{ m}^2 \text{ s}^{-1}$

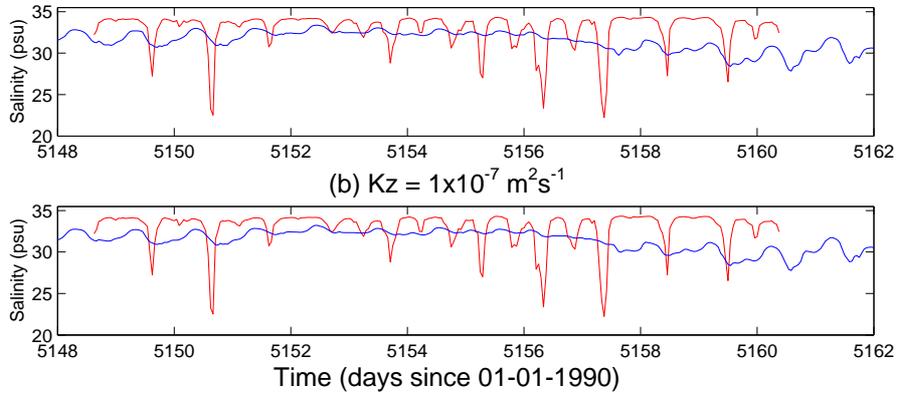


Figure 6.3.3 : Salinity calibration at Bridgewater with variable horizontal viscosity
(a) $AH = 15 \text{ m}^2 \text{ s}^{-1}$

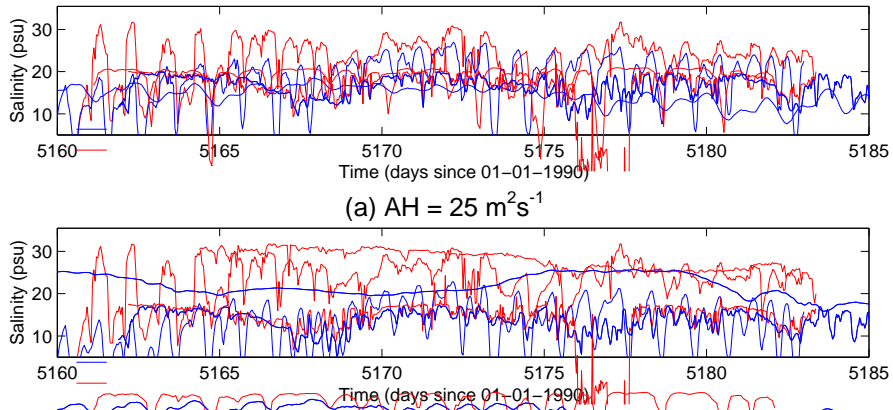


Figure 6.3.4 : Salinity calibration at Bridgewater with Smagorinsky horizontal viscosity
(a) $c = 0.5$

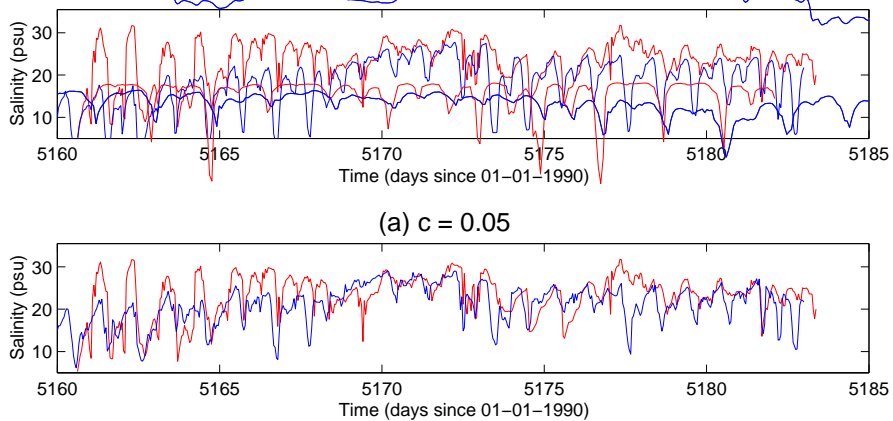


Figure 6.3.5 : Salinity calibration using k- ω mixing scheme

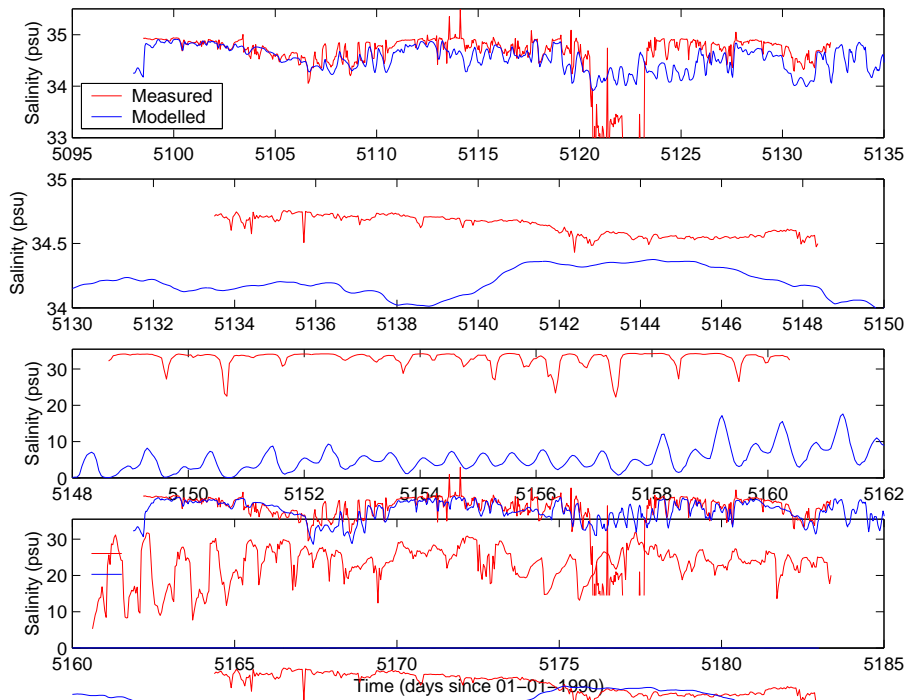


Figure 6.3.6 : Salinity at Elwick Bay and Bridgewater using bathymetry depicted in Figure 5.5.2 (b)

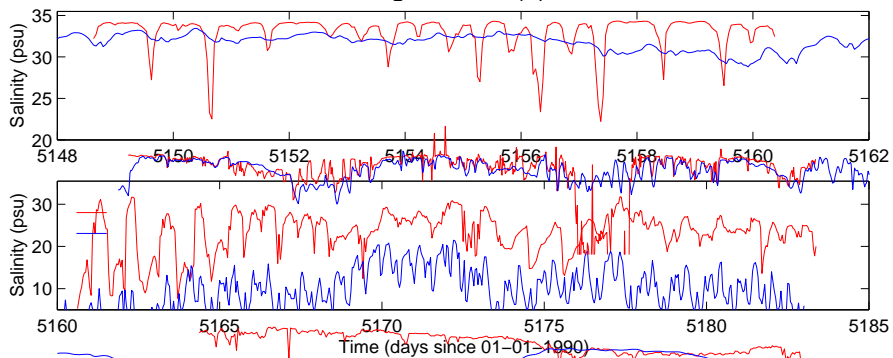
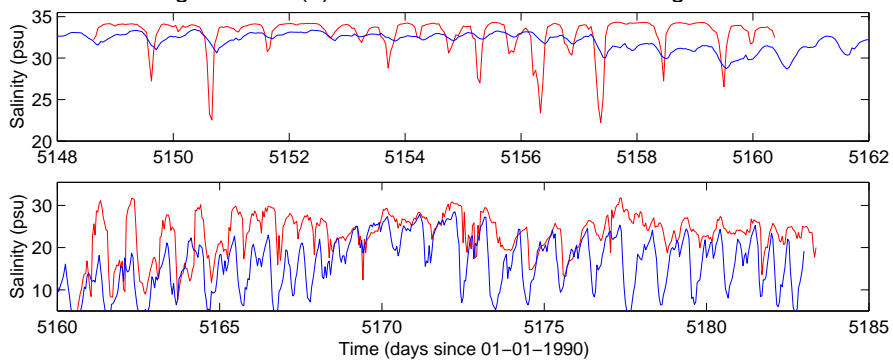


Figure 6.3.7 : Salinity at Elwick Bay and Bridgewater using bathymetry depicted in Figure 5.5.2 (b) with 7m main channel to Bridgewater



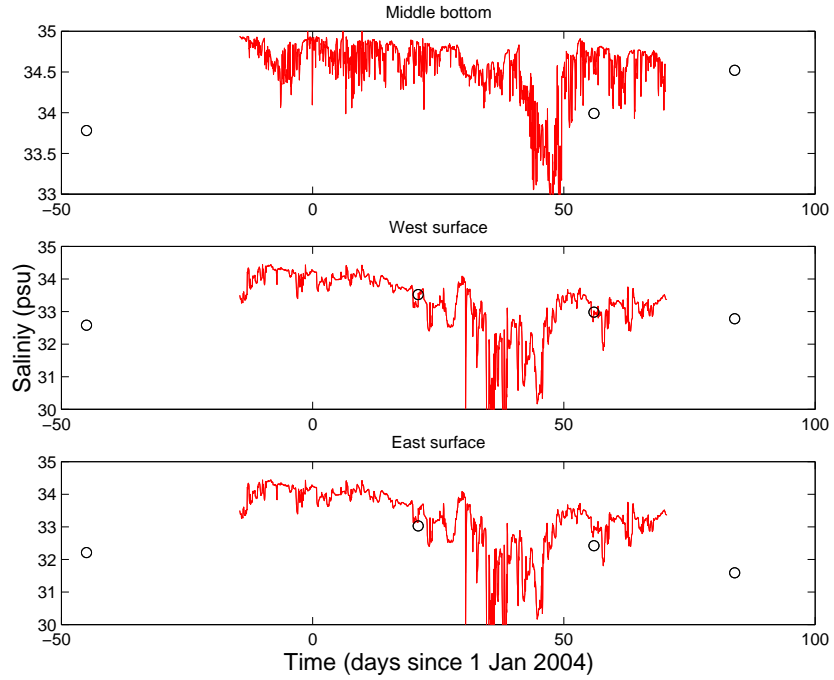
6.4 Annual simulations

Simulations of longer duration are desirable when analysing sediment transport and contaminant dynamics, since these processes are associated with long timescales. DPIWE have collected temperature and salinity data (referred to as DPIWE data) on an approximately monthly basis for several years and these data are suitable for forcing the Iron Pot open boundary. Temperature and salinity are linearly interpolated in time to obtain values at every model time-step, thus due to the coarse temporal frequency of these data the model calibration is expected to be somewhat compromised. This becomes evident when comparing the DPIWE data with T/S data collected from the Dec 03 – Mar 04 field campaign (referred to as CSIRO data) in Figure 6.4.1. The DPIWE data shows good correlation with the CSIRO data, however it is apparent that a linear interpolation between the DPIWE data can introduce significant error at certain times, especially during times of flood when salinity becomes low and the event is not captured by a monthly sample.

The temperature and salinity derived from the model using the DPIWE data as T/S boundary conditions is compared to the CSIRO data in Figure 6.4.2. The calibration suffers near the Iron Pot boundary where model salinity is too low. The lack of temporal structure, tending towards a linear variation, is evident in the top panels of Figures 6.4.2, a direct result of the temporal linear interpolation used on the DPIWE data. Further upstream the calibration improves, reflecting dynamics that are not directly controlled by transport effects of T/S near the open boundary; e.g. freshwater inflow, salt wedge propagation and entrainment. This simulation was run from 1 Jan 2003 to 11 Mar 2004, and is suitable for investigations of dynamics on longer timescales.

Figure 6.4.1 : Comparison of continuous sampled T/S (red line) with monthly DPIWE data (black circle).

(a) Salinity



(b) Temperature

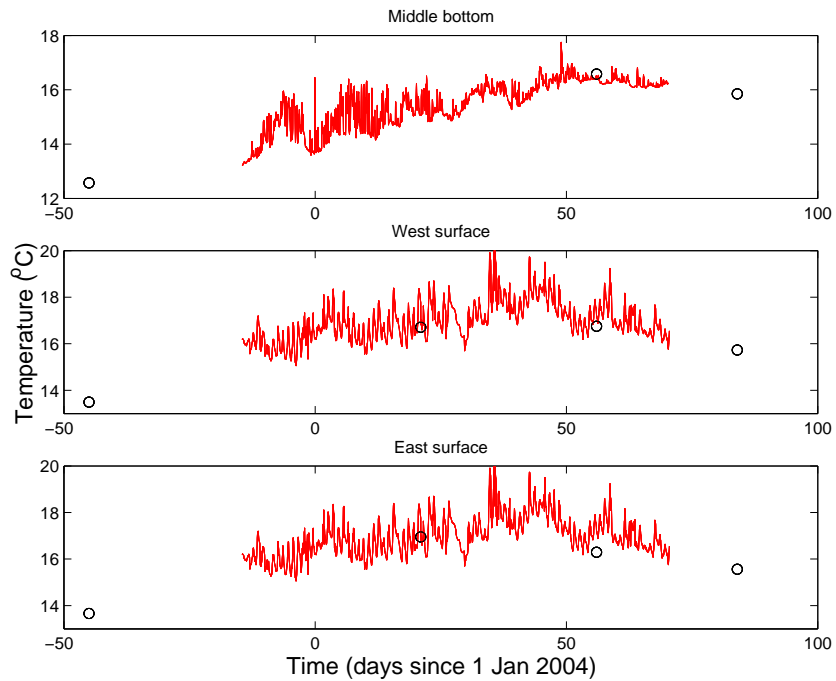
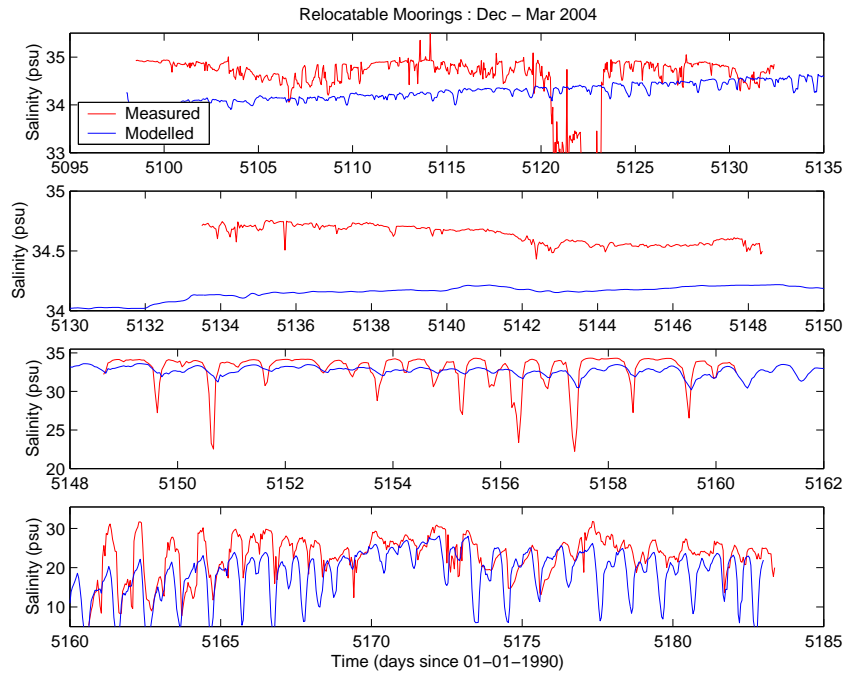
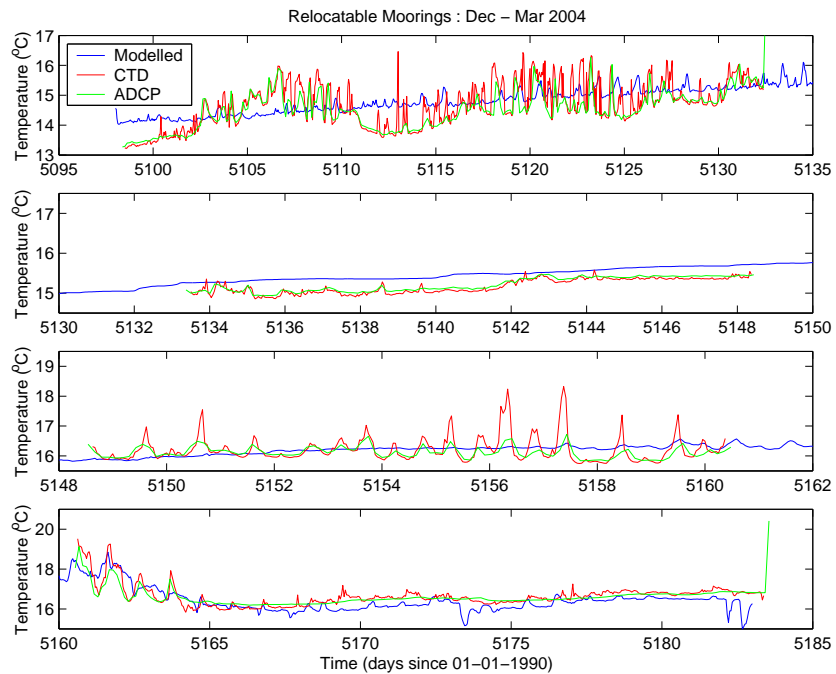


Figure 6.4.2 : Model calibration using DPIWE data
(a) Salinity



(b) Temperature



7. Model Solutions

7.1 General Solutions

Figures 7.1.1 and 7.1.2 show snapshots of the surface salinity and current distribution during low and high flow conditions respectively. It is observed that the fresh water plume extends much further downstream under high flow into the lower estuary, as expected. Under low flow conditions a surface reversal of the currents is seen during the tidal period but this is absent under high flow since the river discharge overwhelms the tidal flow. However, the maximum extent of the freshwater plume does extend further downstream when aided by the ebb tide. Currents are stronger under both flow conditions on the ebb tide. This is the combination of tidal and river flow combining on the ebb, and the ebb tide being stronger and shorter than the flood due to the mixed diurnal character of the tide (e.g. the flood tide often turns midway through its phase, Figure 6.2.2).

The bottom salinities and currents are displayed for low and high flow conditions respectively in Figures 7.1.3. and 7.1.4. High salinity is observed in the deeper sections of the estuary well into the upper estuary, corresponding to the propagation of the salt wedge upstream. Under high flow the salt wedge is pushed further downstream into the middle estuary. Currents are predominantly upstream in the bottom waters.

A section along the deepest part of the middle estuary is displayed in Figure 7.1.5 at four times from spring tide high water to spring tide low water. The distances along the transects are displayed in Figure 7.1.6 for reference. At high water the halocline is relatively smooth and tight in vertical extent at a distance 14 – 16km along the transect. As the tide ebbs the halocline becomes perturbed, with the halocline undergoing undulations similar to a mode 1 internal wave (e.g. 6-10km Figure 7.1.5(b)) or expanding in the vertical similar to a mode 2 internal wave (e.g. 12.5km Figure 7.1.5(d)). The latter phenomenon is observed in a time series over a spring tidal cycle at 12km (Figure 7.1.7), where the vertical distance between 20 and 28 psu contours has doubled at low water compared to high water. This downward movement and opening of the halocline effectively decreases salinity near the bottom and is responsible for the periodic decreases in salinity observed in Figures 4.8 and 4.9. At neap tide this phenomena is not observed (Figure 7.1.8), indicating strong flows are required to induce this perturbation. Similarly the perturbations are not observed on the flood tide which is weaker than the ebb.

The exact mechanism responsible for these perturbations is unclear, but several possibilities can be discounted. Internal waves at the tidal frequency (i.e. internal waves forced by the tide; internal tides) cannot be responsible since these have a frequency bounded by the inertial frequency (Gill, 1982, p259), f ($f = \text{Coriolis parameter} \sim -9.91 \times 10^{-5} \text{ s}^{-1}$ at $42^{\circ}50'S$ giving inertial period $T = 2\pi/f \sim 17.6$ hours). The tide is mixed diurnal in the Derwent estuary with the halocline perturbations occurring on the diurnal tidal period (~24 hours, which is greater than the 17.6hr limit), hence forced internal tides are not possible at the latitude of the Derwent estuary.

Bathymetry does play a role in the generation of the perturbations, since running the model with a constant 10m bathymetry in the upper and middle estuary removes the perturbations (Figure 7.1.9). Similarly, running the model with no momentum advection also removes these perturbations (Figure 7.1.10) indicating non-linear processes are important. Furthermore, the perturbations are unlikely to be the result of lee waves generated by flow over topography, since a simulation using uniform bathymetry of 7m in the deepest part of the channel still resulted in the formation of the perturbations (Figure 7.1.11). This was repeated using a 10m channel below 14km (Figure 7.1.12), and it can be observed that a 3m change in bathymetry results in minimal perturbations due to lee waves in comparison with the perturbations at 5km where the channel is

flat. Finally a simulation was performed with uniform 5m bathymetry above Bowen Bridge with a 7m deep channel (Figure 7.1.13), and it is observed the perturbations are again subdued, indicating that the cross-river bathymetry plays a role in the generation mechanism.

The generation of these perturbations is hypothesised to be due to enhanced secondary cross channel circulation induced by compound (stepped) bathymetry on curved channels (Shao and Chen (2003), Blanckaert and Graf (2001)) resulting in vertical advection of the halocline. These secondary circulations are found in straight channels, but are enhanced by curvature. This hypothesis is consistent with the importance of nonlinear momentum advection, which is responsible for momentum exchange at interfaces between changes in bathymetry. It is also observed that the halocline perturbations are consistently located in the proximity of bends in the channel, supporting the idea of curvature enhanced secondary flow (Figure 7.1.11(c) shows enhanced flow around bends). These types of flow may be associated with velocities of 20 – 30% of the along-stream velocity (Shao and Chen, 2003). Flow in a curved channel typically has surface flow towards the outer bank and bottom flow towards the inner bank. A channel with compound bathymetry has two cross-river circulation gyres generated by pressure and turbulent stress forces that converge at the bathymetry step to result in upwelling, with downwelling towards the boundaries of the channel. The exact configuration of the gyres is dependent on channel depths, widths and curvature of the bend. The enhanced vertical motions resulting from the secondary flow may significantly alter the position of the halocline. Under maximum downstream flow conditions (e.g. ebb on a spring tide) when the secondary circulations are maximum, the halocline may be sufficiently downwelled at certain locations to result in the observed perturbations. The regions of vertical flow, and associated movement of the halocline, can be observed in Figure 7.1.11 (b). It was difficult to emulate this phenomena with idealized topography, which suggests the secondary circulation may be critically dependent on the cross-river bathymetry.

Figure 7.1.1 : Dec 27 surface velocity and salinity
 (a) Low flow conditions ($\sim 30 \text{ m}^3 \text{ s}^{-1}$) Flood tide (range $\sim 1.1 \text{ m}$)
 (b) Low flow conditions ($\sim 30 \text{ m}^3 \text{ s}^{-1}$) Ebb tide (range $\sim 1.1 \text{ m}$)

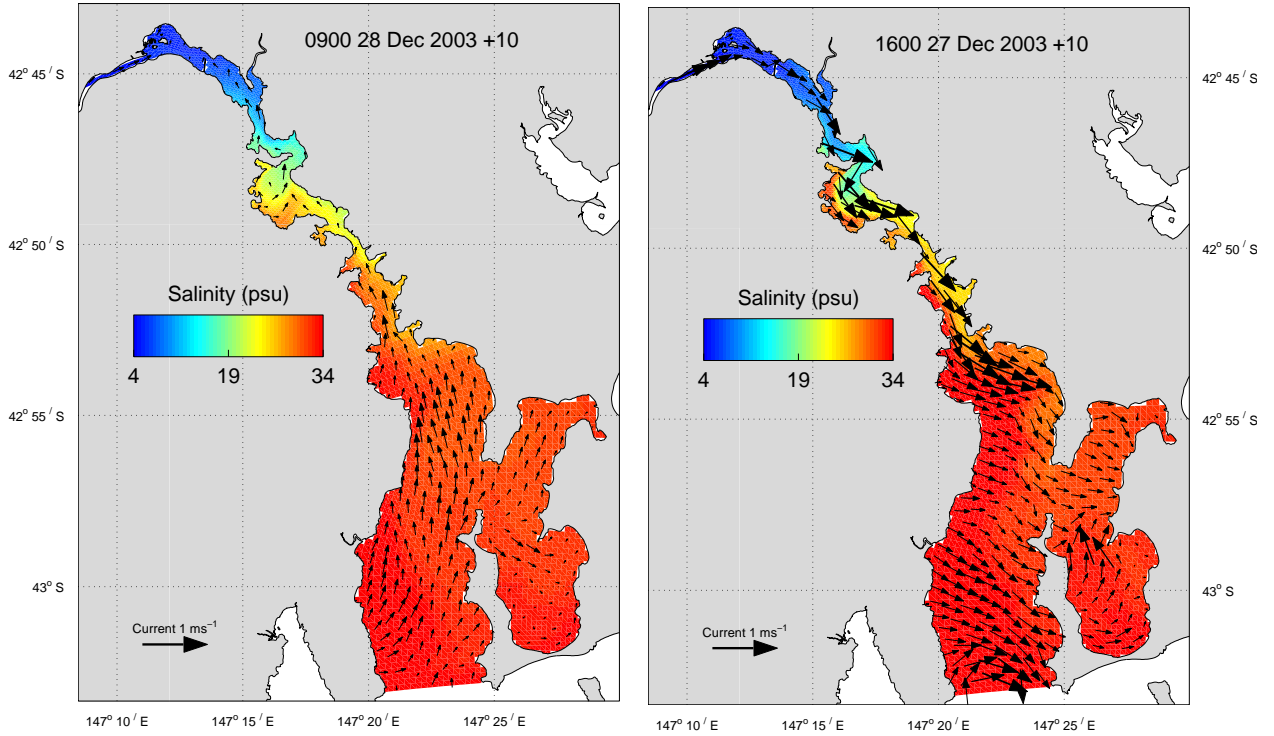


Figure 7.1.2 : Jan 31 surface velocity and salinity
 (a) High flow conditions ($\sim 180 \text{ m}^3 \text{ s}^{-1}$) Flood tide (range $\sim 1.0 \text{ m}$)
 (b) High flow conditions ($\sim 180 \text{ m}^3 \text{ s}^{-1}$) Ebb tide (range $\sim 0.93 \text{ m}$)

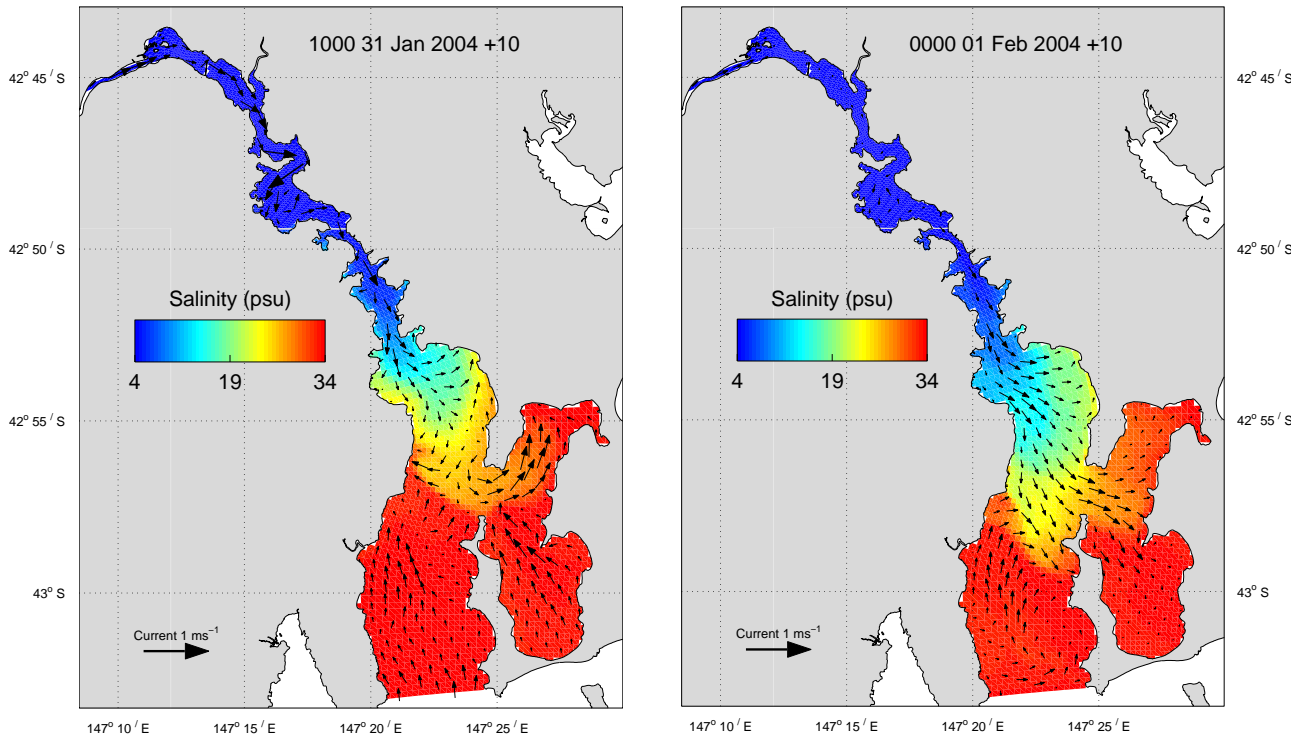


Figure 7.1.3 : Dec 27
Bottom salinity and currents
Low flow ($\sim 30 \text{ m}^3 \text{ s}^{-1}$)

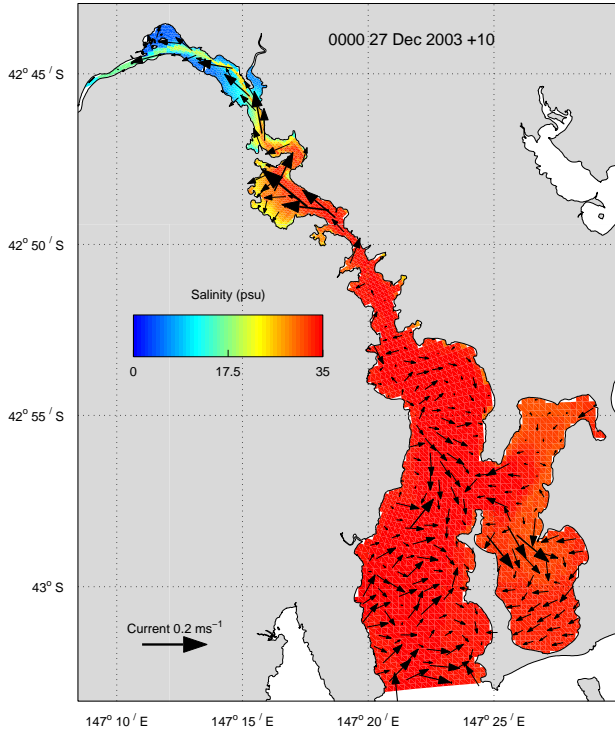


Figure 7.1.3 : Jan 31,
Bottom salinity and currents
High flow ($\sim 180 \text{ m}^3 \text{ s}^{-1}$)

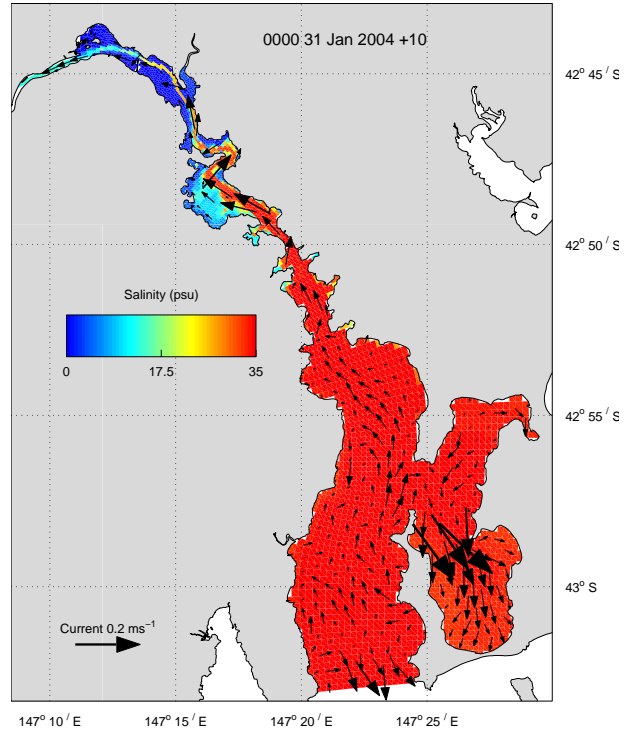


Figure 7.1.5 (a) : Salinity 0800 5th Feb : Spring tide high water

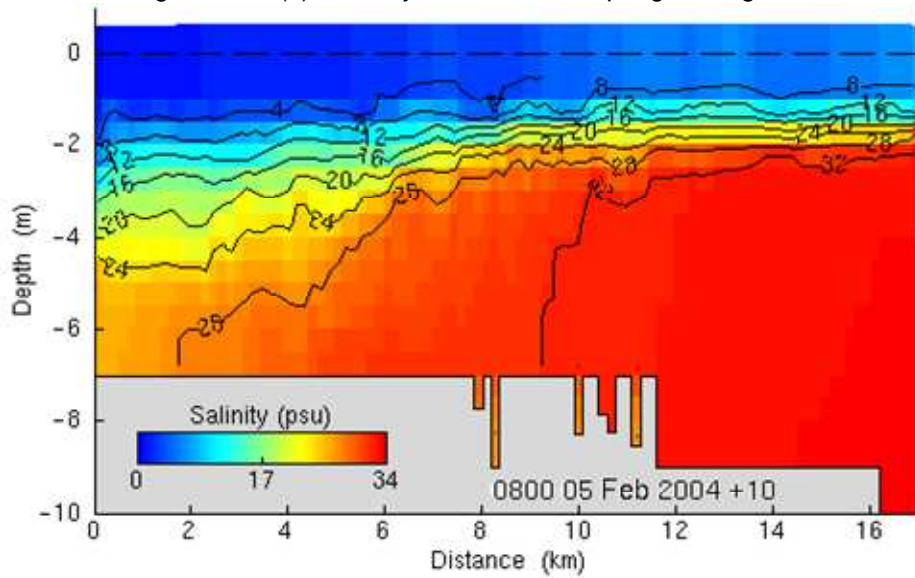


Figure 7.1.5 (b) : Salinity 1100 5th Feb

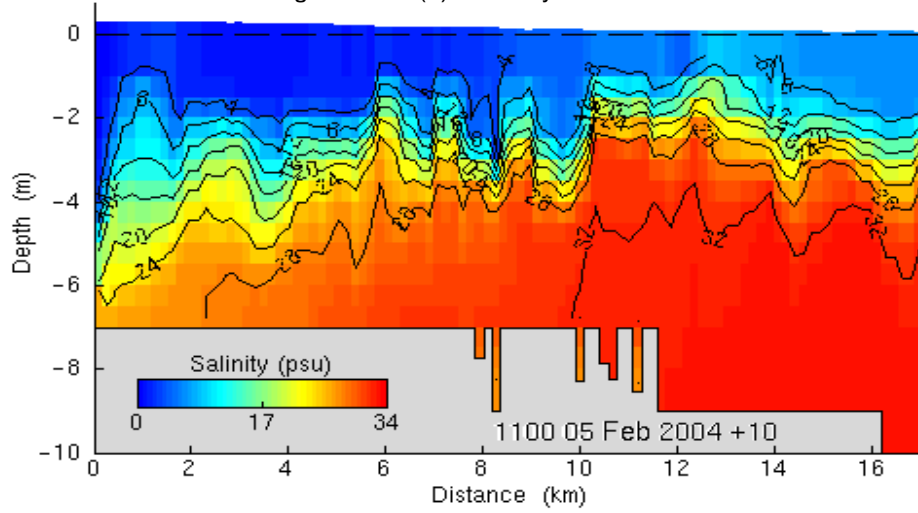


Figure 7.1.5 (c) : Salinity 1300 5th Feb

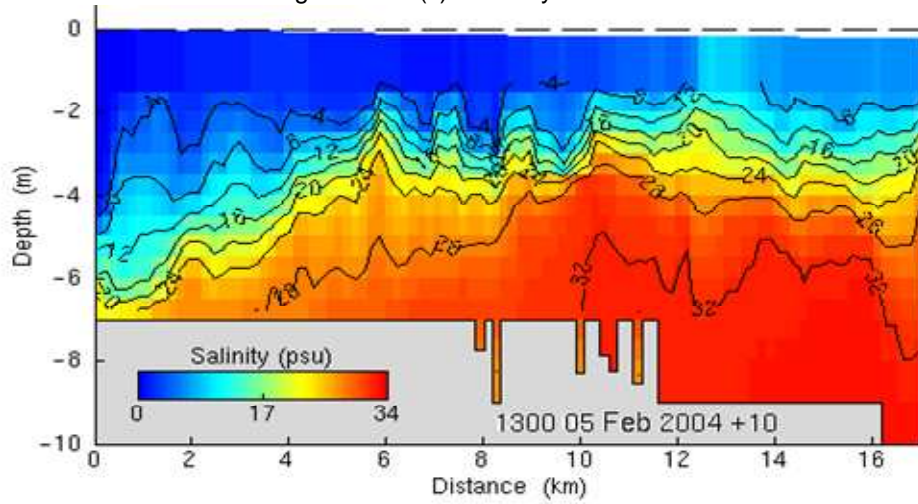


Figure 7.1.5 (d) : Salinity 1500 5th Feb : Spring tide low water

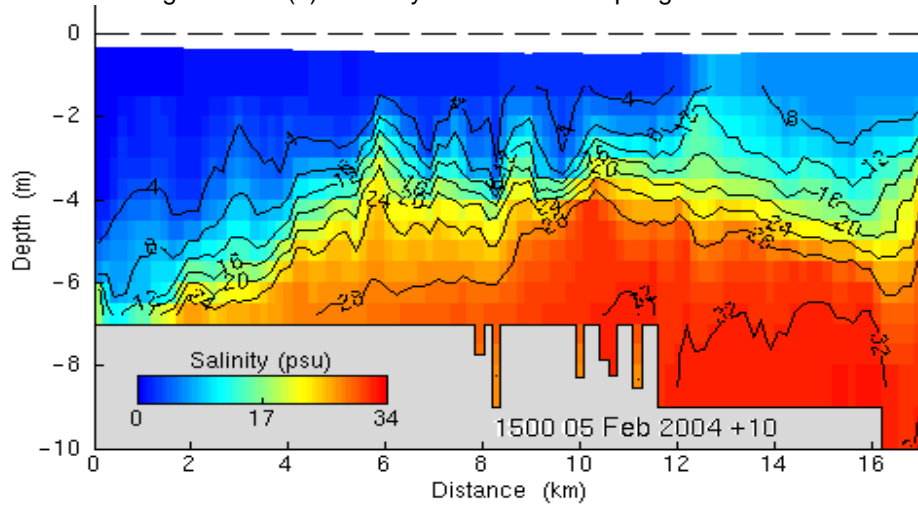


Figure 7.1.6 : Marker distances

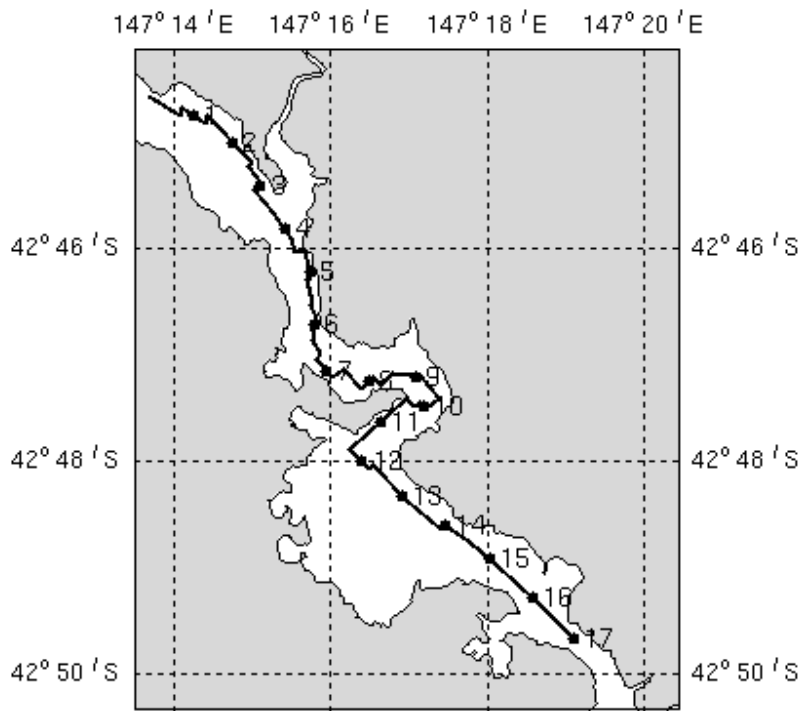


Figure 7.1.7 (a) : Salinity time series at ~12km, 17th Feb : Spring tide

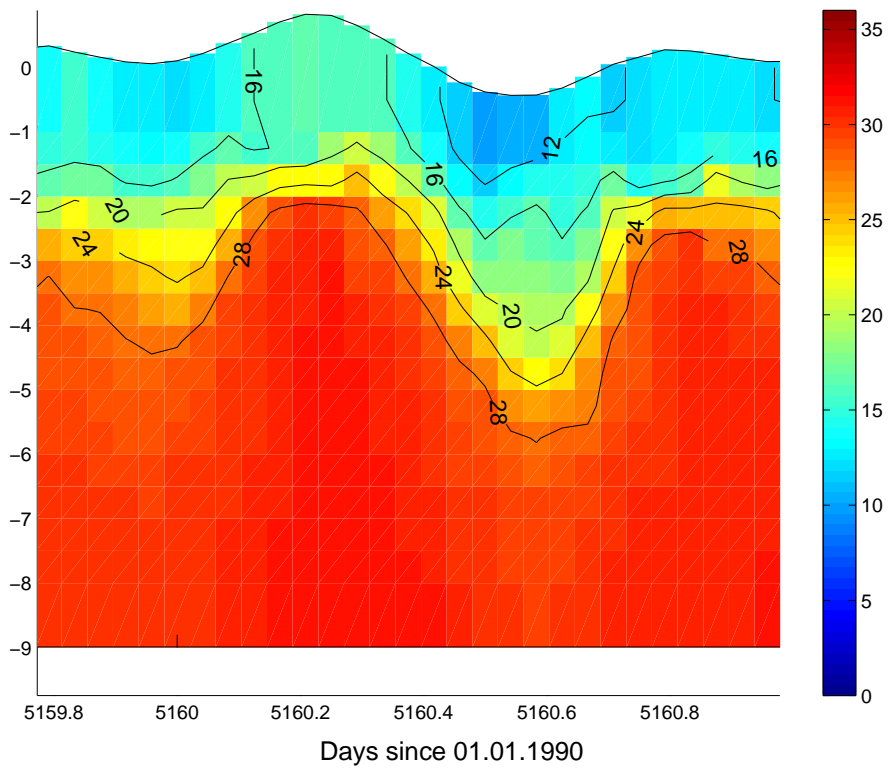


Figure 7.1.8 : Salinity section at neap tide
 (a) 1400 12th Feb : high water (b) 2000 12th Feb low water

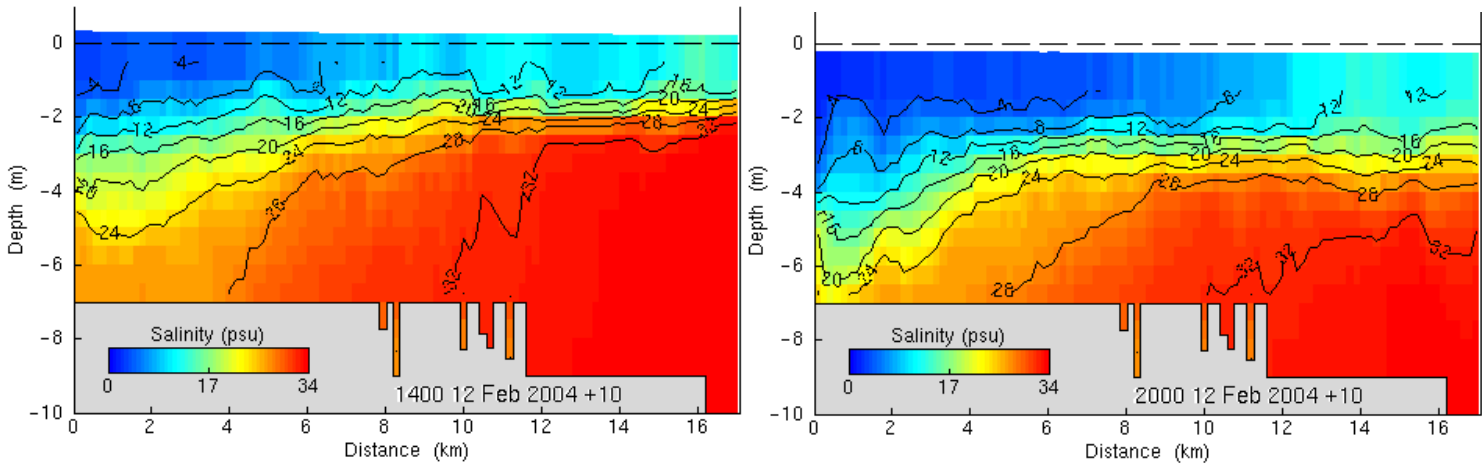


Figure 7.1.9 : Salinity 0800 5th Feb : 10m bathymetry
 (a) Spring tide high water (b) Spring tide low water

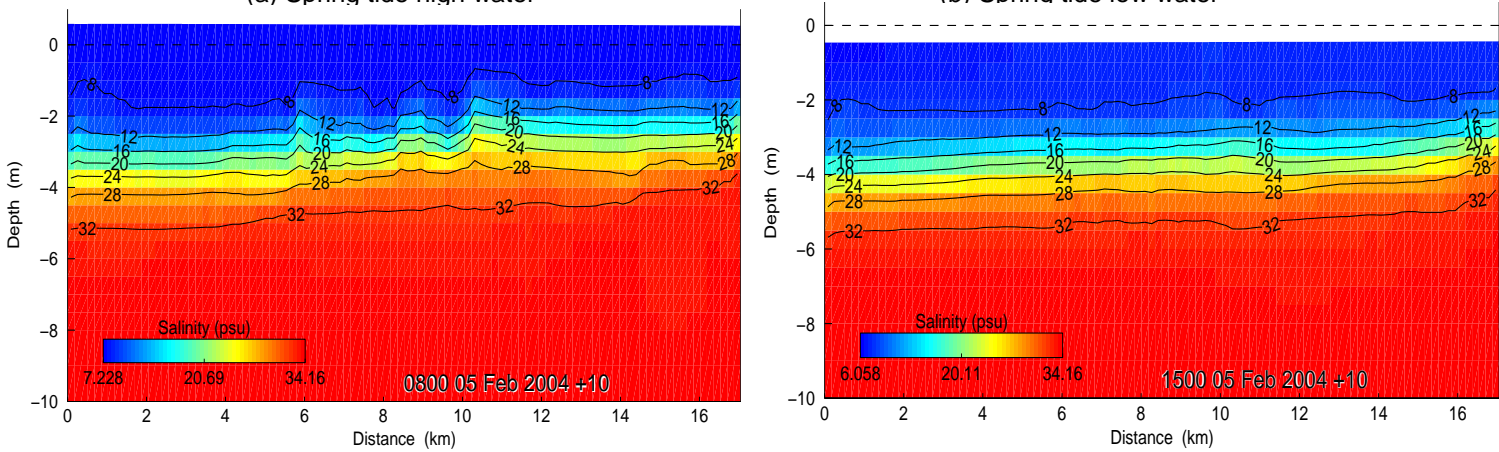


Figure 7.1.10 (a) : Salinity section with no advection : spring tide low water

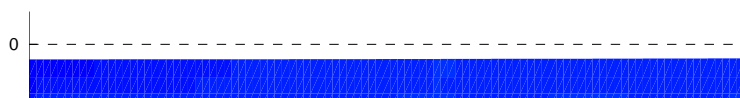
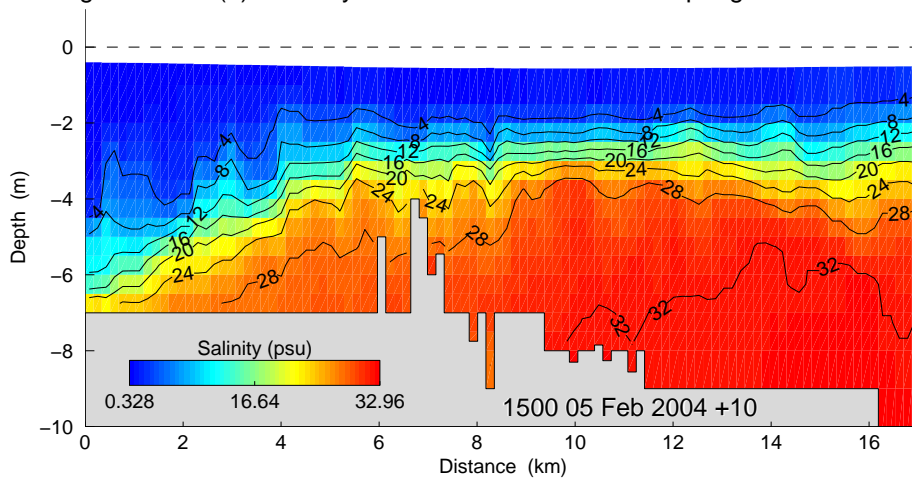


Figure 7.1.11 (a) : Salinity section with uniform 7m channel : flood tide low water

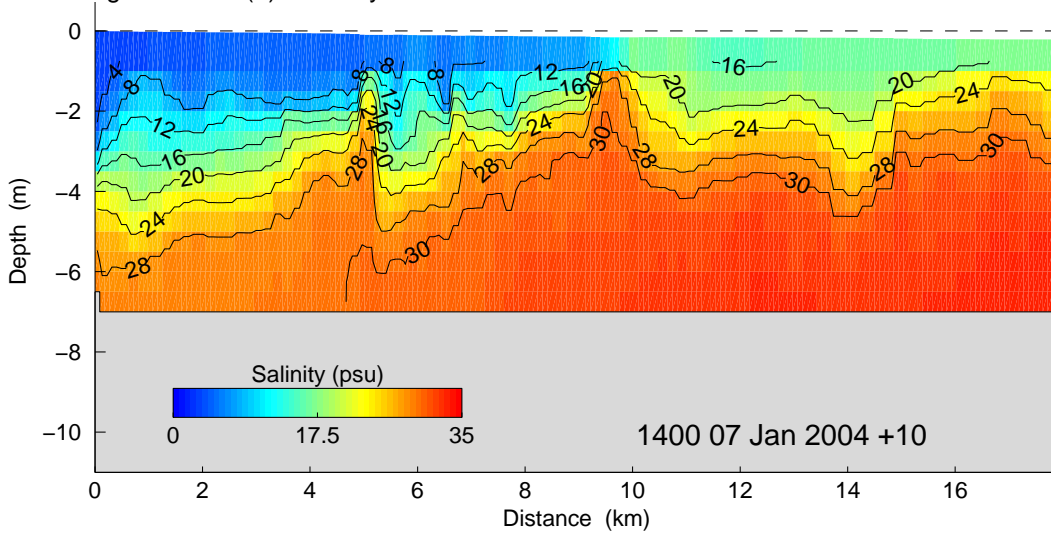


Figure 7.1.11 (b) : Salinity and velocity cross section with uniform 7m channel

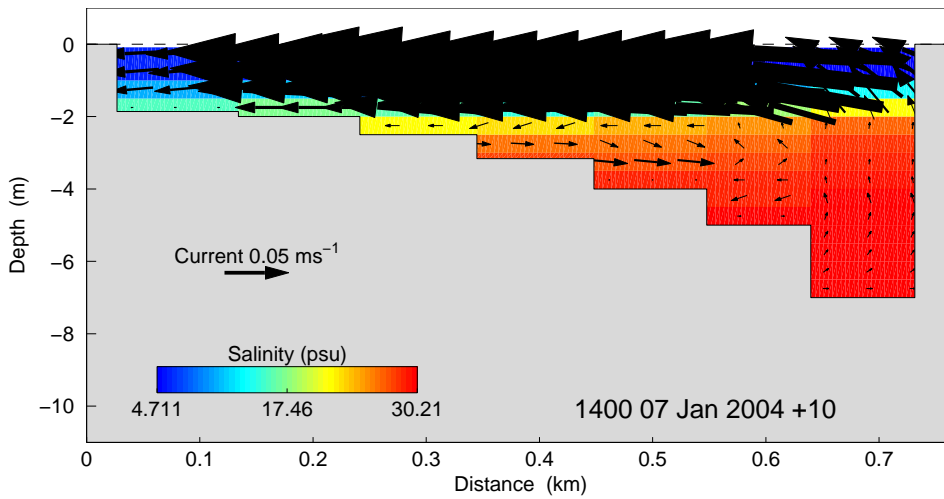


Figure 7.1.11 (c) : Salinity and velocity plan with uniform 7m channel

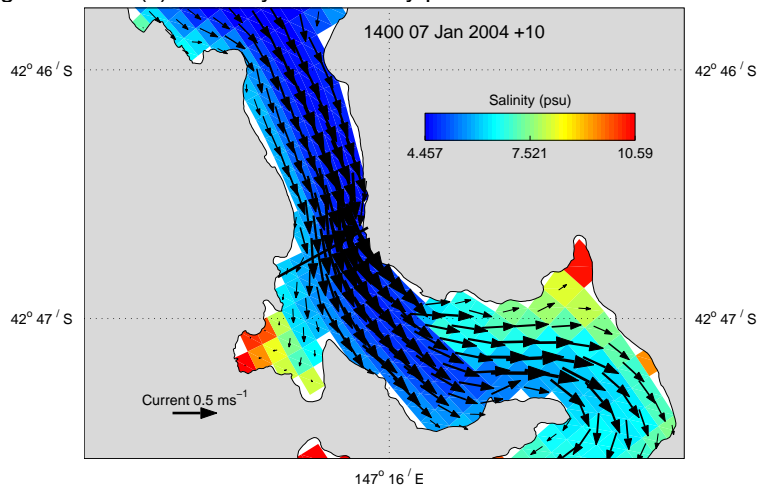


Figure 7.1.12 : Salinity section with uniform 7 & 10m channel : flood tide low water

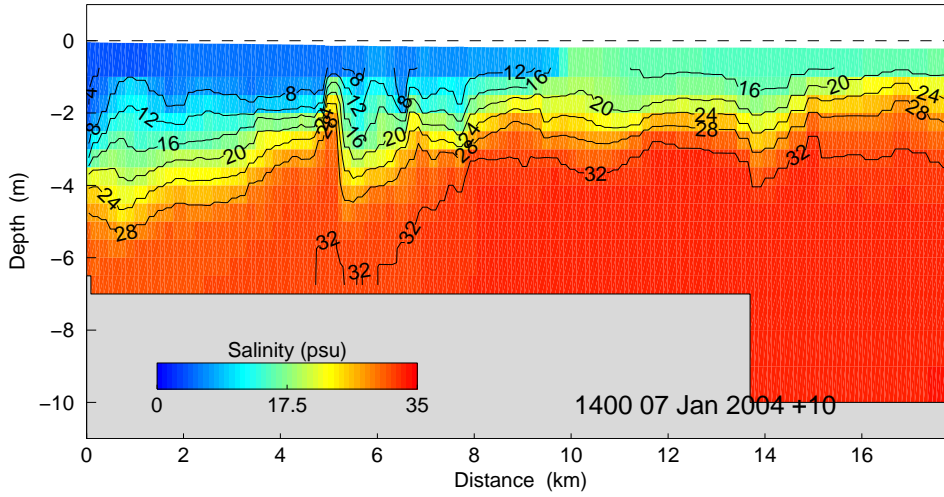


Figure 7.1.13 (a) : Salinity section using real bathymetry below Bowen Bridge, 5m above Bowen Bridge with idealised 7m channel

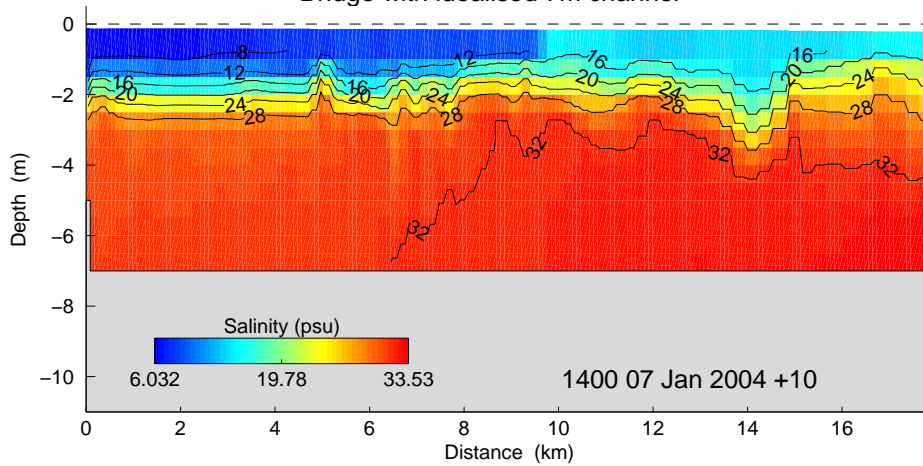
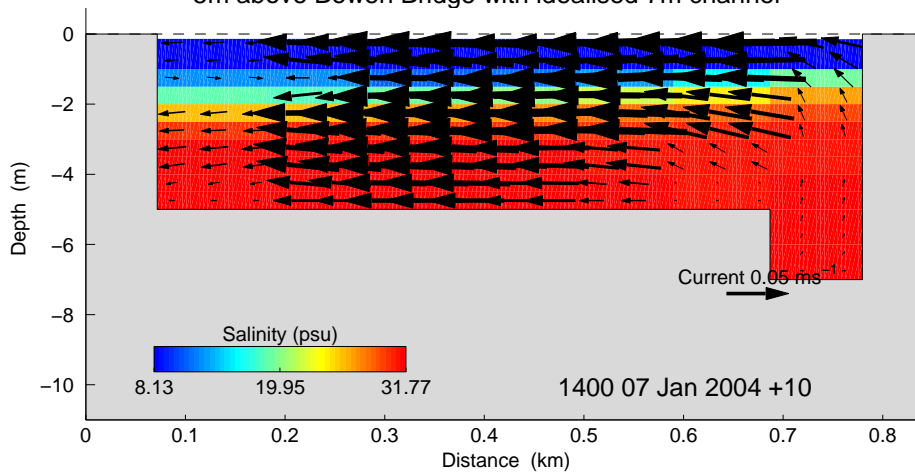


Figure 7.1.13 (b) : Salinity and velocity cross section using real bathymetry below Bowen Bridge, 5m above Bowen Bridge with idealised 7m channel



7.2 Residual Flow

Velocity was averaged over the neap-spring cycle (14 day means) in order to diagnose the residual circulation in the estuary. Surface and bottom velocities are displayed in Figure 7.2.1 (a) and (b) respectively. These Figures show that mean flow is down-estuary in the surface layer with magnitudes less than 0.2 ms^{-1} and up-estuary in the bottom layer with magnitudes less than 0.05 ms^{-1} . This is consistent with circulation in a salt wedge estuary, where the salt wedge propagates upstream due to baroclinic pressure forcing in the lower layers and returns downstream in the surface layer, augmented by the barotropically forced river discharge. The surface flow appears to favour the eastern bank of the river in the lower estuary, consistent with previous studies. Surface mean flow is into Ralphs Bay, while bottom mean flow is generally out of the Bay. A cyclonic gyre is observed at the bottom in the vicinity of Howrah. These flow patterns reflect the distribution passive tracers are expected to follow in the long term.

Residual currents at the surface and bottom were also computed over three day periods on both spring and neap tides (Figures 7.2.2 and 7.2.4 respectively), including a zoomed section of Elwick Bay (the focus site of the process study) in Figures 7.2.3 and 7.2.5. These 3 day means provide an indication of the variability of the mean flow during spring and neap conditions as a result of tidally rectified currents. The spring tide mean flow is similar to the long term mean with a more pronounced gyre occupying the channel off Howrah / Tranmere (Figure 7.2.2). The flow through Elwick Bay is downstream in the surface layer and upstream in the bottom layer throughout the Bay. A small anticyclonic gyre is evident at the north-eastern corner of the Bay (eastern shore). Surface currents are largest on the outer bank of bends at the surface, and in the main channel at the bottom, although bottom currents in the middle of the Bay are also quite large.

The neap tide case (Figure 7.2.4) again shows downriver flow at the surface and upriver flow at the bottom, however the gyre near Howrah at the bottom is absent under these conditions and appears at the surface. Outflow from Ralphs Bay in the bottom is also stronger during the neap phase. The spatial distribution and magnitudes of flow in Elwick Bay are similar to the spring phase, although a downstream flow is observed in the bottom on the north-western side of the Bay.

Figure 7.2.1 : 14 day mean flow

a) Surface

(b) Bottom

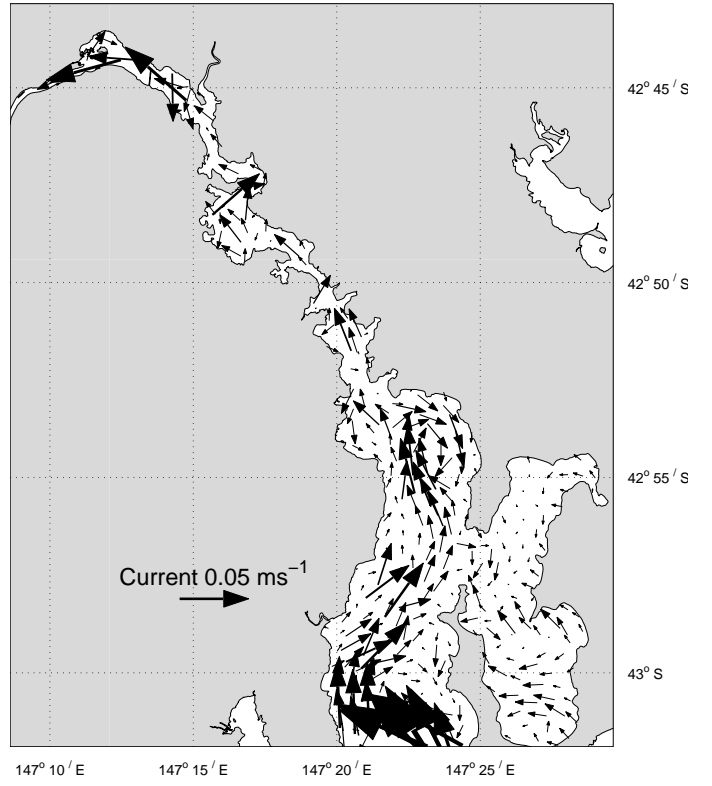
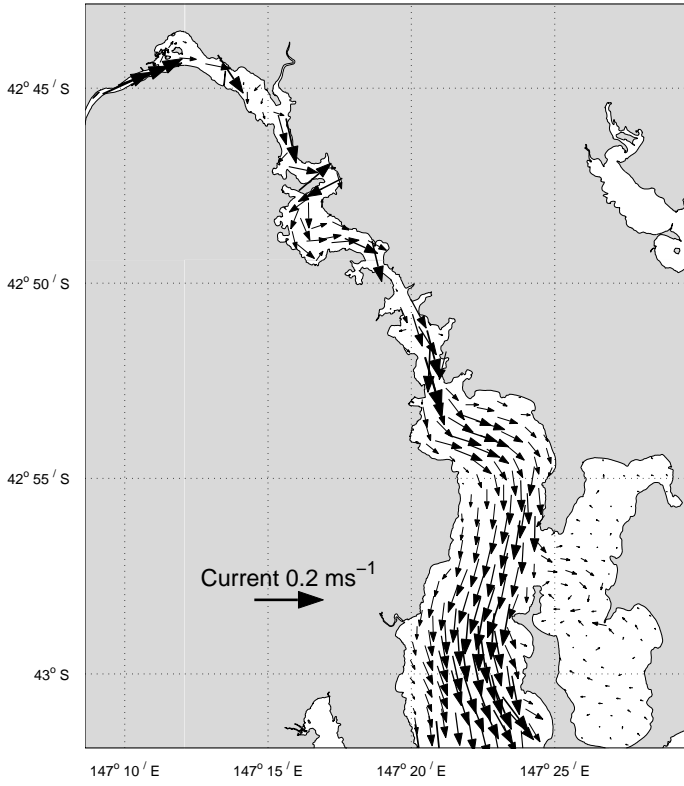


Figure 7.2.2 : 3 day mean flow : spring tide
 a) Surface (b) Bottom

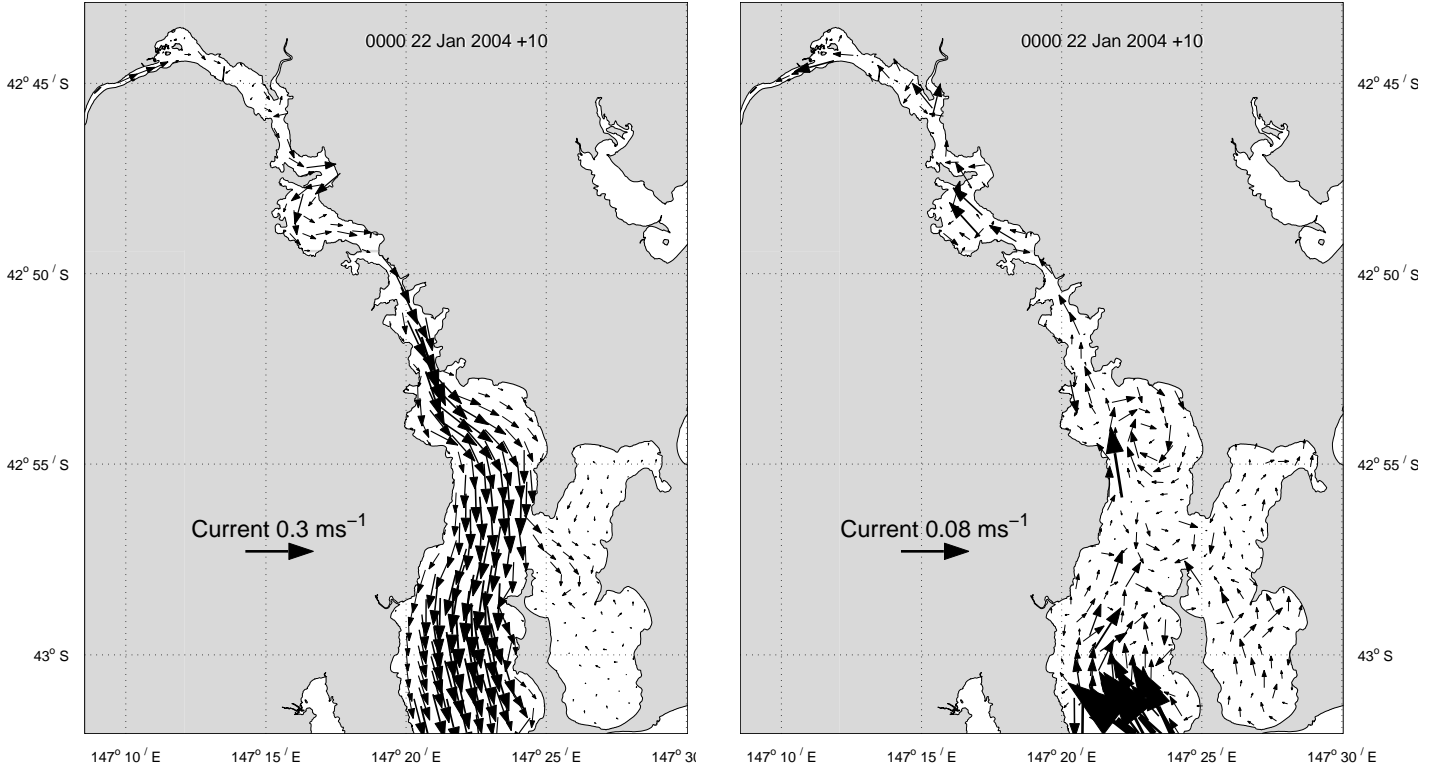


Figure 7.2.3 : Elwick Bay 3 day mean flow : spring tide
 a) Surface (b) Bottom

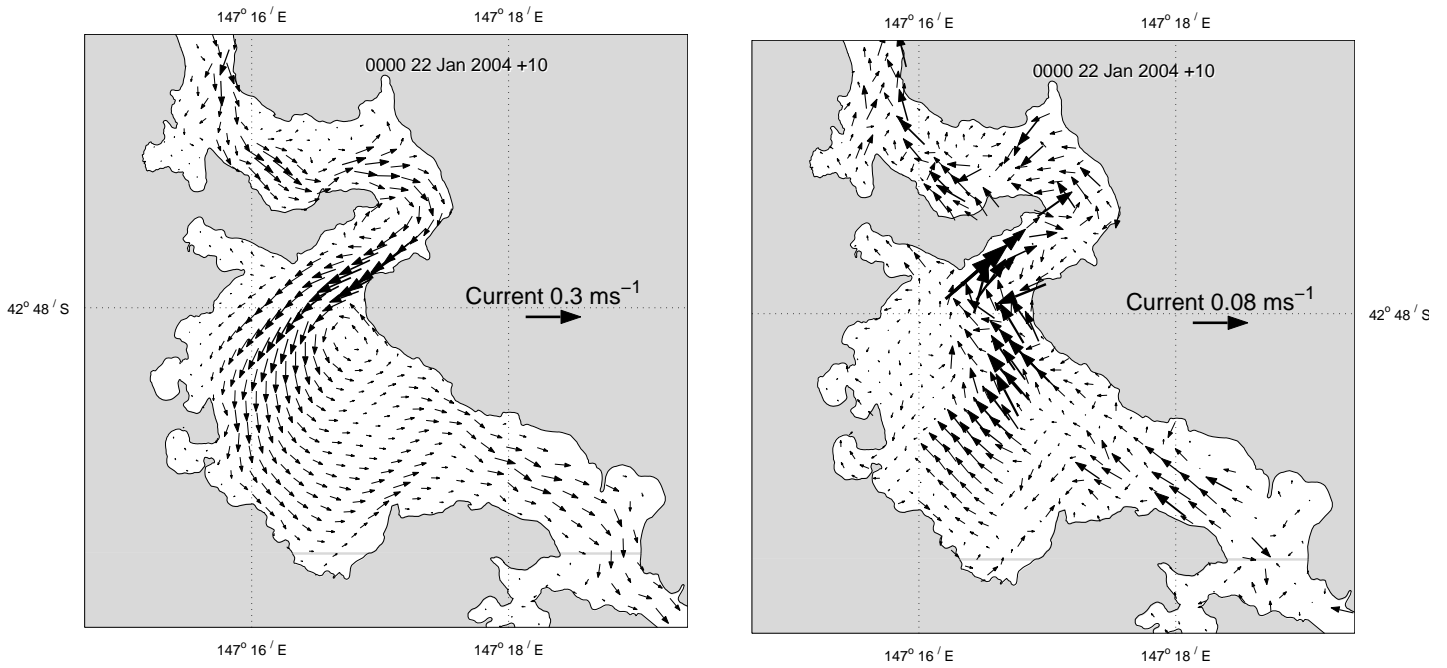


Figure 7.2.4 : 3 day mean flow : neap tide

a) Surface

(b) Bottom

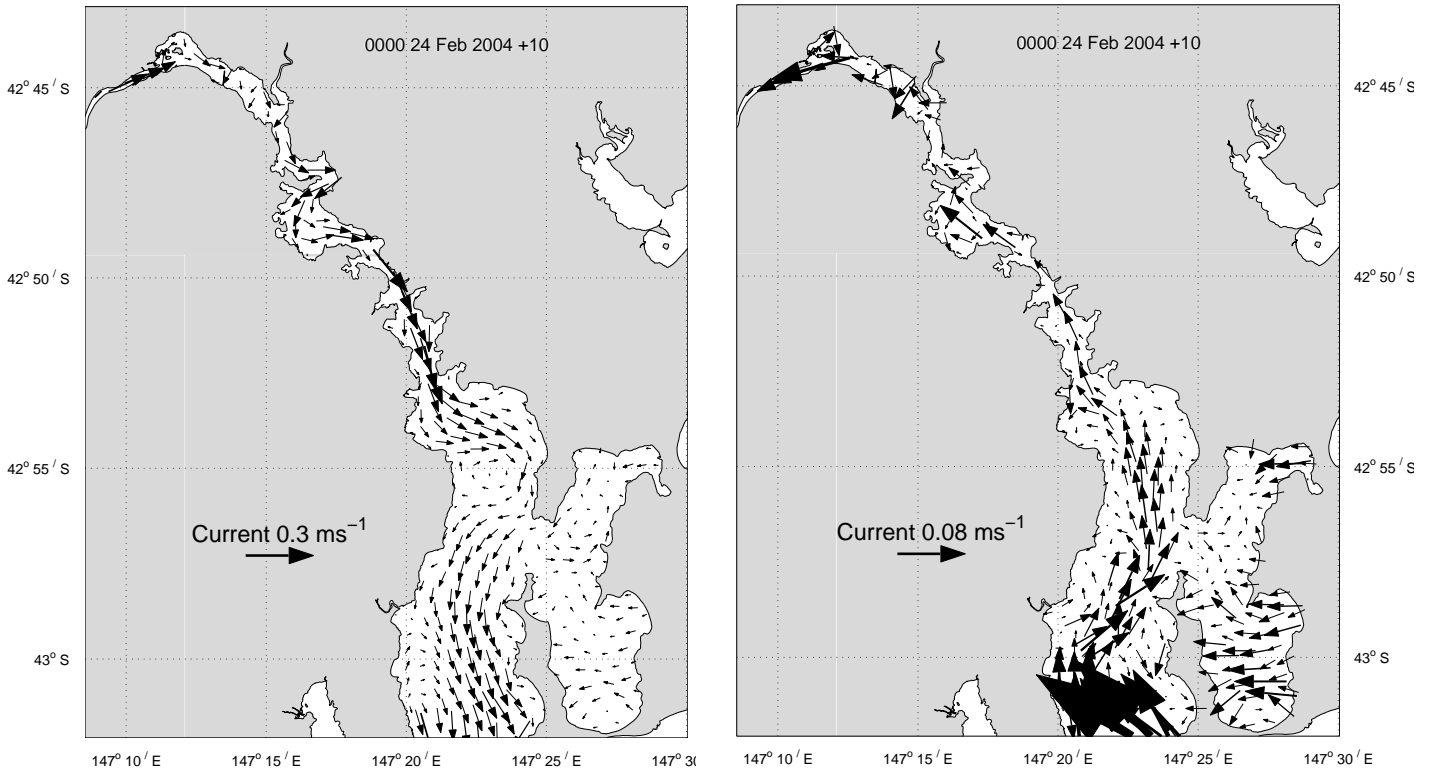
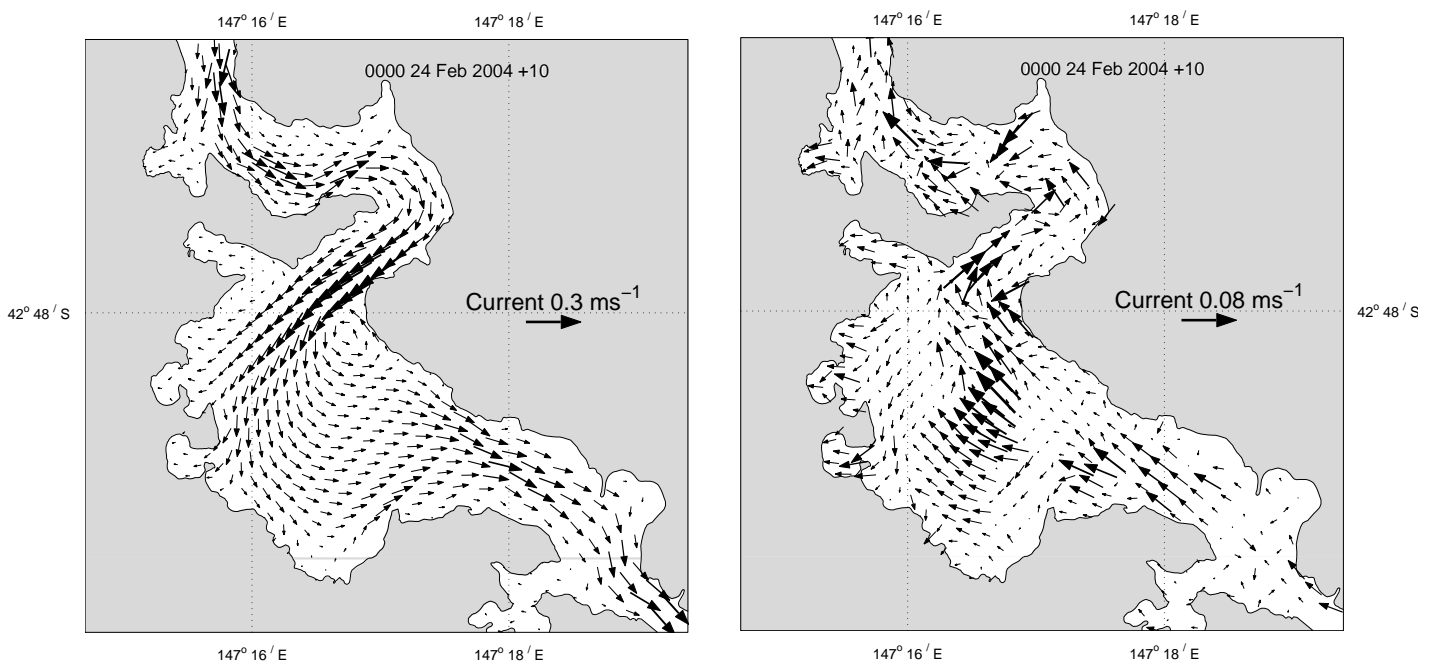


Figure 7.2.5 : Elwick Bay 3 day mean flow : neap tide

a) Surface

(b) Bottom



7.3 Momentum Balance

The model is capable of diagnosing the contribution from each term in the momentum balance to the change in velocity. This is in the form of a velocity tendency in ms^{-1} for each term in the momentum balance; i.e. momentum advection, horizontal diffusion (mixing), Coriolis (rotation), vertical diffusion (vertical mixing), barotropic pressure gradient forces (sea level gradients) and baroclinic pressure gradient forces (density gradients). Generally near the surface vertical diffusion represents the contribution due to the wind, which acts to accelerate the flow. Near the bottom vertical diffusion represents bottom drag which acts to retard the flow. The sum of all tendencies is equal to the total change in velocity over one time step (i.e. the acceleration). Note that the sum of tendencies is *not* equal to the actual velocity at any particular time, and must be added to the velocity at the previous time-step in order to obtain this actual velocity. Under steady state conditions the total tendency is zero and all momentum tendencies must balance. For non-steady motion one or several tendencies may dominate resulting in non-zero total tendency and acceleration of flow. Momentum tendencies are useful in evaluating the relative contributions of each forcing mechanism and diagnosing the dominant forcing mechanisms that drive motion in the domain.

The local momentum balance varies markedly in time and space throughout the domain depending on wind strength and direction, river flow and the phase of the diurnal tide and neap-spring tidal cycle. A snapshot at mooring site 3 (Elwick Bay) is presented in Figure 7.3.1 near the bottom (6.25 m) for the first 5 days of February 2004. During this time river flow varies from $\sim 130 - 180 \text{ m}^3\text{s}^{-1}$ and the tide was passing through a spring phase with minimum tidal range of 1.1m. Wind was generally low, coming from the south-western quadrant with speeds of around 4 ms^{-1} . The along-channel direction corresponds to the u_1 velocity and cross-channel direction by the u_2 velocity. Figure 7.4.1 shows that generally the barotropic pressure gradient (i.e. tidal forcing, black line in Figure 7.4.1) and baroclinic pressure gradient (density forcing, pink line) dominates the solutions. The horizontal diffusion is also frequently large, and in phase with the tidal forcing. This is consistent with the sensitivity analysis, where the magnitude of horizontal diffusion coefficients impacted on the calibration. This time series is taken near the bottom, hence vertical diffusion represents deceleration on the flow due to bottom friction, which is generally negligible in comparison to other forcing. The Coriolis force (aqua line) is apparent only in the cross channel direction, consistent with flow predominantly in the along-estuary direction. The cross-channel direction also exhibits significant contribution from non-linear advection, consistent with the importance of momentum advection in generating cross-river secondary circulations. The momentum balance varies spatially and temporally throughout the domain, as mentioned above, therefore while tendency snapshots are useful for diagnosing the momentum balance for a particular place and time, the characterisation of the system as a whole is difficult to capture. A mean momentum balance is of more use to infer the net motion in the domain.

The spatial distributions for the mean tendencies over the simulation are shown in Figures 7.3.2 – 7.3.7. These Figures show the largest tendencies are due to the baroclinic pressure, vertical diffusion and Coriolis. The barotropic pressure tendency is weakly directed down-estuary (Figure 7.3.6). The tides are the major contributor to the barotropic tendency, and these average out to result in net flow due to river forcing and tidally rectified currents only. In the model the Derwent river inflow at the New Norfolk boundary is forced using a vertical velocity profile rather than a pressure gradient, hence the barotropic tendency reflects only a component of this forcing. The Coriolis force tends to drive flow eastwards in the bottom layer and westwards in the surface layer (Figure 7.3.5). This is consistent with the down-estuary surface flow and up-estuary bottom flow both deflected to the left in the southern hemisphere. The baroclinic pressure tendency generally drives flow up-estuary in the bottom layers, consistent with the salt-wedge circulation (Figures 7.3.7, 7.3.8). The non linear components (advection, Figure 7.3.2 and horizontal diffusion, Figure 7.3.3) show no coherent pattern and are small except for isolated locations in the estuary. These

non-linear tendencies become locally important in perturbing the stratified structure. This is investigated further below.

This analysis indicates that locally motion in the domain is driven predominantly by tide and density effects, as expected for a micro-tidal salt wedge estuary. The mean flow is a balance between density forcing and Coriolis. The salt wedge is driven up-estuary in the bottom layers by density forcing, and entrains water into the surface layer where it returns down-estuary. These flows are balanced by the Coriolis force. Bottom friction acts to retard the flow near the bottom, and at the surface the wind contributes a mean westerly component. The non-linear components may be locally important.

Snapshots of the spatial distribution of the tendencies at high water, low water and maximum ebb tide are displayed in Figures 7.3.9 to 7.3.14. These figures show that the dominant forcing is due to the barotropic gradient, directed down-estuary and maximum on the ebb tide. Due to mixed diurnal character of the tide the ebb is stronger and shorter than the flood, since during the flood the semi-diurnal tide opposes the flood to some extent. The advective tendency is the next largest contributor to the momentum balance and is maximum at the surface on the ebb tide. The baroclinic contribution is generally maximum at the bottom, having an up-estuary maximum at high and low tide when mixing is minimum. This component is observed to produce localized downstream flow during the maximum ebb. The horizontal diffusion and Coriolis components are maximum at various locations in the water column on the ebb tide when tidal currents are maximum. Vertical diffusion tendency is maximum at surface or bottom, generally during times of maximum flow.

The flow driven by the advective tendency on the ebb tide is highly divergent, as is the barotropic pressure tendency to a lesser degree. This results in local areas of upwelling and downwelling. This is consistent with secondary circulations resulting from barotropic pressure and momentum exchange from turbulence stress forces outlined in Section 7.1, which were hypothesised to be responsible for perturbing the density structure and creating the observed wave-like features noted in Section 7.1.

Figure 7.3.1 : Momentum balance at mooring 3 (Elwick Bay)

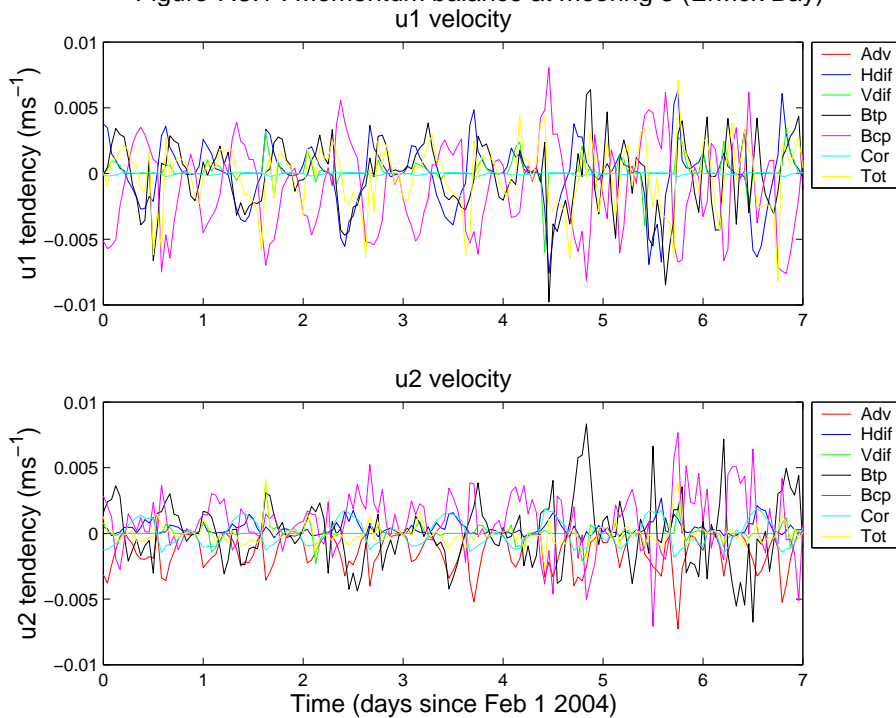


Figure 7.3.2 : Mean advective tendency
(a) : Surface (b) Bottom

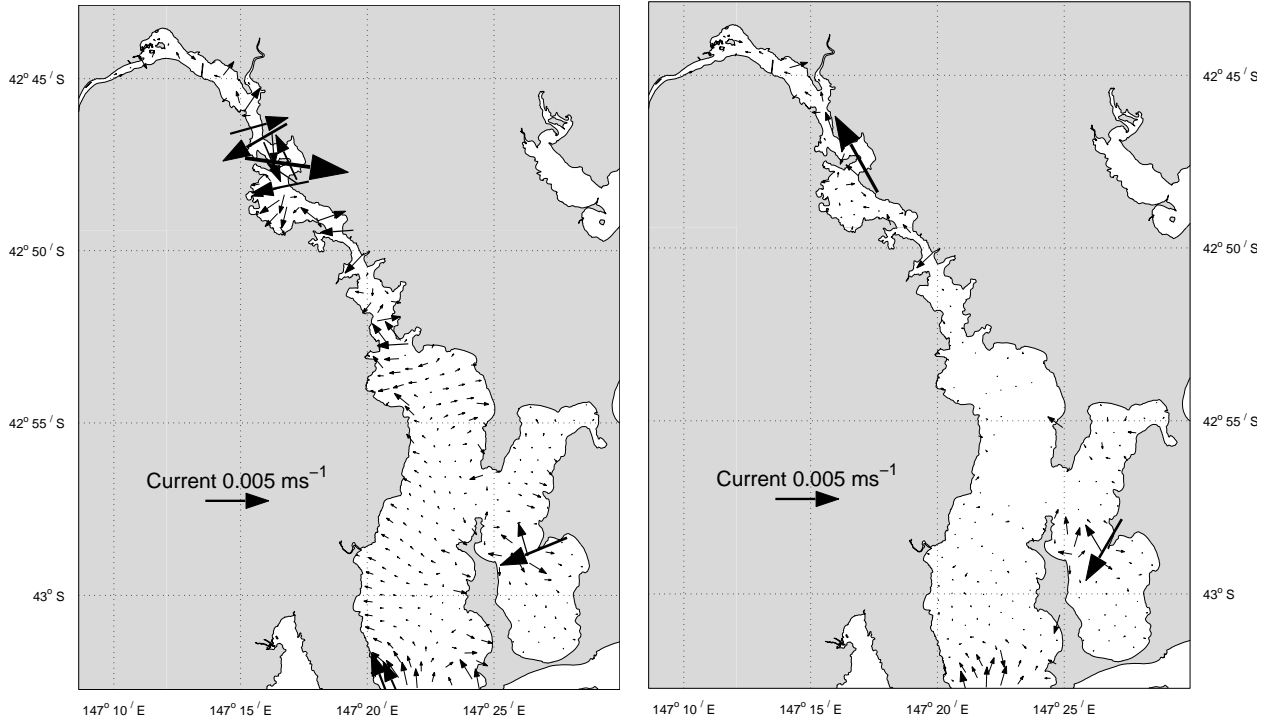


Figure 7.3.3 : Mean horizontal diffusive tendency
(a) : Surface (b) Bottom

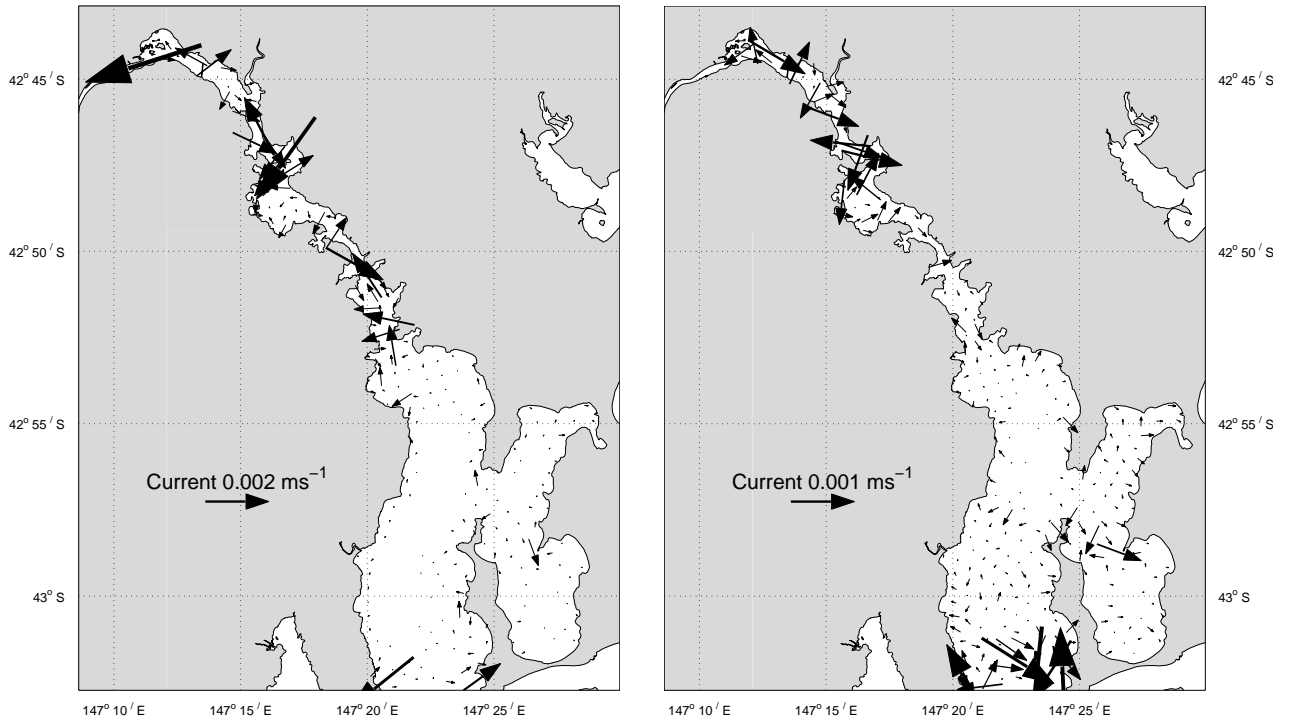


Figure 7.3.4 : Mean vertical diffusive tendency
 (a) : Surface (b) Bottom

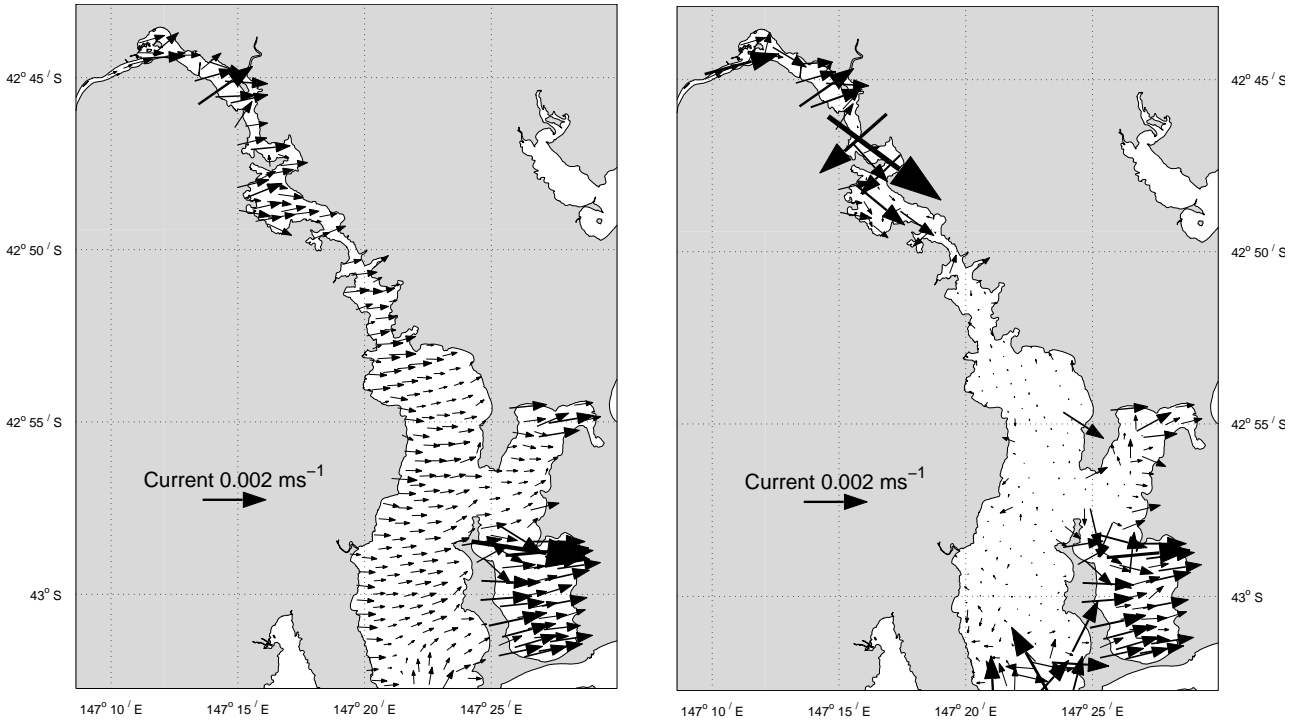


Figure 7.3.5 : Mean Coriolis tendency
 (a) : Surface (b) Bottom

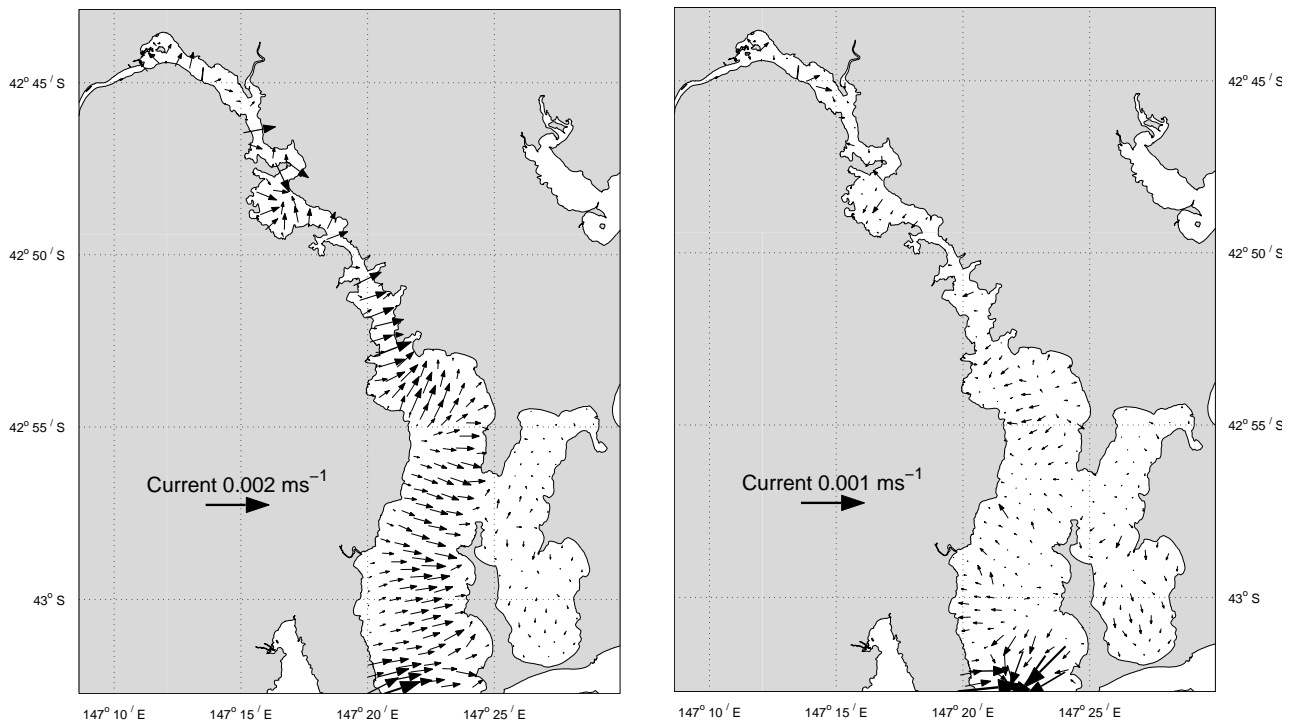


Figure 7.3.6 : Mean barotropic pressure tendency
 (a) : Surface (b) Bottom

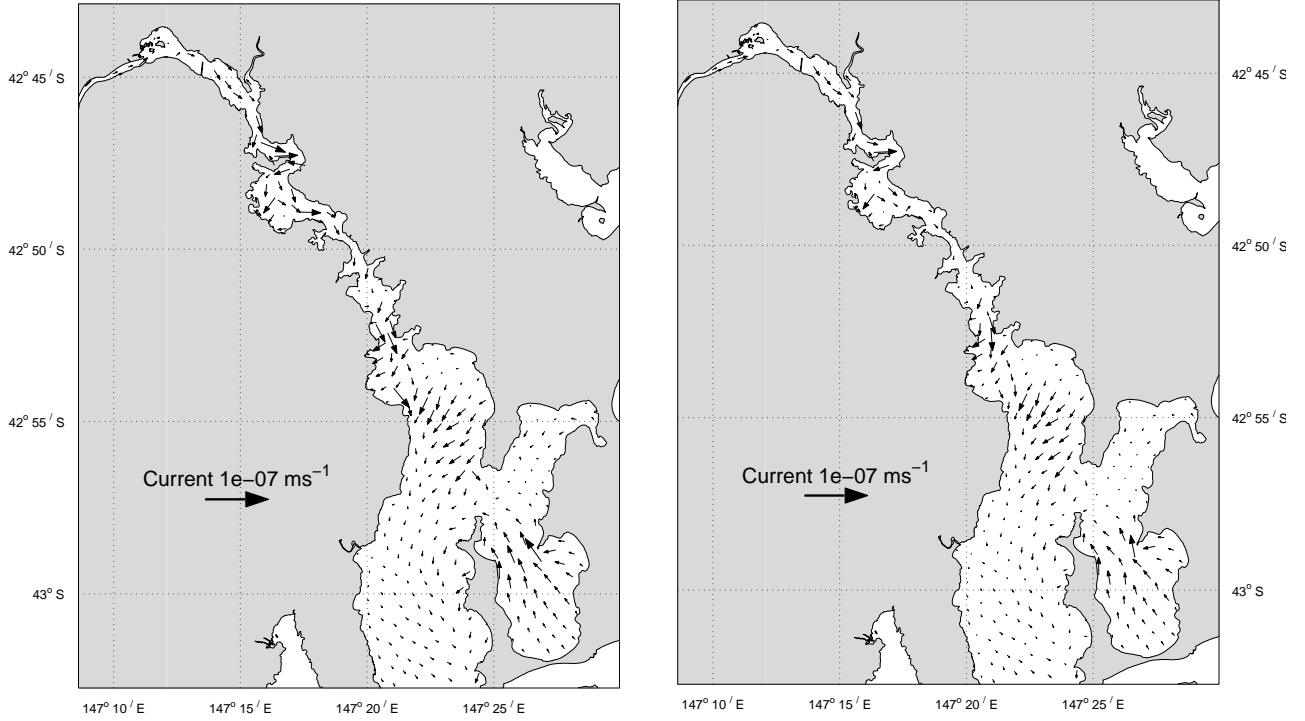


Figure 7.3.7 : Mean baroclinic pressure tendency
 (a) : Surface (b) Bottom

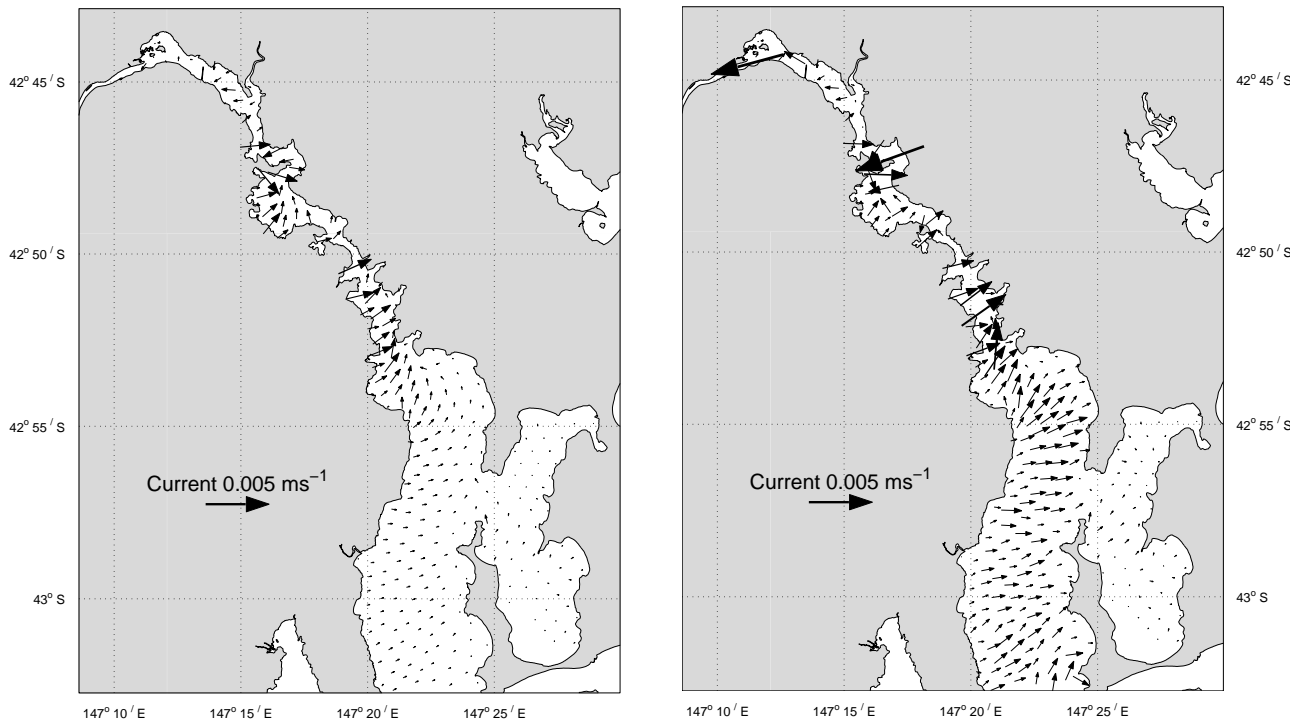


Figure 7.3.8 : Detail of mean bottom baroclinic pressure tendency

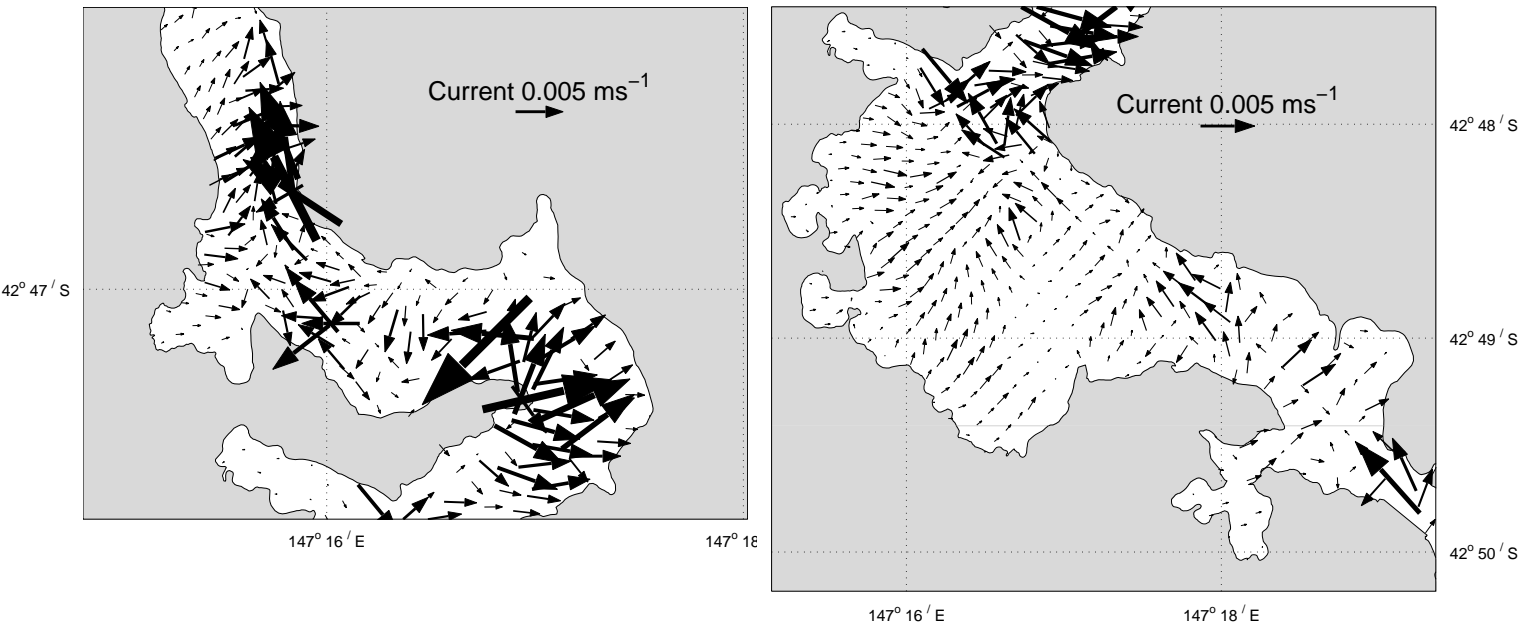


Figure 7.3.9 : Advective tendency (surface)
(b) Maximum ebb

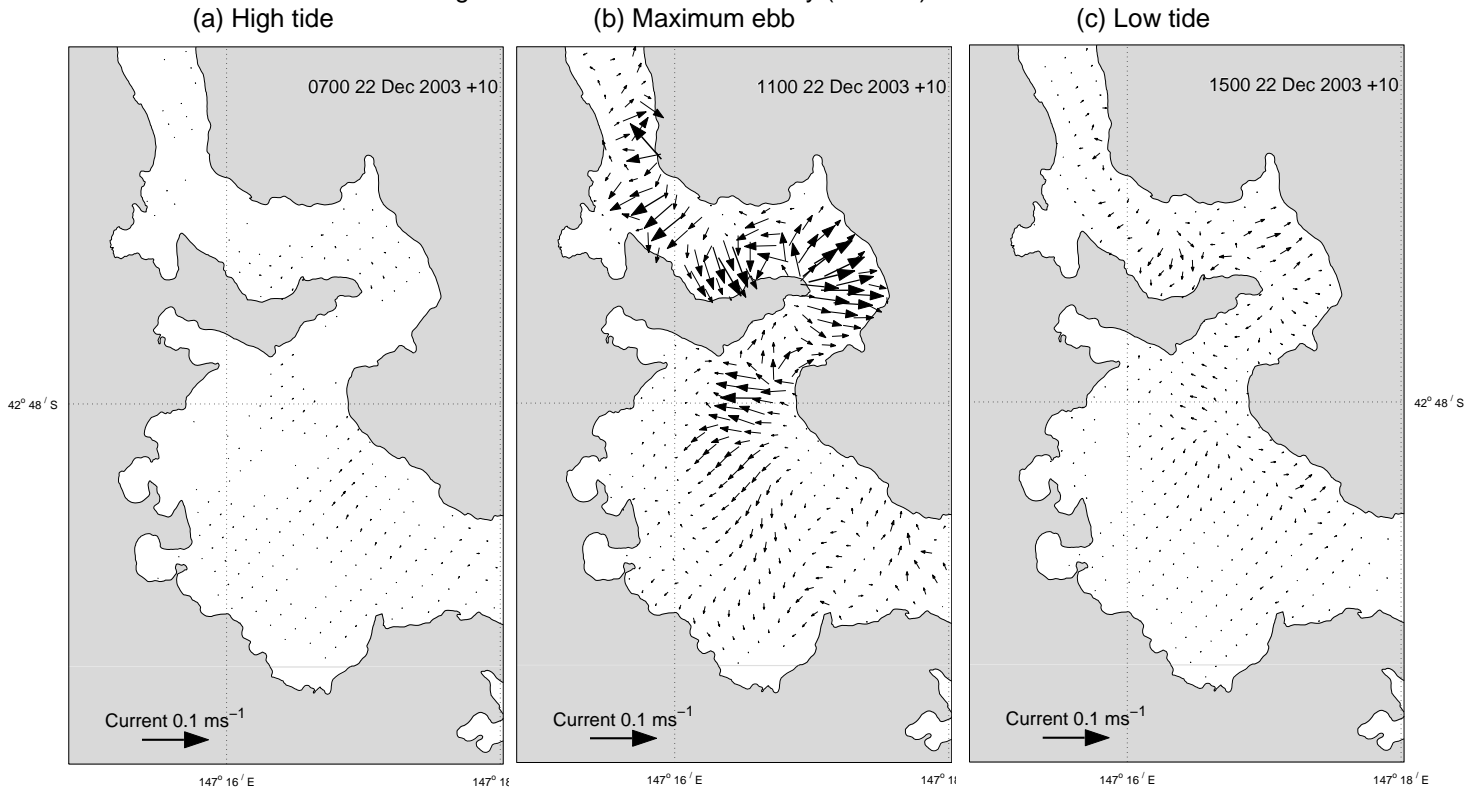


Figure 7.3.10 : Horizontal diffusive tendency (at 2.25m)
(b) Maximum ebb

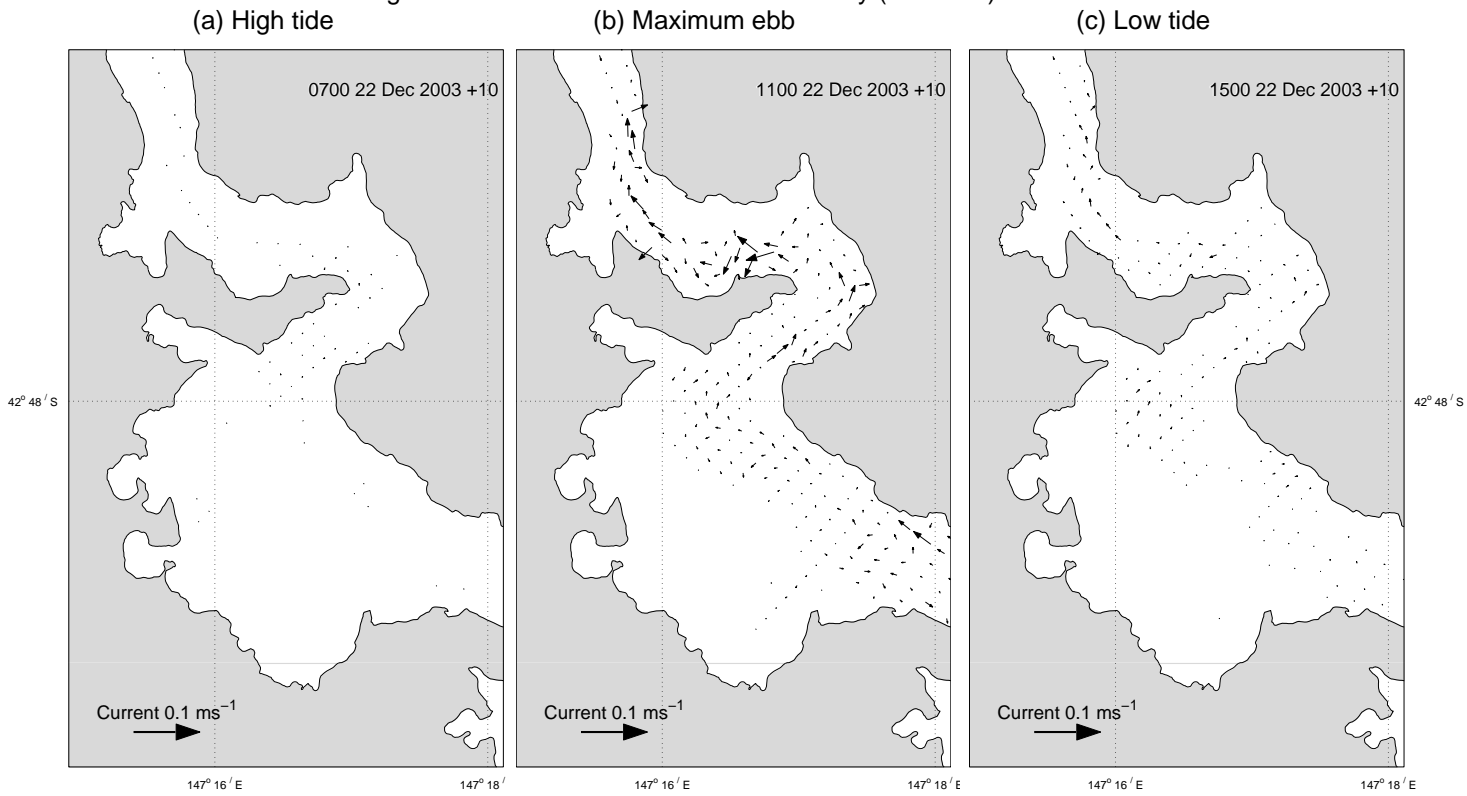


Figure 7.3.11 : Vertical diffusive tendency (bottom)

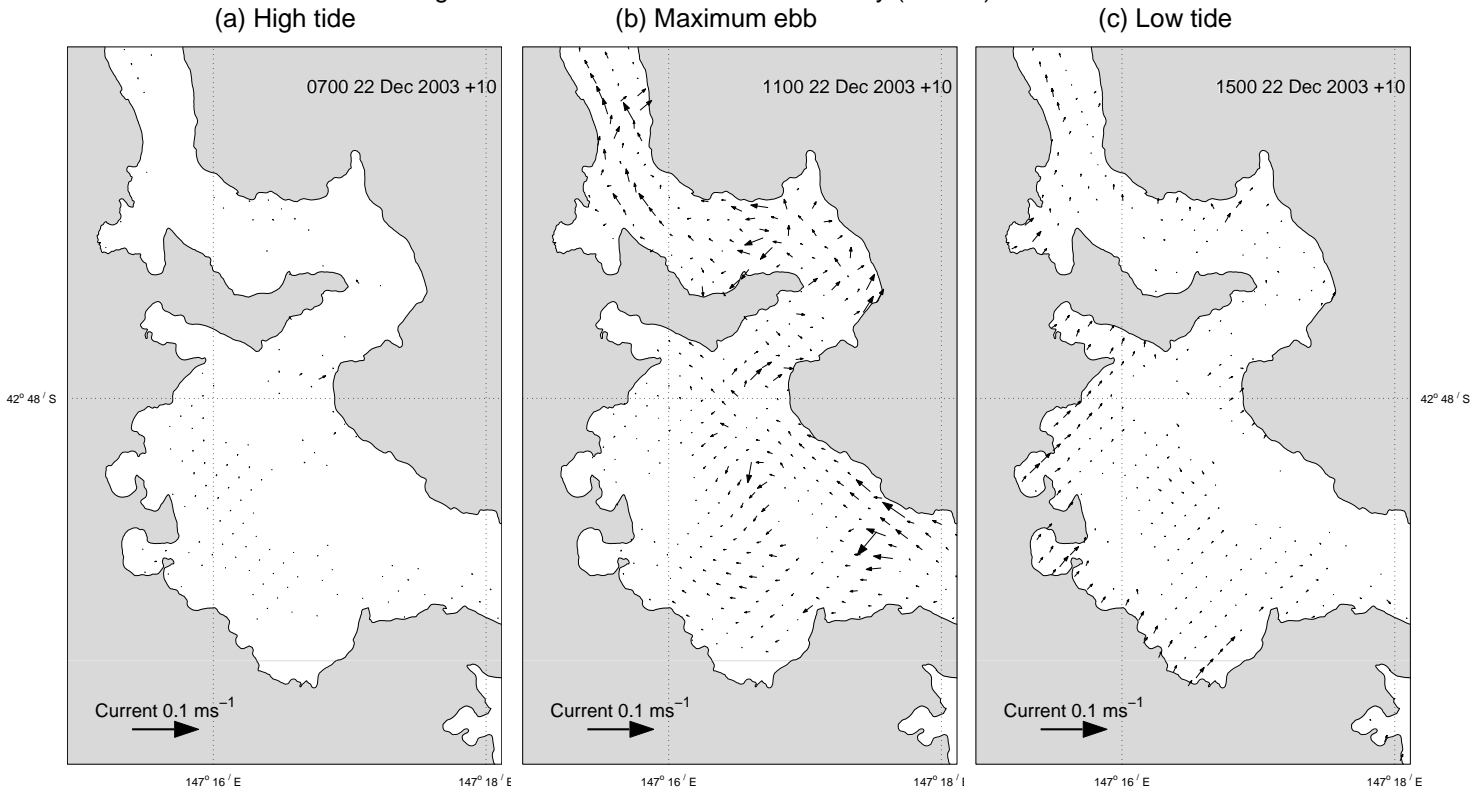


Figure 7.3.12 : Coriolis tendency (surface)

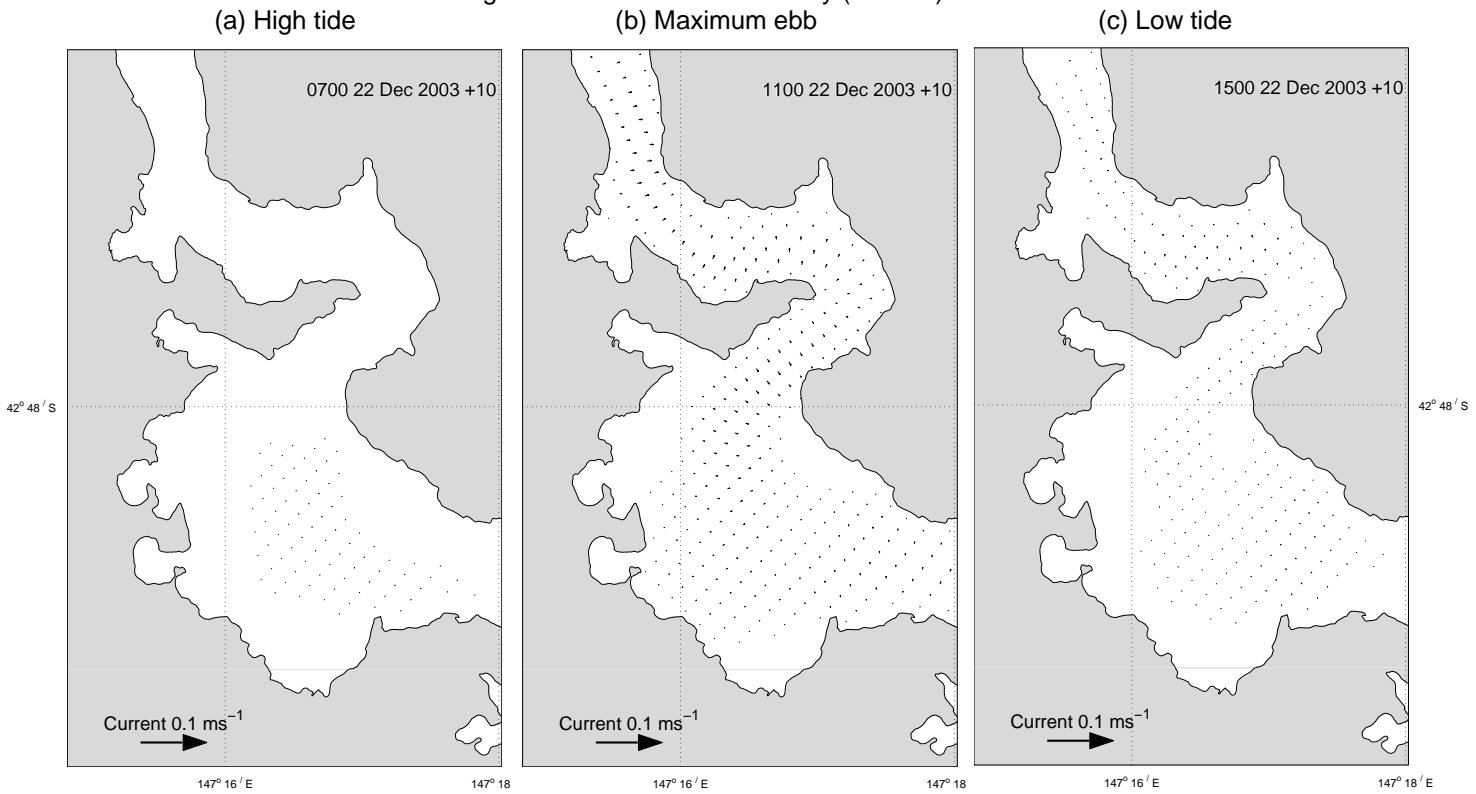


Figure 7.3.13 : Barotropic pressure tendency (surface)

(a) High tide

(b) Maximum ebb

(c) Low tide

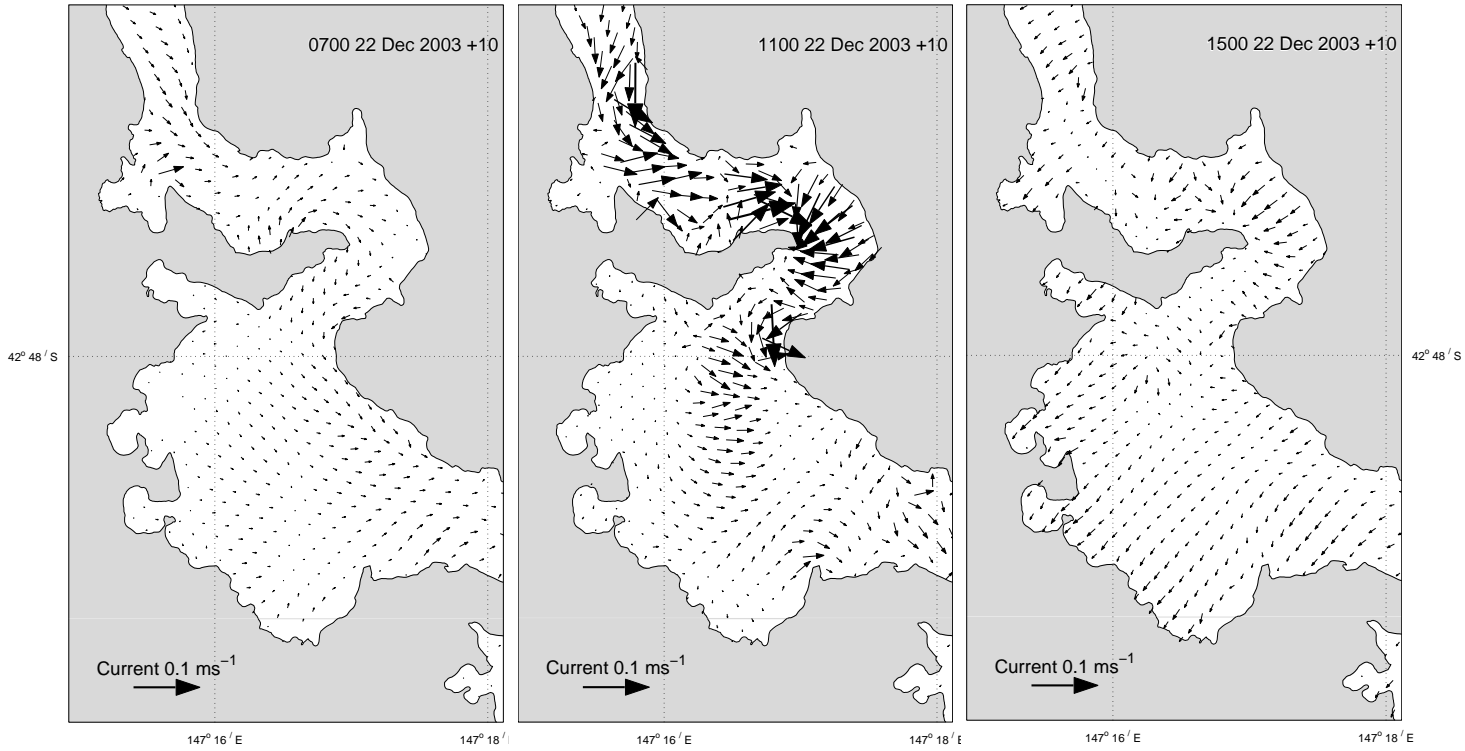
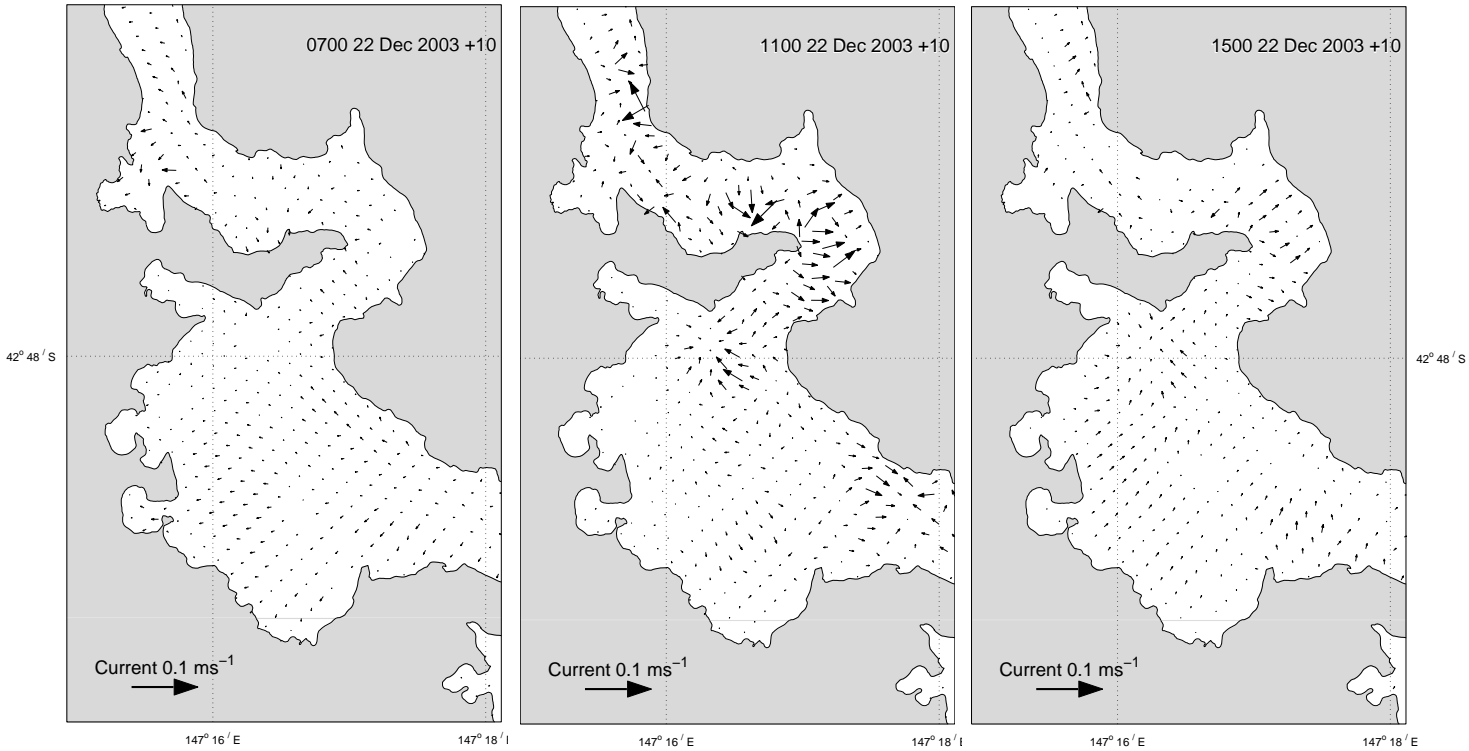


Figure 7.3.14 : Baroclinic pressure tendency (bottom)

(a) High tide

(b) Maximum ebb

(c) Low tide



7.4 Flushing Times

Passive tracers were used to obtain an estimate of the flushing characteristics of the estuary. A passive tracer was initialized in a sub-region of the estuary with a concentration of 1 and zero elsewhere, and the total mass in this sub-region was calculated throughout the simulation. Full forcing was applied to the domain (i.e. wind, tide, low frequency sea level and temperature / salinity effects) and the tracer distribution was simulated for a fixed period encompassing the expected flushing time. The e-folding time for flushing this sub-region is encountered when the total mass was reduced to $1/e$ (~38%) of the initial mass.

Flushing times were calculated for the dates 16 Jan and 5 Feb when mean flow was 56 and $78 \text{ m}^3\text{s}^{-1}$ respectively. River discharge remained constant during the lower mean flow period (e.g. ~ day 30 in Figure 5.4.1) whereas the higher mean flow period encompassed a period of rapidly fluctuating high flow (~ day 50 in Figure 5.4.1 with a maximum flow of $\sim 170 \text{ m}^3\text{s}^{-1}$). The simulation starts at low water for both the times. Flushing times were calculated for a variety of sections of and estuary and side bays, summarized in Table 7.4.1. The initial flushing region for each simulation, the tracer distribution at the flushing time and time series of the normalized total mass in the sub-regions are displayed in Figures 7.4.1 to 7.4.16. The time series plots include a fitted curve to the total mass decrease which provides a general trend of tracer decrease.

Flushing times for each region are summarized in Table 7.4.1, from which it is observed that flushing times vary markedly. Overall flushing characteristics for the Derwent can be characterized as good. The longest flushing time, not surprisingly, is for the whole estuary with a time of 11.1 days under flow conditions of $56 \text{ m}^3\text{s}^{-1}$. Maximum surface tracer concentration is found in Ralphs Bay at the flushing time, with significant concentrations (> 0.9 , i.e. 90% of the original concentration) for low flows. The fastest flushing time is found in New Town Bay, with a time of ~4 hours. Flushing times decrease for all regions with increasing river flow, and hence the flushing times for each region are not fixed but are expected to vary significantly under different forcing conditions of wind, tidal range and river flow. The flushing times presented below, however, provide a useful relative comparison of regions under flow conditions close to the median.

All the side bays have short flushing times of less than 1 day. Although the tracer mass is rapidly reduced in these bays due to removal of tracer from the bay, the tracer is simply moved to another location and thus remains present in the estuary for a much longer time. An example is New Town Bay under $78 \text{ m}^3\text{s}^{-1}$ flow where tracer is removed in ~4 hours (Fig 7.4.14) but is transported to the next bay downstream, Cornelian Bay (albeit with lower concentrations of ~0.1). Hence if this tracer were to represent a contaminant, the removal from one location can result in contamination in another. An exception appears to be Prince of Wales Bay (Figs 7.4.11 & 12), where the bulk of tracer appears to be confined to the Bay.

Table 7.4.1 : Flushing Characteristics

Run	Region	Date	Flushing (days)
1	Whole estuary	16 Jan	11.1
2	Whole estuary	5 Feb	9.3
3	Upper + middle	16 Jan	4.0
4	Upper + middle	5 Feb	3.4
5	Elwick Bay	16 Jan	0.78
6	Elwick Bay	5 Feb	0.64
7	Cornelian Bay	16 Jan	0.48
8	Cornelian Bay	5 Feb	0.38
9	Geilston Bay	16 Jan	0.55
10	Geilston Bay	5 Feb	0.32
11	Prince of Wales Bay	16 Jan	0.88
12	Prince of Wales Bay	5 Feb	0.68
13	New Town Bay	16 Jan	0.40
14	New Town Bay	5 Feb	0.17
15	Ralphs Bay	16 Jan	3.42
16	Ralphs Bay	5 Feb	2.14

Figure 7.4.1 : Flushing from 16 Jan 2004
Mean flow = $56 \text{ m}^3 \text{ s}^{-1}$, flushing time = 11.1 days

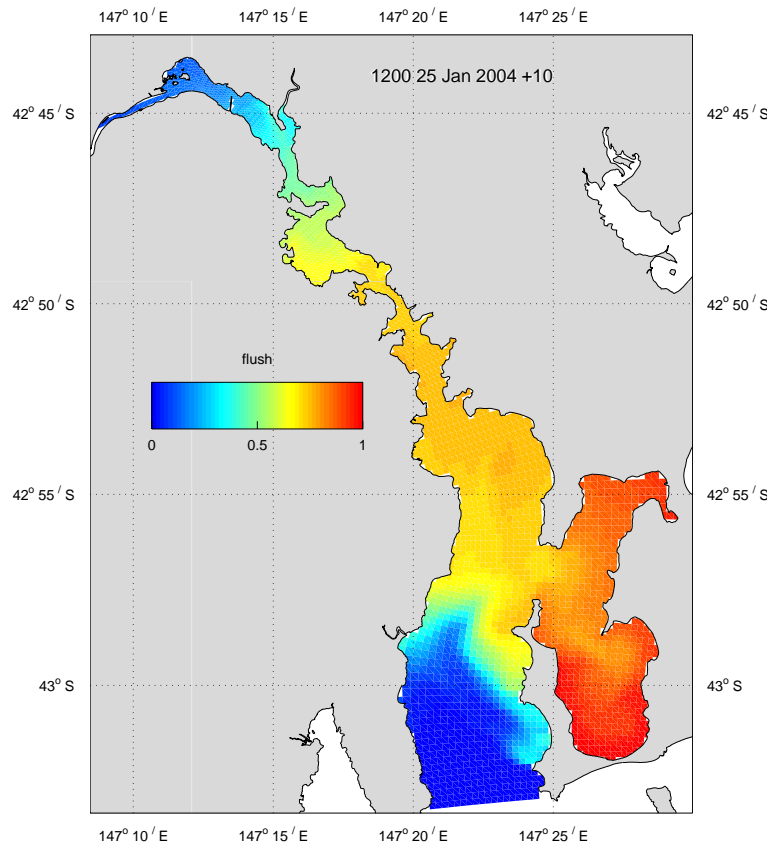
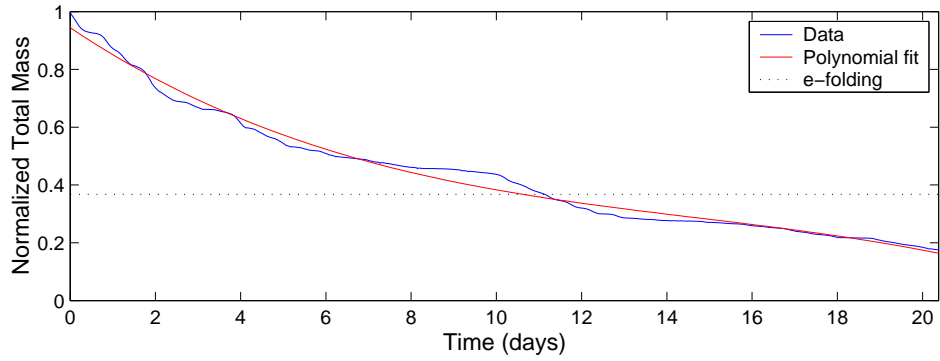


Figure 7.4.2 : Flushing from 5 Feb 2004
Mean flow = $78 \text{ m}^3 \text{ s}^{-1}$, flushing time = 9.3 days

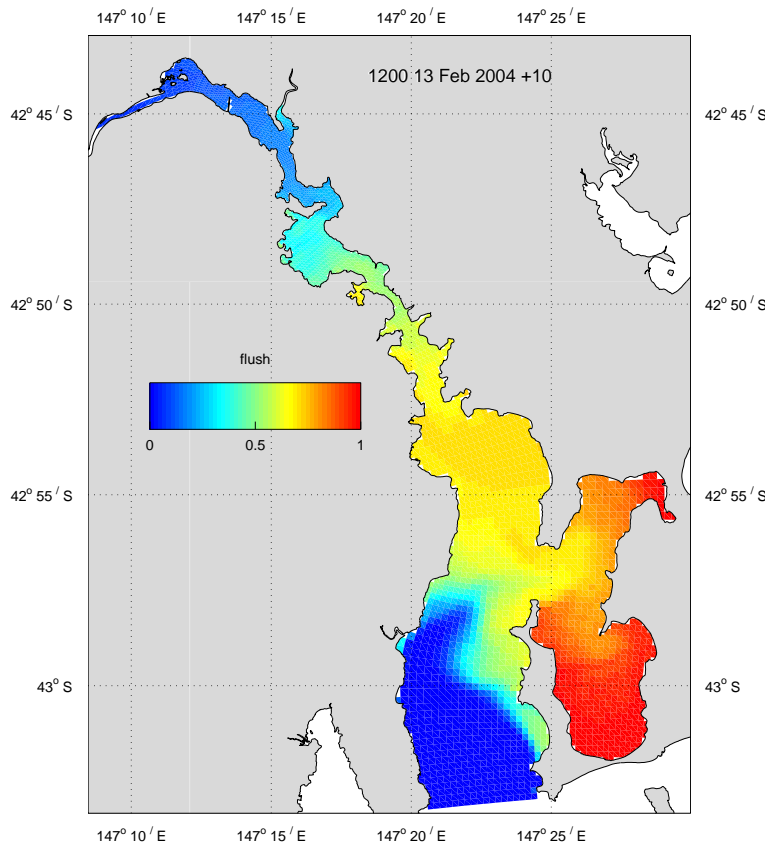
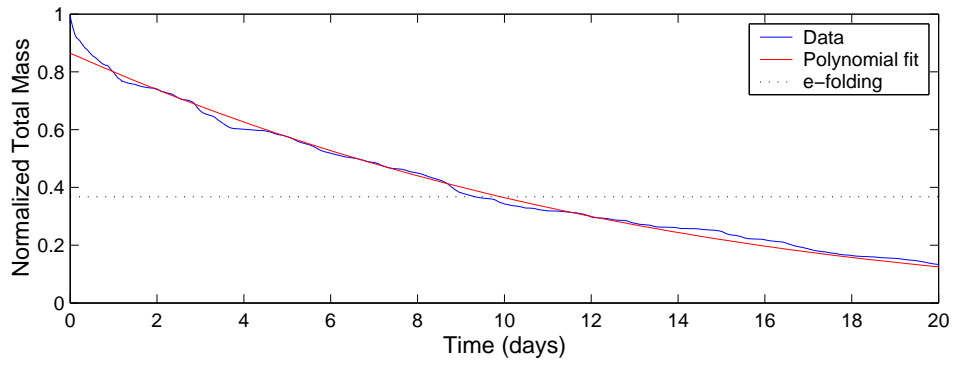
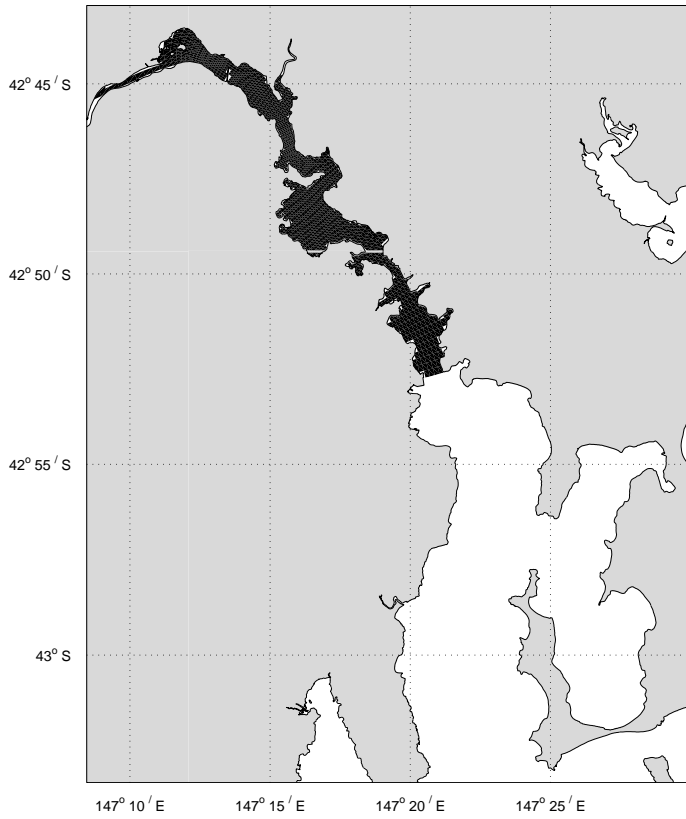
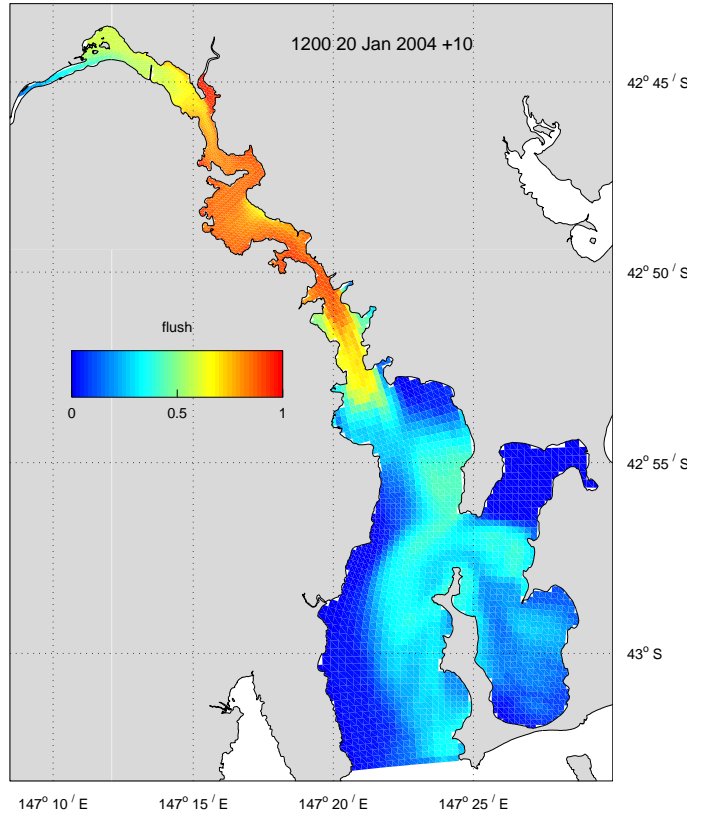


Figure 7.4.3 : Middle and upper estuary flushing from 16 Jan 2004
Mean flow = $56 \text{ m}^3 \text{ s}^{-1}$, flushing time = 4.0 days

(a) Flushing region in black



(b) Surface tracer distribution at 20 Jan



(c) Flushing characteristics

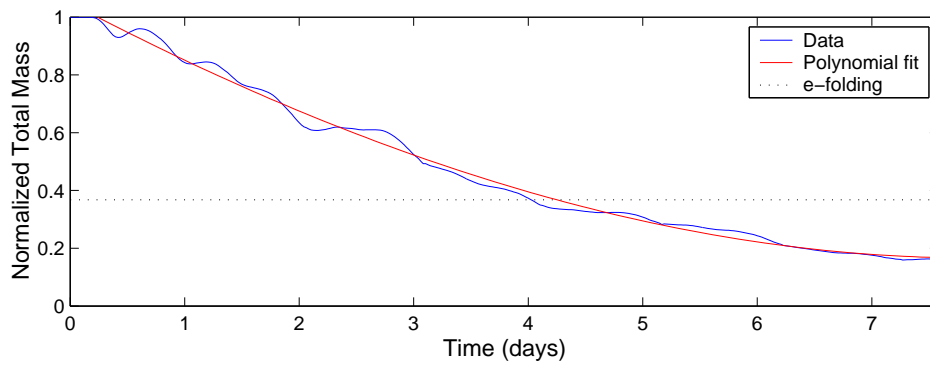
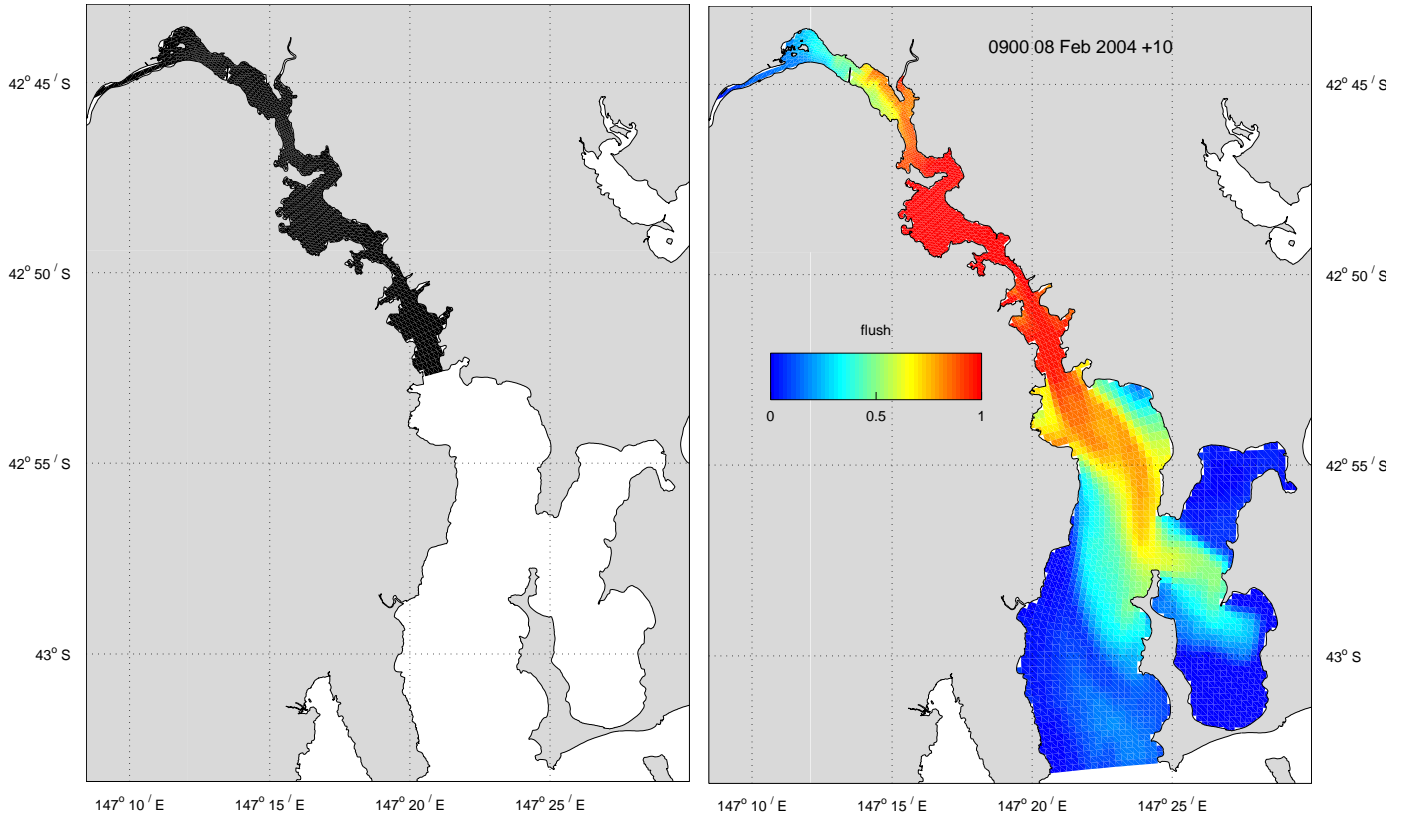


Figure 7.4.4 : Middle and upper estuary flushing from 5 Feb 2004
Mean flow = $78 \text{ m}^3 \text{ s}^{-1}$, flushing time = 3.4 days

(a) Flushing region in black

(b) Surface tracer distribution at 8 Feb



(c) Flushing characteristics

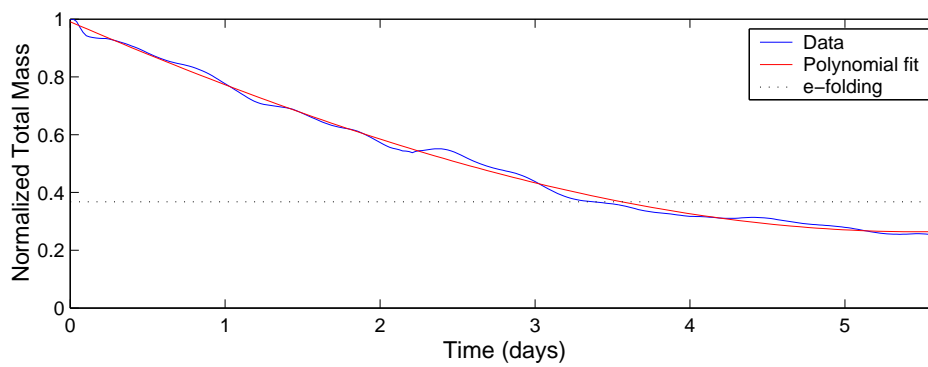
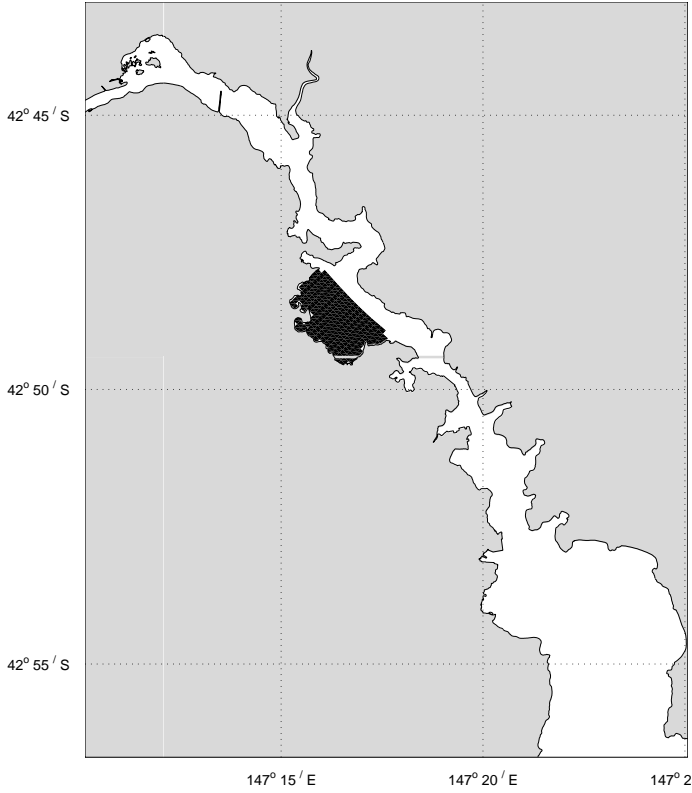
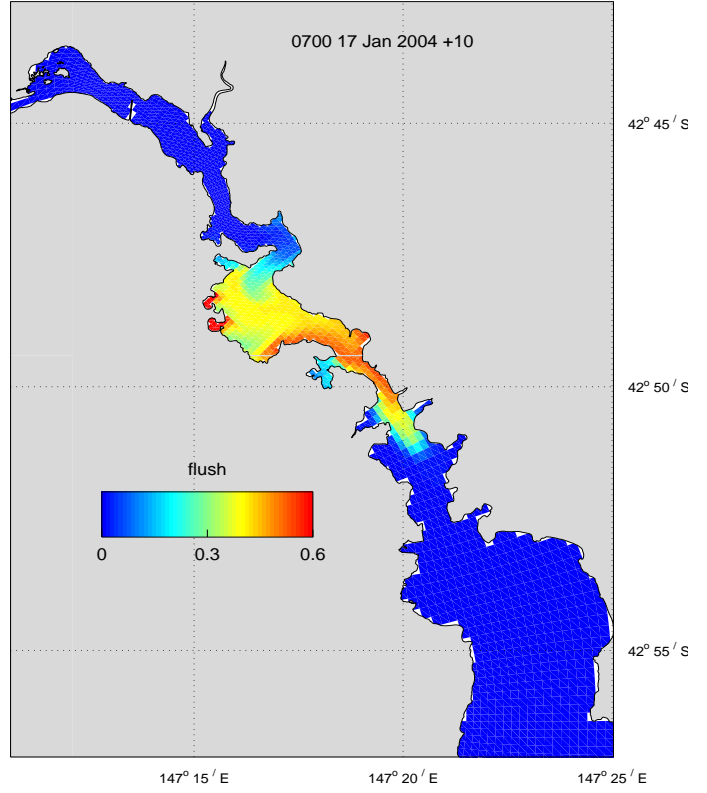


Figure 7.4.5 : Elwick Bay flushing from 16 Jan 2004
 Mean flow = $56 \text{ m}^3\text{s}^{-1}$, flushing time = 18.72 hours

(a) Flushing region in black



(b) Surface tracer distribution at 17 Jan



(c) Flushing characteristics

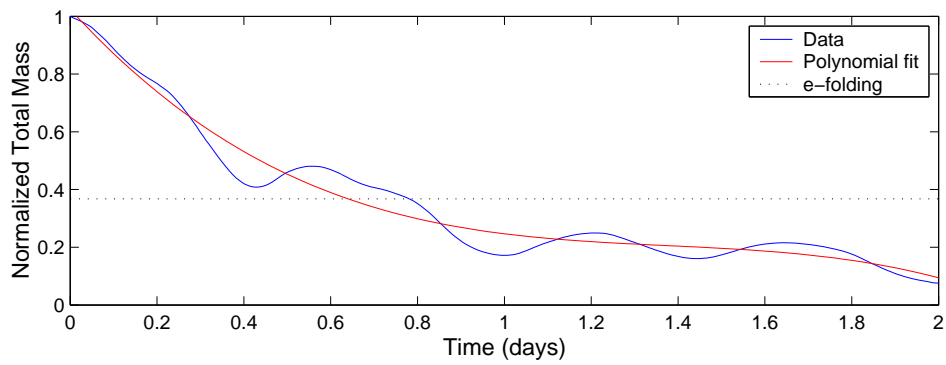
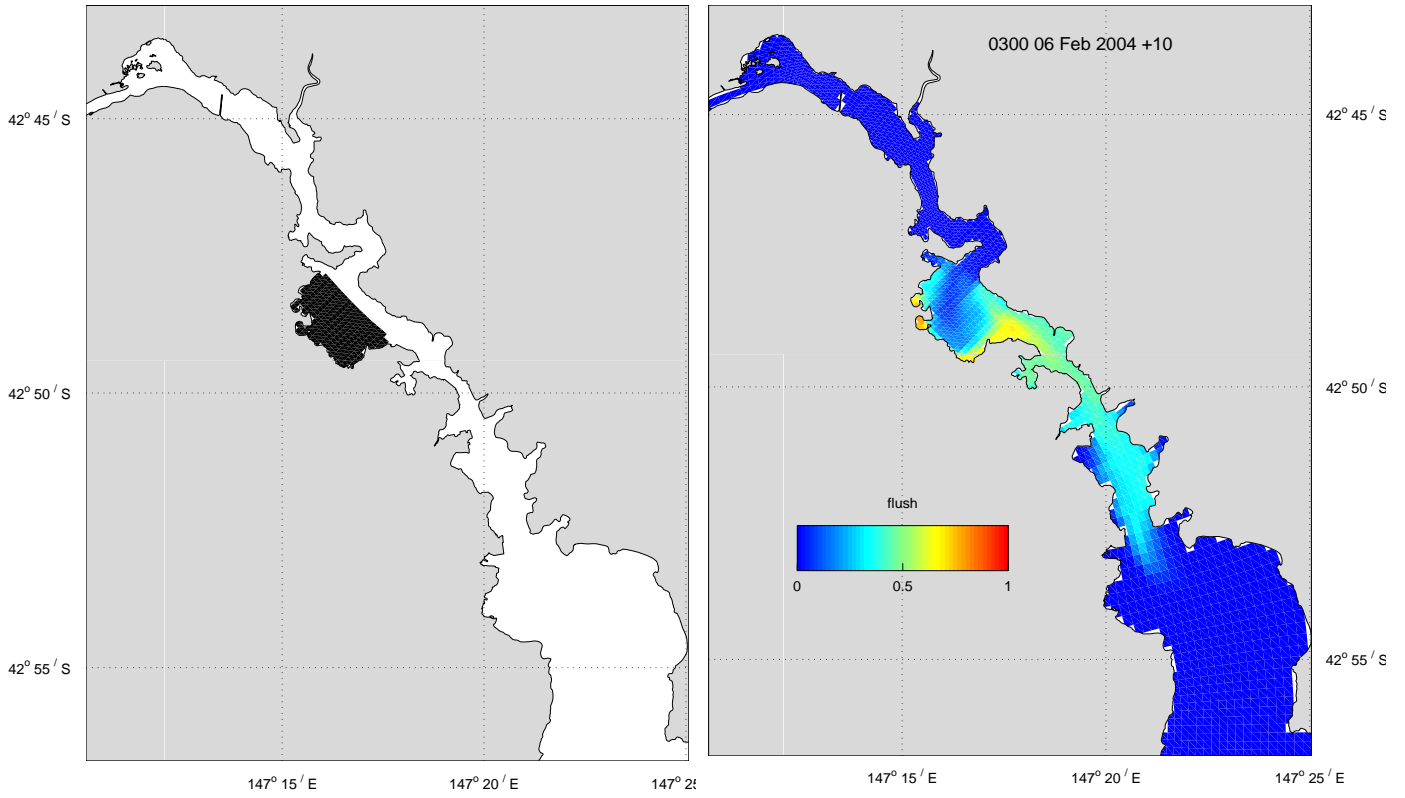


Figure 7.4.6 : Elwick Bay flushing from 5 Feb 2004
Mean flow = $78 \text{ m}^3 \text{ s}^{-1}$, flushing time = 15.25 hours

(a) Flushing region in black

(b) Surface tracer distribution at 6 Feb



(c) Flushing characteristics

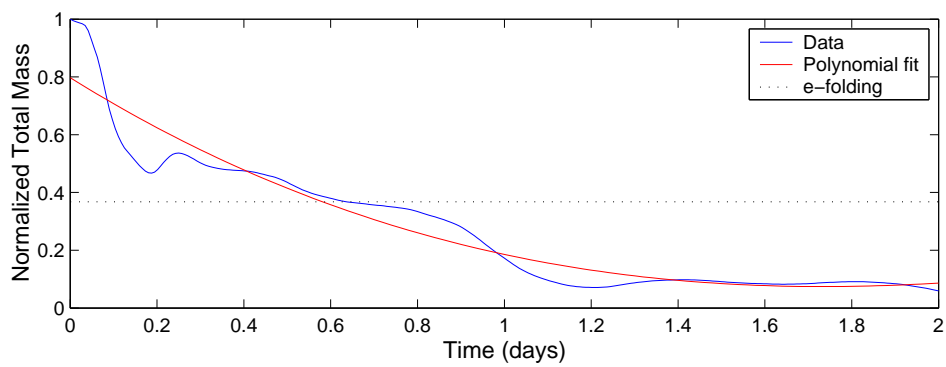
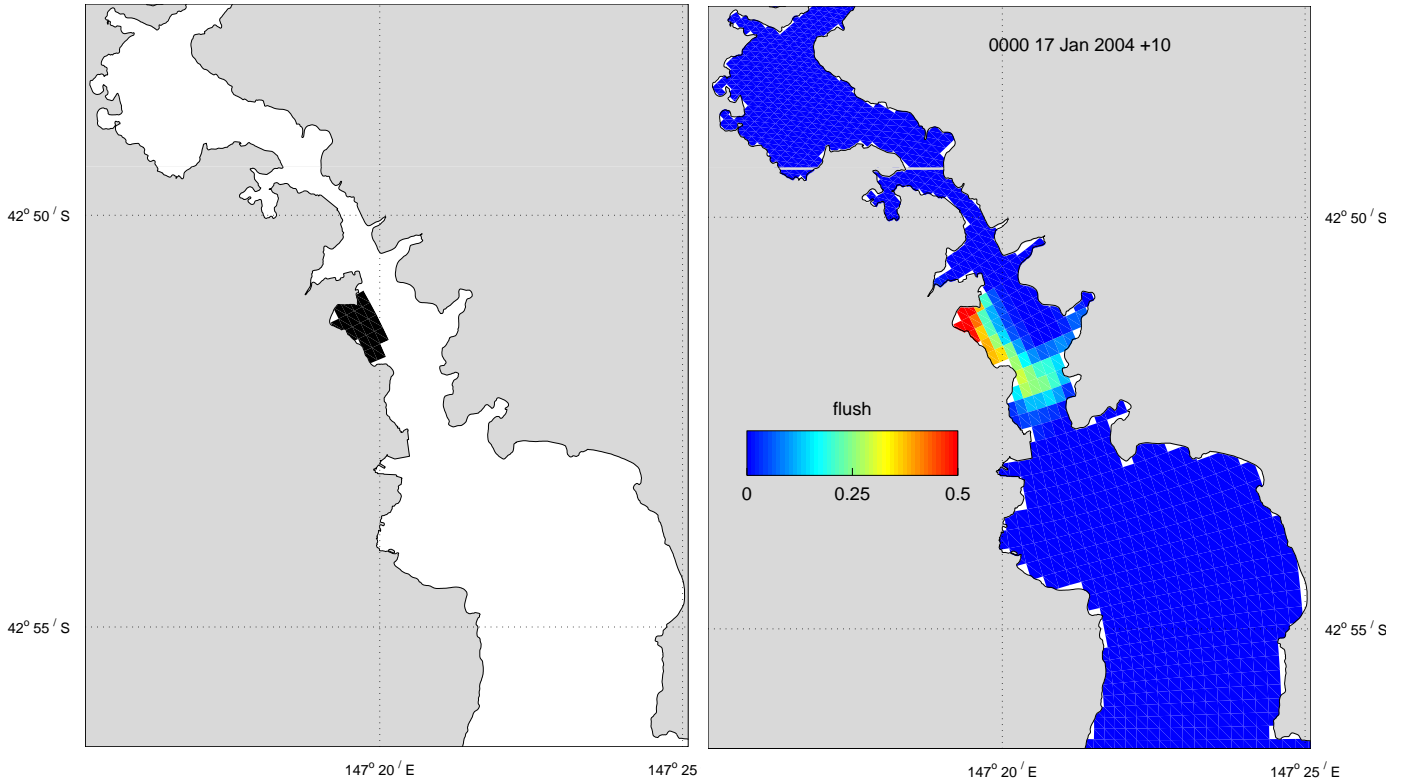


Figure 7.4.7 : Cornelian Bay flushing from 16 Jan 2004
Mean flow = $56 \text{ m}^3 \text{ s}^{-1}$, flushing time = 11.57 hours

(a) Flushing region in black

(b) Surface tracer distribution at 17 Jan



(c) Flushing characteristics

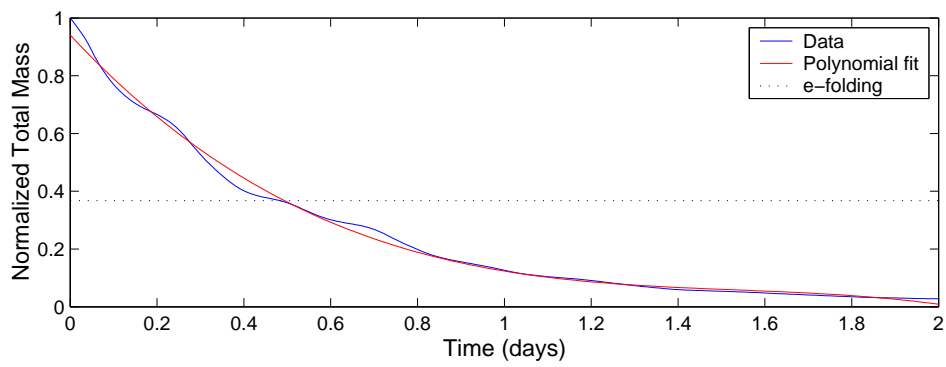
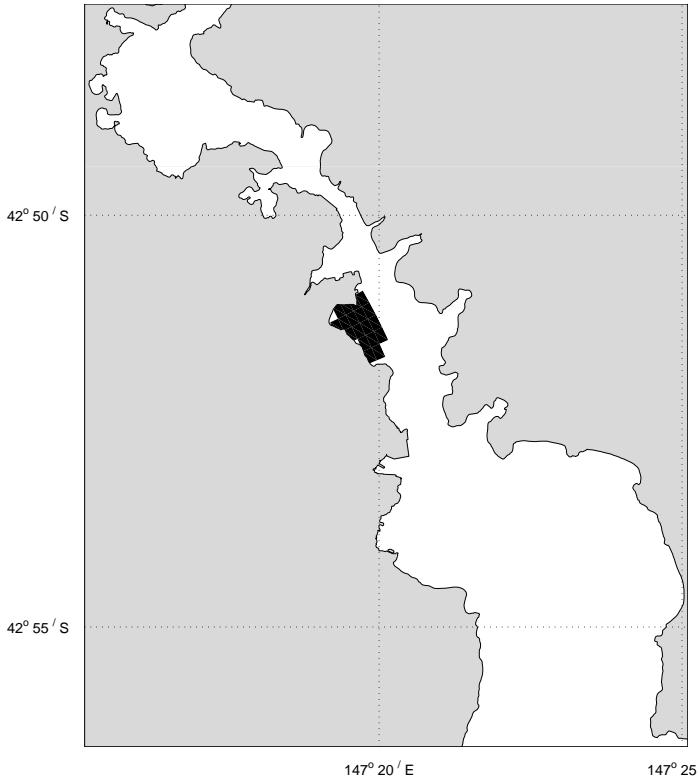
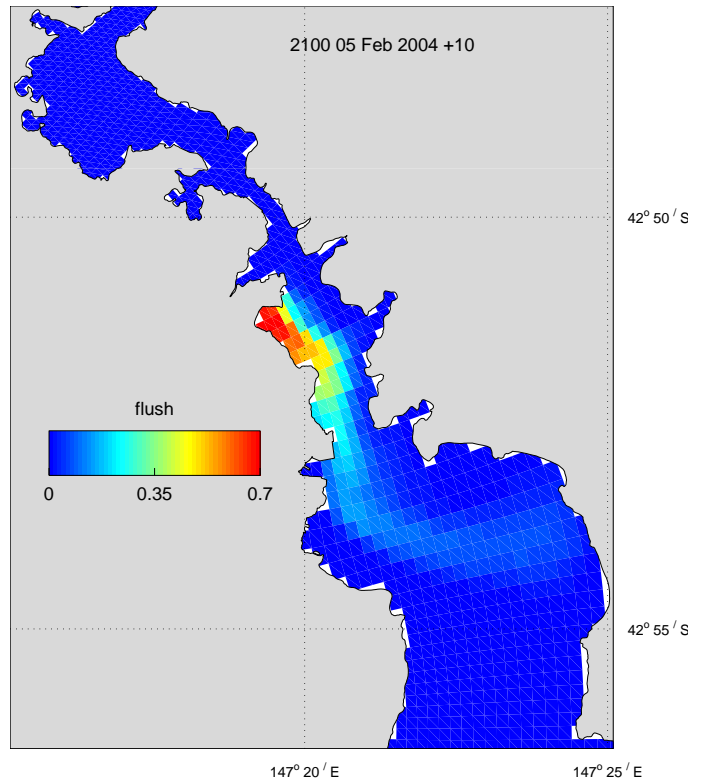


Figure 7.4.8 : Cornelian Bay flushing from 5 Feb 2004
Mean flow = $78 \text{ m}^3 \text{ s}^{-1}$, flushing time = 9.23 hours

(a) Flushing region in black



(b) Surface tracer distribution at 5 Feb



(c) Flushing characteristics

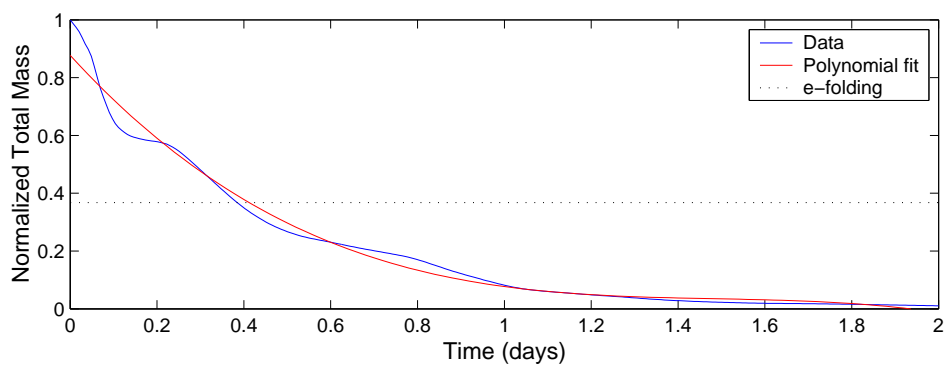
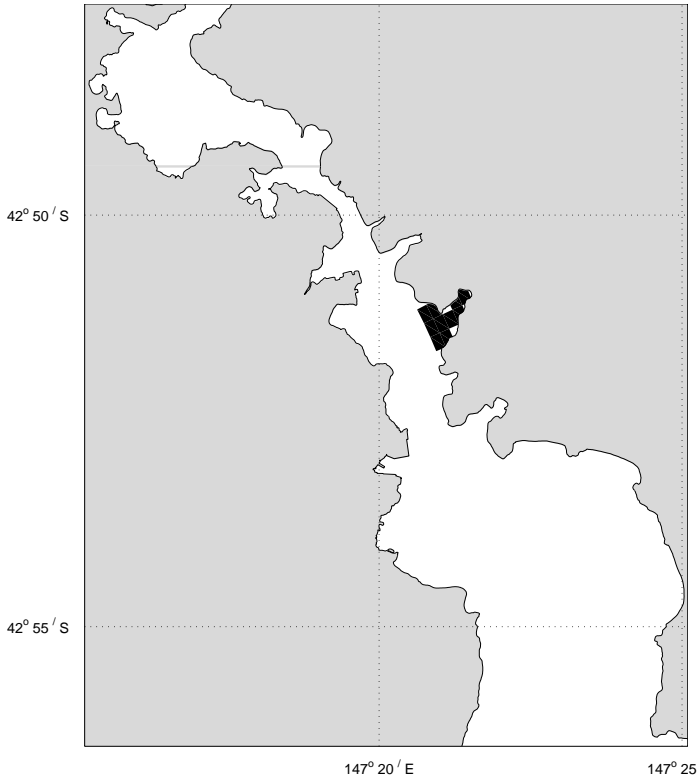
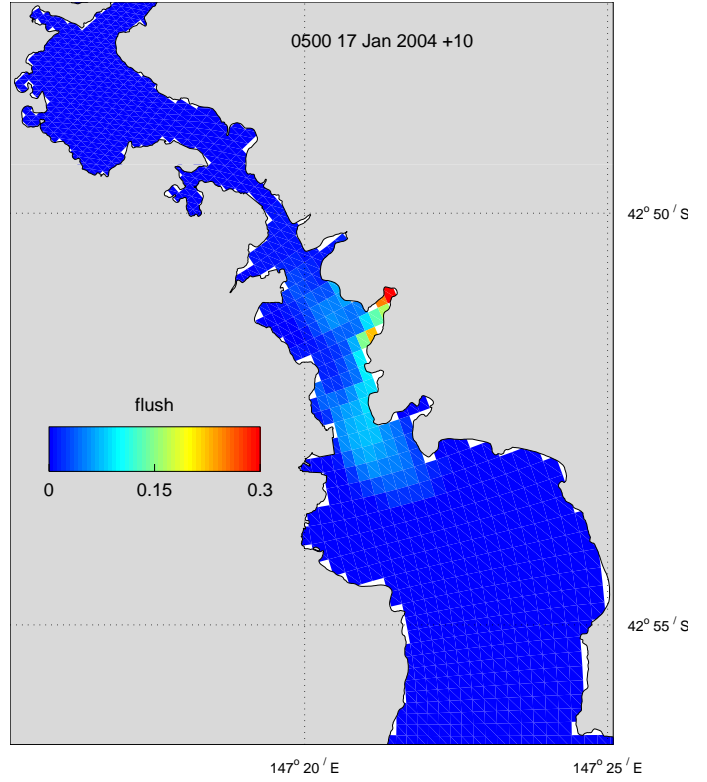


Figure 7.4.9 : Geilston Bay flushing from 16 Jan 2004
Mean flow = $56 \text{ m}^3\text{s}^{-1}$, flushing time = 13.12 hours

(a) Flushing region in black



(b) Surface tracer distribution at 17 Jan



(c) Flushing characteristics

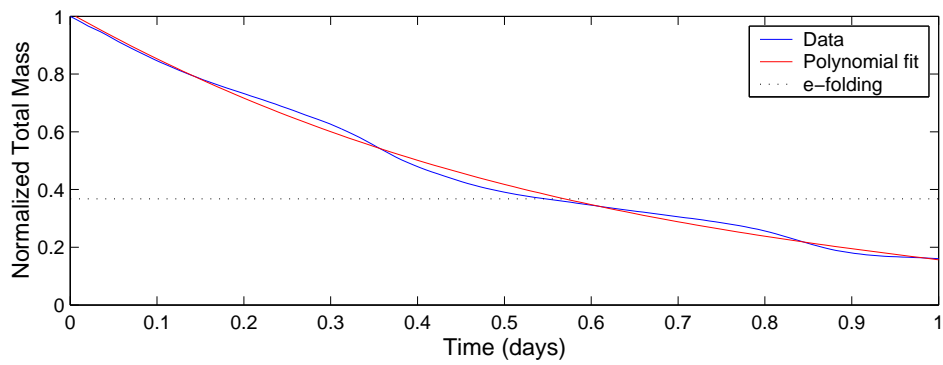
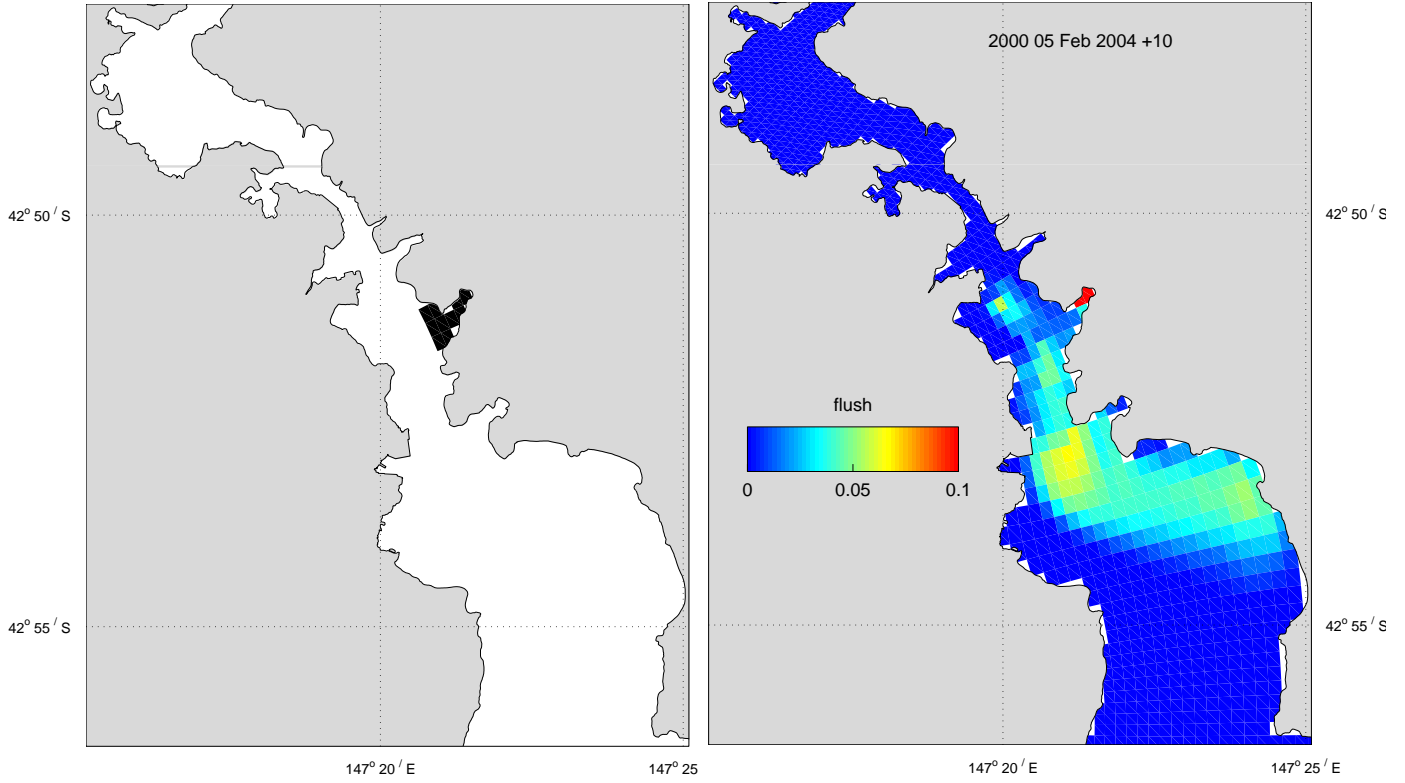


Figure 7.4.10 : Geilston Bay flushing from 5 Feb 2004
Mean flow = $78 \text{ m}^3 \text{ s}^{-1}$, flushing time = 7.68 hours

(a) Flushing region in black

(b) Surface tracer distribution at 5 Feb



(c) Flushing characteristics

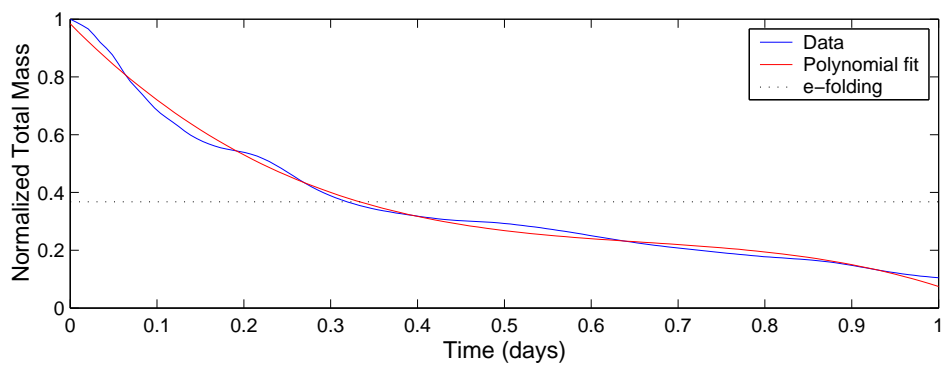
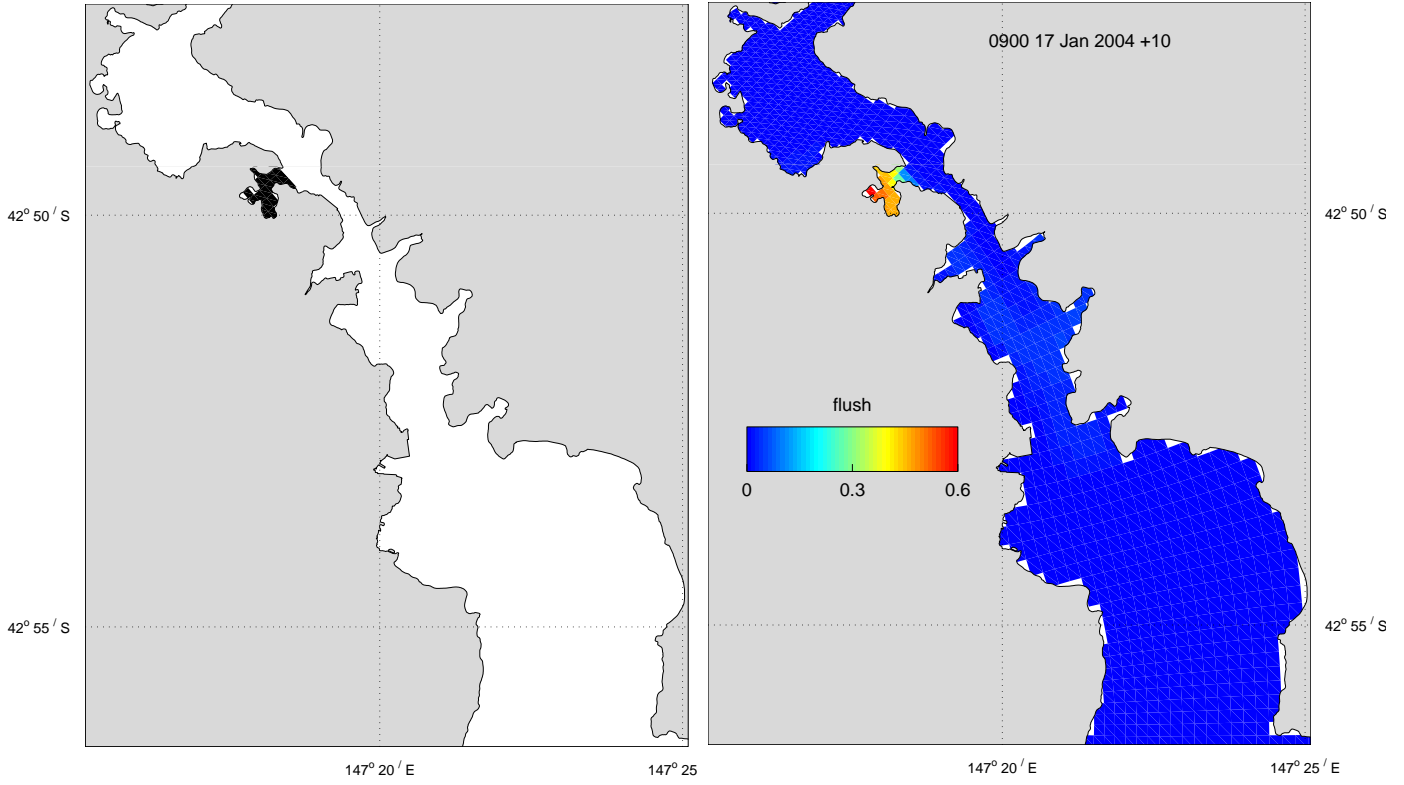


Figure 7.4.11 : Prince of Wales flushing from 16 Jan 2004
Mean flow = $56 \text{ m}^3\text{s}^{-1}$, flushing time = 21.12 hours

(a) Flushing region in black

(b) Surface tracer distribution at 17 Jan



(c) Flushing characteristics

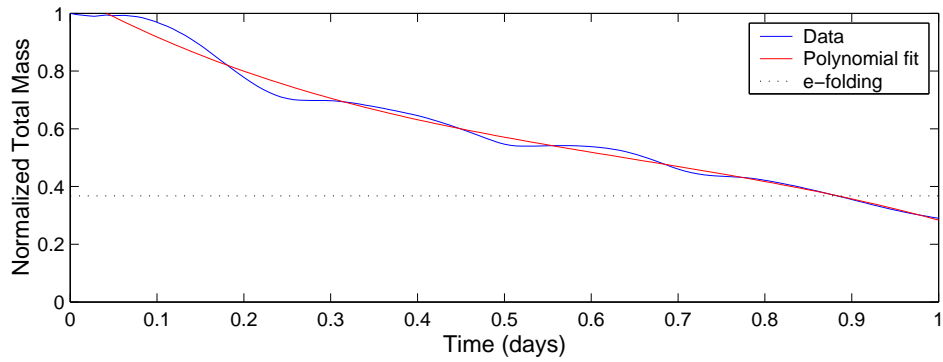
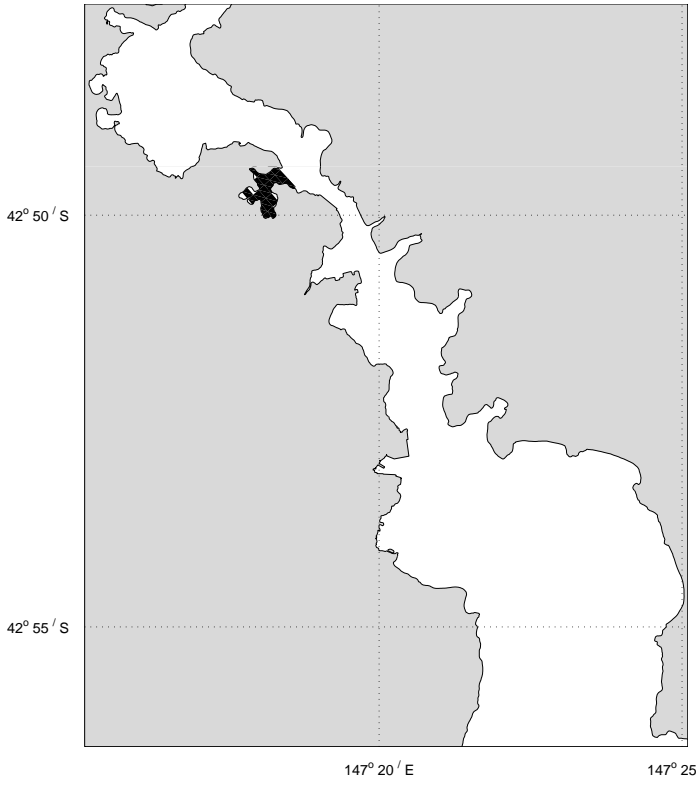
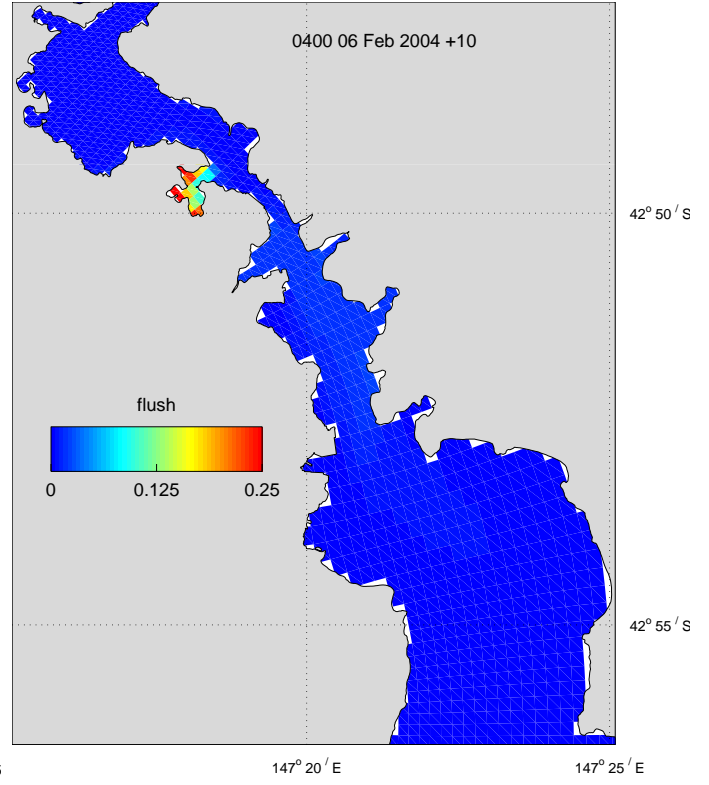


Figure 7.4.12 : Prince of Wales Bay flushing from 5 Feb 2004
Mean flow = $78 \text{ m}^3\text{s}^{-1}$, flushing time = 16.01 hours

(a) Flushing region in black



(b) Surface tracer distribution at 6 Feb



(c) Flushing characteristics

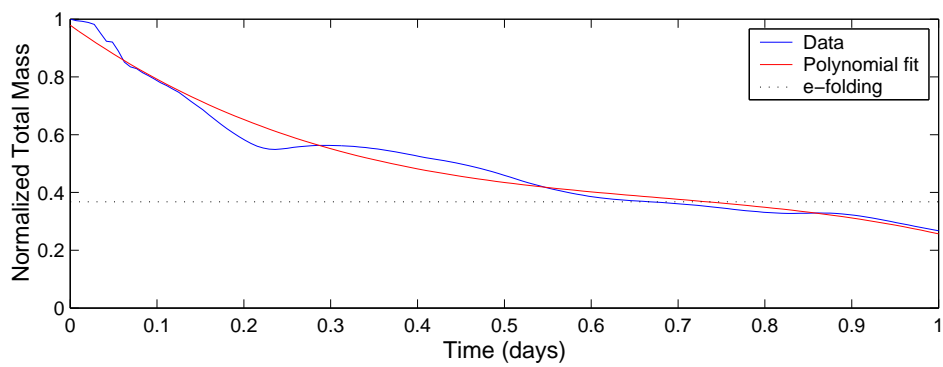
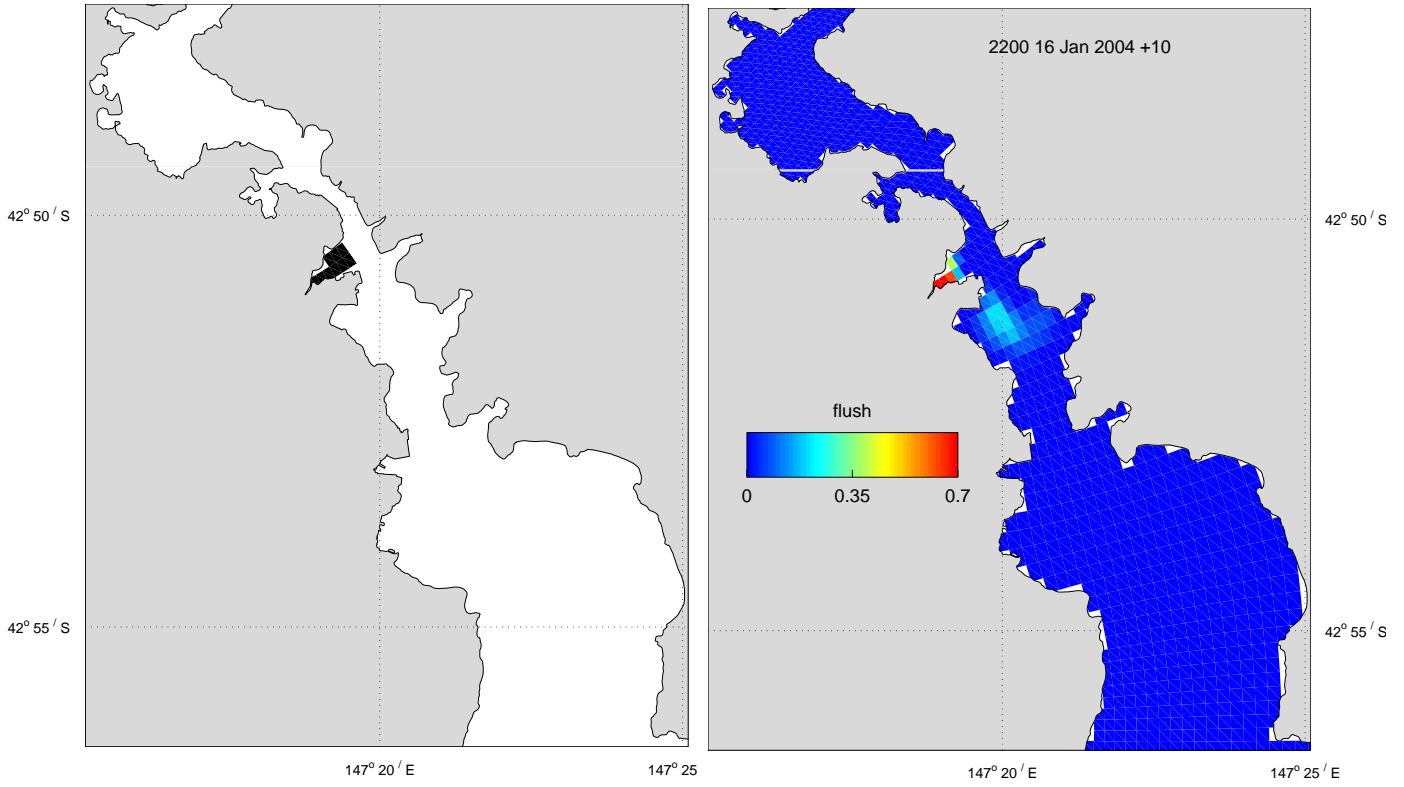


Figure 7.4.13 : New Town Bay flushing from 16 Jan 2004
Mean flow = $56 \text{ m}^3 \text{ s}^{-1}$, flushing time = 9.67 hours

(a) Flushing region in black

(b) Surface tracer distribution at 16 Jan



(c) Flushing characteristics

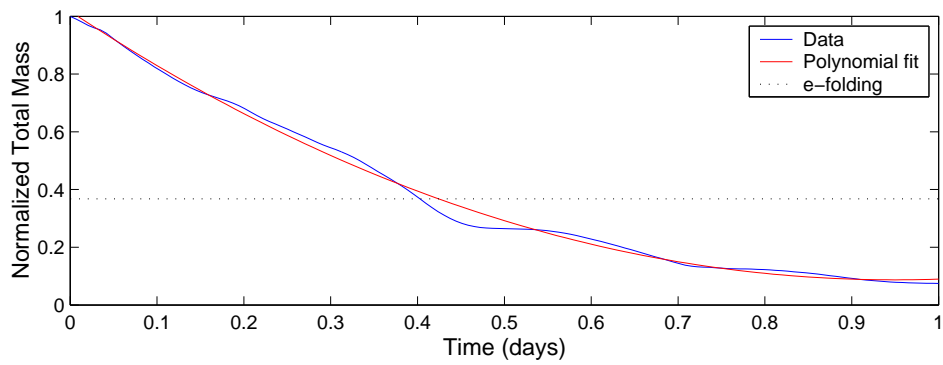
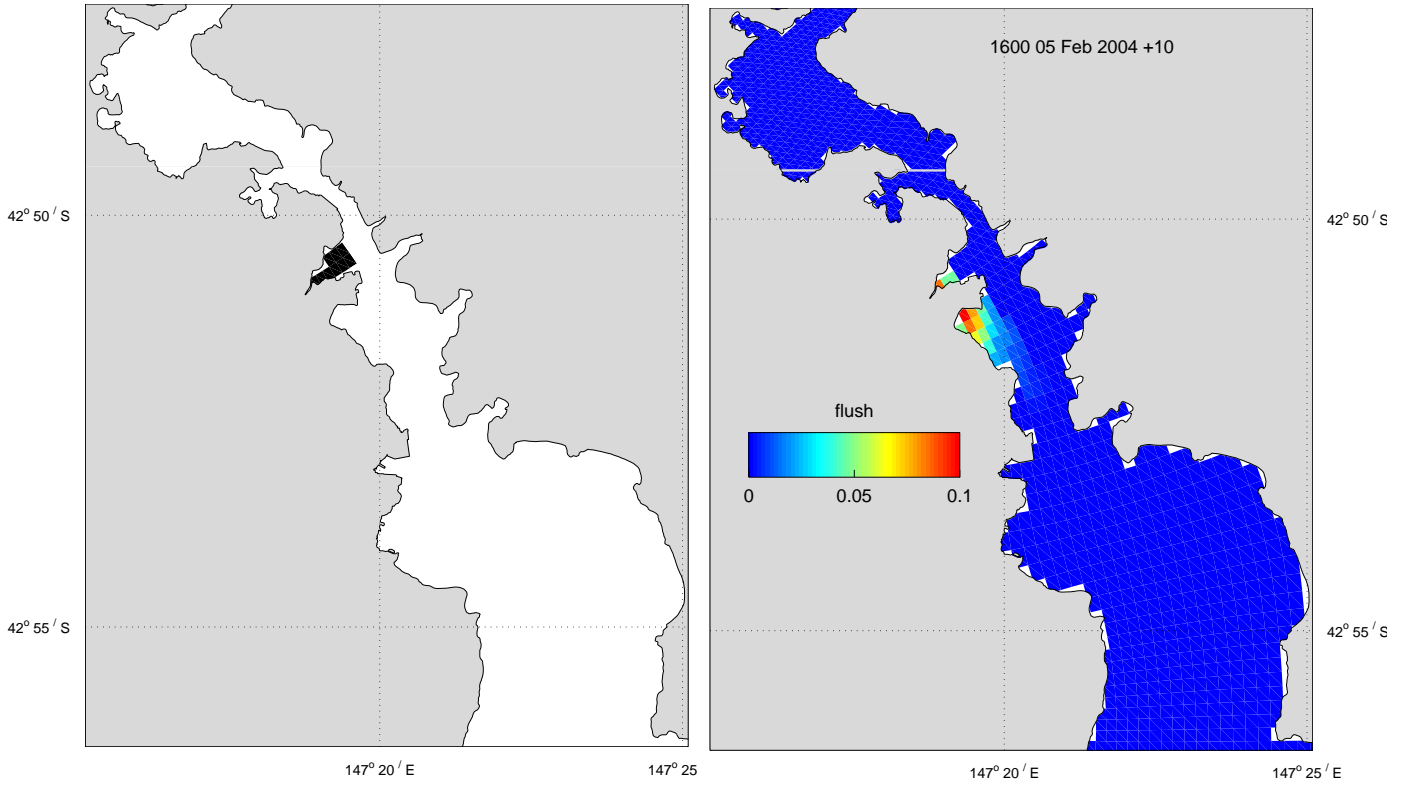


Figure 7.4.14 : New Town Bay flushing from 5 Feb 2004
Mean flow = $78 \text{ m}^3 \text{ s}^{-1}$, flushing time = 4 hours

(a) Flushing region in black

(b) Surface tracer distribution at 5 Feb



(c) Flushing characteristics

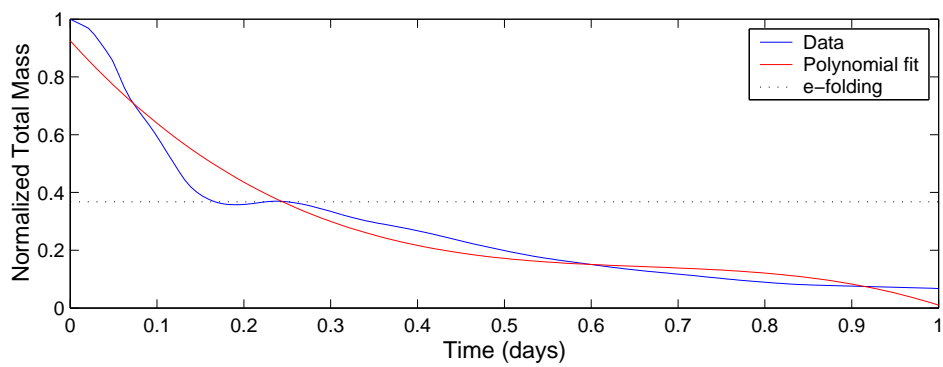
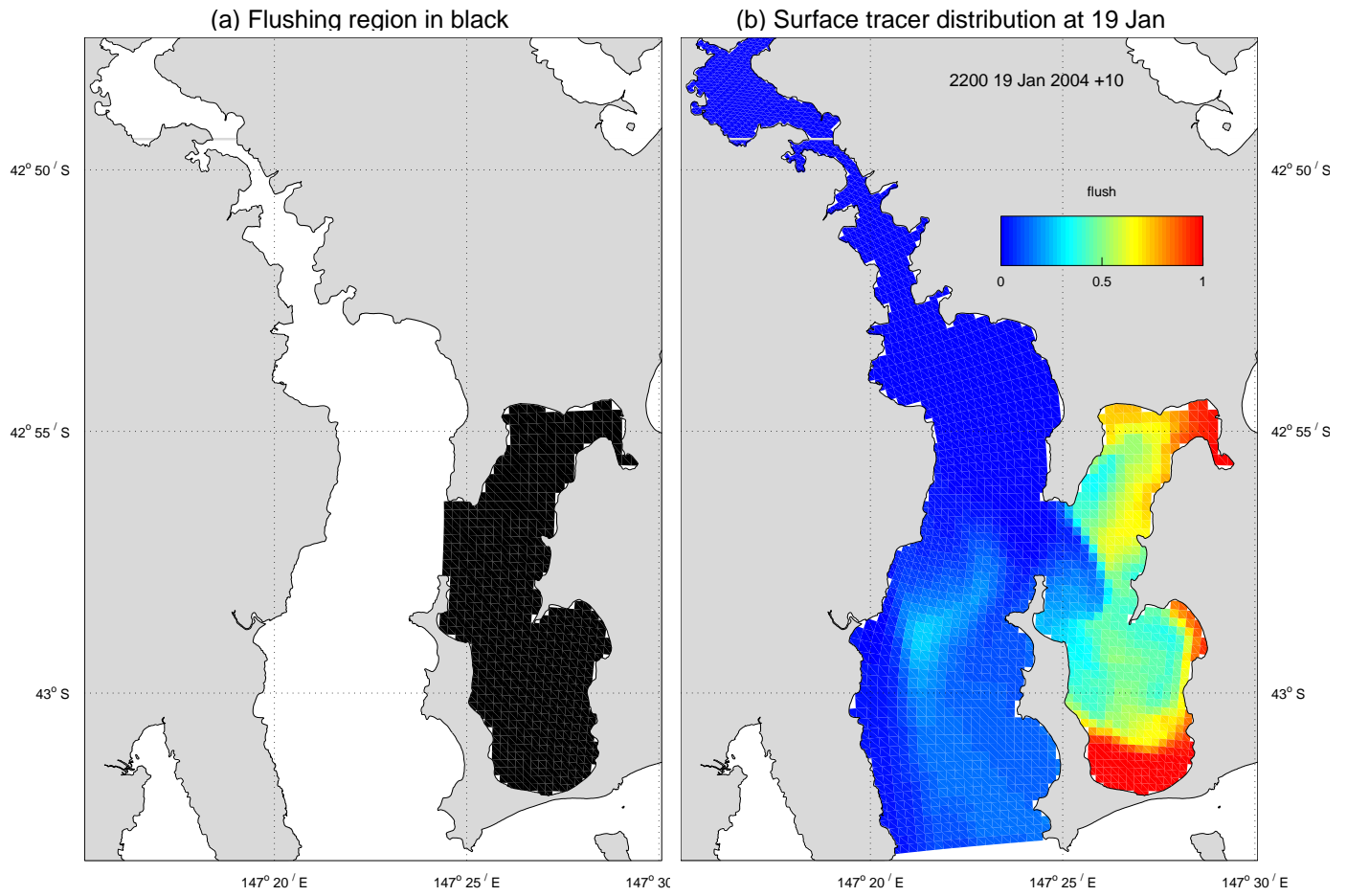


Figure 7.4.15 : Ralphs Bay flushing from 16 Jan 2004
Mean flow = $56 \text{ m}^3 \text{ s}^{-1}$, flushing time = 3.42 days



(c) Flushing characteristics

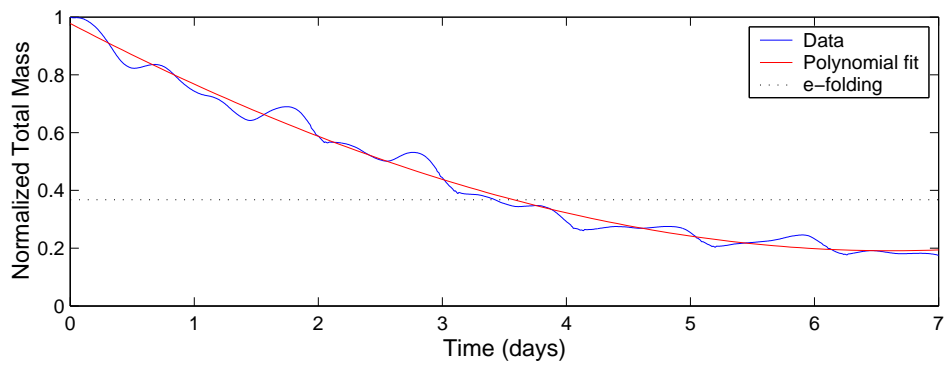
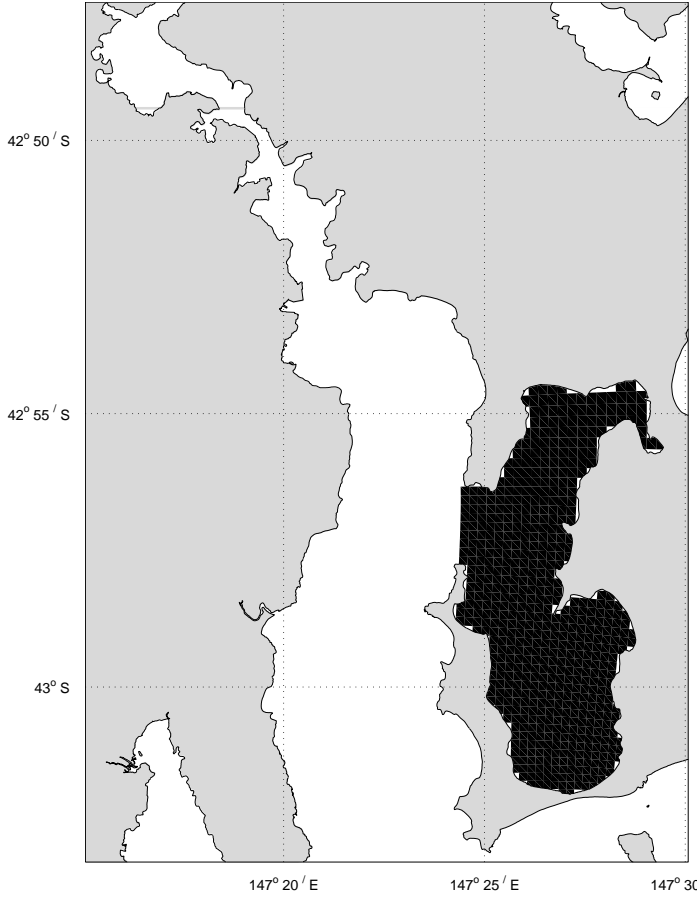
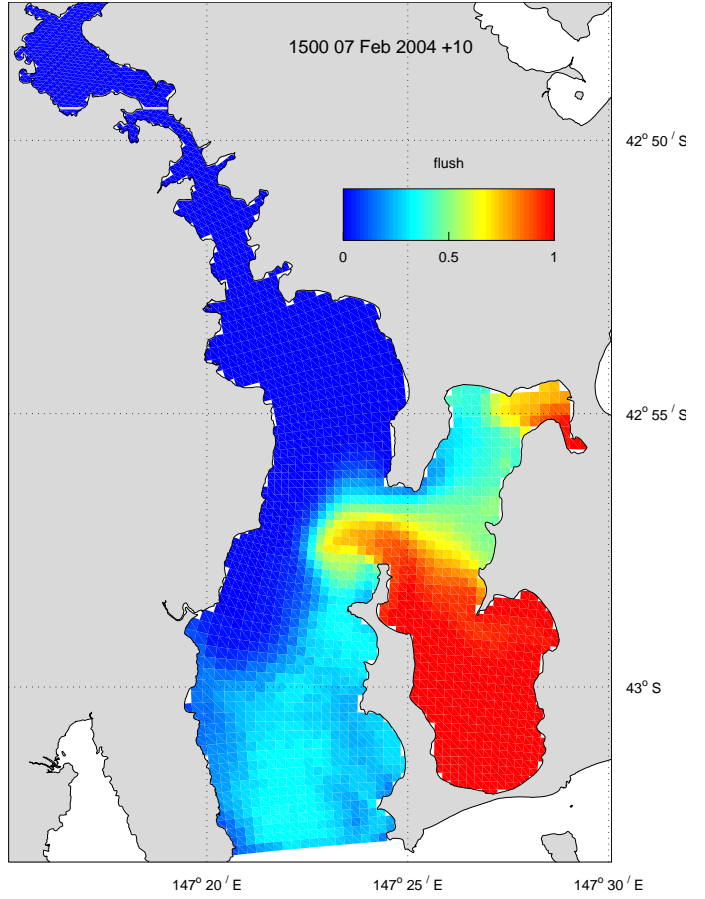


Figure 7.4.16 : Ralps Bay flushing from 5 Feb 2004
Mean flow = $78 \text{ m}^3\text{s}^{-1}$, flushing time = 2.14 days

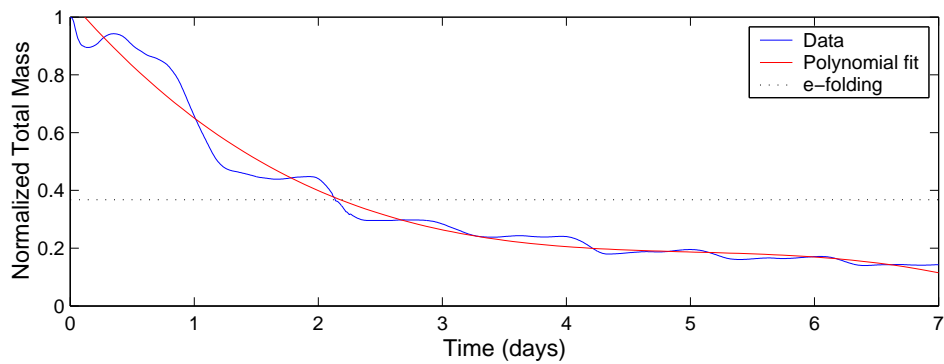
(a) Flushing region in black



(b) Surface tracer distribution at 7 Feb



(c) Flushing characteristics



7.5 Mixing Zones

Point sources of tracers were continuously input into the water column at locations corresponding to a number of sites (Figure 7.5.1 and Table 7.5.1) with unit loads (assumed to be $1 \text{ gs}^{-1} \sim 31,500 \text{ kg/year}$, giving output concentrations in units of gm^{-3} , or mgL^{-1}) for the ~3 month simulation period of Dec 2003 - Mar 2004. Tracers were released into bottom waters, except the Zinifex release which was also released into the surface. Note that since the bathymetry used in the model is averaged over the grid discretisation, the release depth quoted in Table 7.5.1 may differ from actual STP depths and corresponds to bottom locations in the model grid. Surface tracer concentrations were output at 1 hour intervals and post-processed to compute the 5th, 50th (median) and 95th percentile distributions for the whole simulation, providing a statistical description of the distributions resulting from tracer transport over this period. Owing to the volume of information that must be stored to compute the statistical distributions, only distributions for the surface layer were attempted and it was not feasible to create plots in bottom waters or along sections down the estuary. Note that the response of the tracers to the interaction of the point source input with the system dynamics is linear, so that if the load were increased by some arbitrary factor then the corresponding concentrations can be scaled accordingly.

Results are displayed as Figure 7.5.2 to 7.5.9. Results are interpreted thus: given that a continuous unit load is input at the Blackmans Bay site and its distribution throughout the domain allowed to reach quasi-steady state, at any given location in the domain one would expect to find the concentrations less than those shown in Figure 7.5.2 (a) for 5% of the time, less than those in Figure 7.5.2 (b) for 50% of the time and less than those in Figure 7.5.2 (c) for 95% of the time. Note that the concentration scales in the figures for the three percentiles differ from one another.

Figure 7.5.1 : Mixing zone release locations

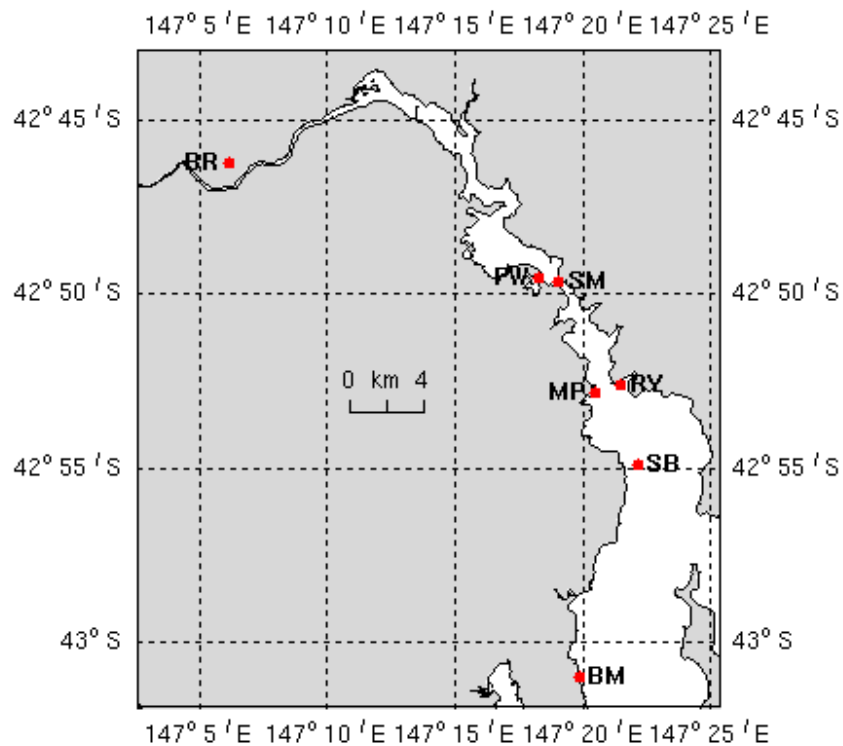


Table 7.5.1 : Mixing zone release characteristics
 Note : Position and depth refer to locations in the model grid.

Name	Location	Type	Latitude	Longitude	Depth (m)
BM	Blackmans Bay	STP	-43.016	147.331	5
SB	Blinking Billy at Sandy Bay	STP	-42.915	147.369	17
MP	Macquarie Point	STP	-42.880	147.342	14
RY	Rosny	STP	-42.877	147.359	10
BY	Boyer (Norske Skog)	CES	-42.770	147.103	4.5
PW	Prince of Wales	STP	-42.826	147.304	2
SM_t SM_b	Zinifex smelter		-42.828	147.318	0 (surface) 6 (bottom)

Generally the tracer distributions consist of a zone of higher concentration in a mixing zone around the release site, with lower concentrations distributed throughout much of the rest of the estuary. The shallower release sites (Prince of Wales Bay and surface Zinifex Smelter) show tracer distributions predominantly downstream from the release site, with higher concentrations than the deeper release sites. Maximum surface concentrations are confined to the immediate vicinity of the release, and for the 95 percentile distributions these are of the order of 0.004. The median distributions for Sandy Bay, Rosny and Macquarie Point do not show this higher concentration mixing zone as clearly, having relatively uniform distributions throughout the middle of the estuary. Also, the bottom Zinifex Smelter release results in uniform median and 95 percentile distributions throughout the middle and upper estuary, with the largest surface 95 percentile concentrations of > 0.01 found in Elwick Bay. Tracer is confined to the vicinity of the release site in Prince of Wales Bay to a greater degree than other sites, consequently resulting in elevated concentrations in this Bay (95 percentile concentration of ~0.06). The Boyer release results in higher tracer values than other site releases, with median concentrations > 0.05 upstream of Elwick Bay. This is a result of the bulk of the release occurring directly into the downstream freshwater flow, whereas the other sites are released in the salt wedge in bottom waters and only manifest in the surface layer via entrainment across the halocline. It is envisioned that concentrations at the other sites are much greater in bottom waters. While the model does not resolve the Derwent River above Bridgewater accurately, the distribution of tracer released at New Norfolk is accurately represented below Bridgewater, as evidenced by the sound calibration to salinity. Therefore, the tracer distribution from the Boyer site can be considered realistic below Bridgewater.

Figure 7.5.2 : Blackmans Bay surface percentile distributions

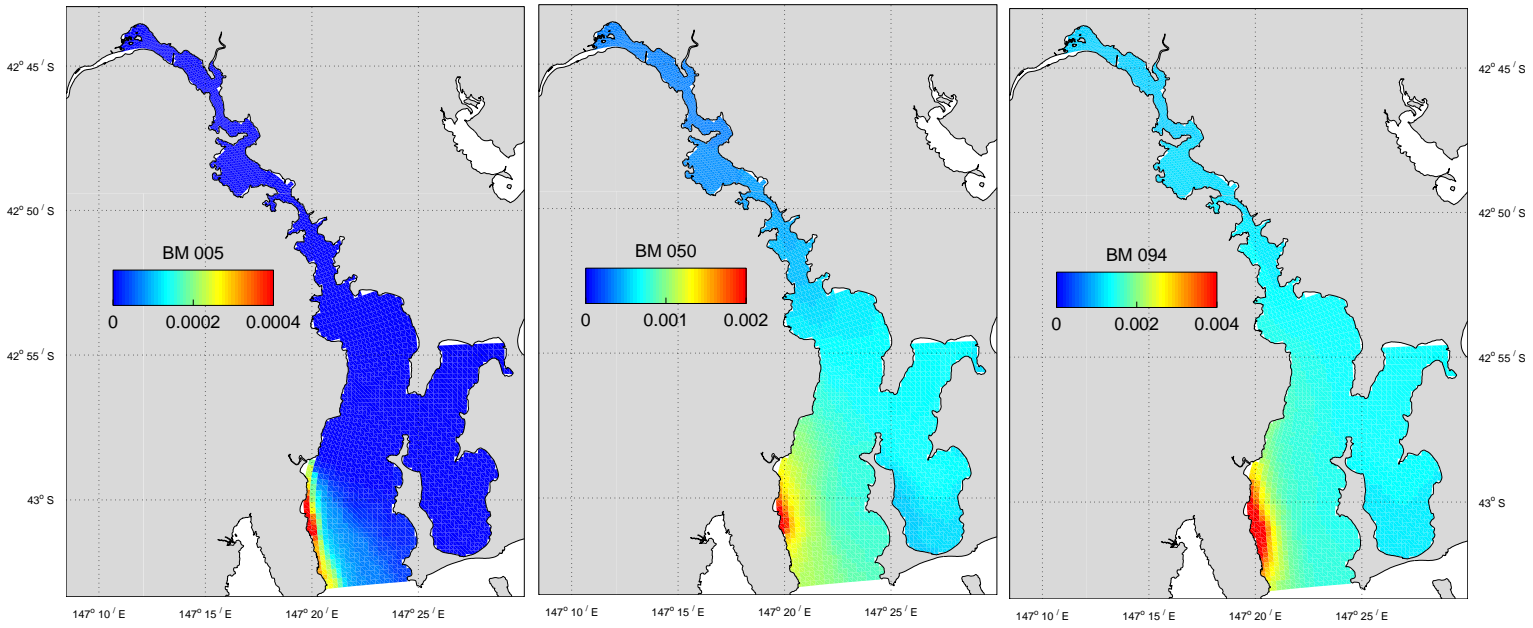


Figure 7.5.3 : Sandy Bay (Blinking Billy) surface percentile distributions

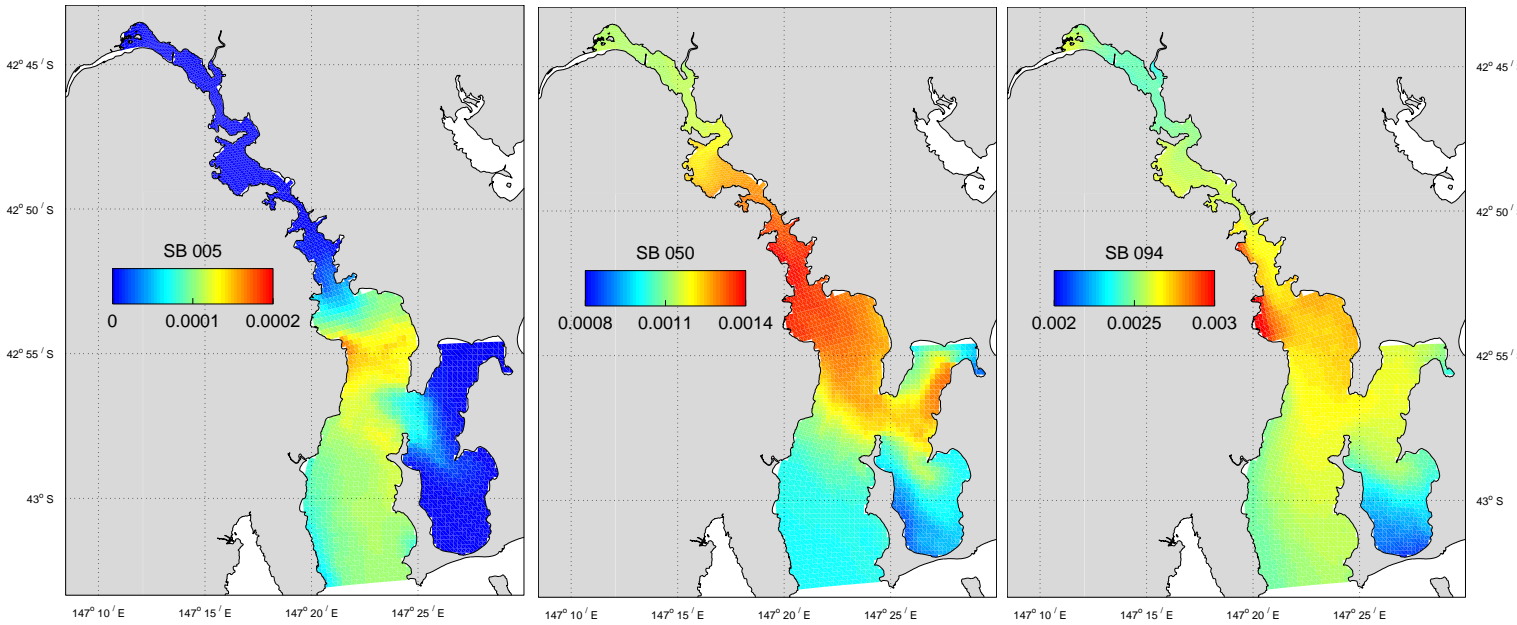


Figure 7.5.4 : Macquarie Point surface percentile distributions

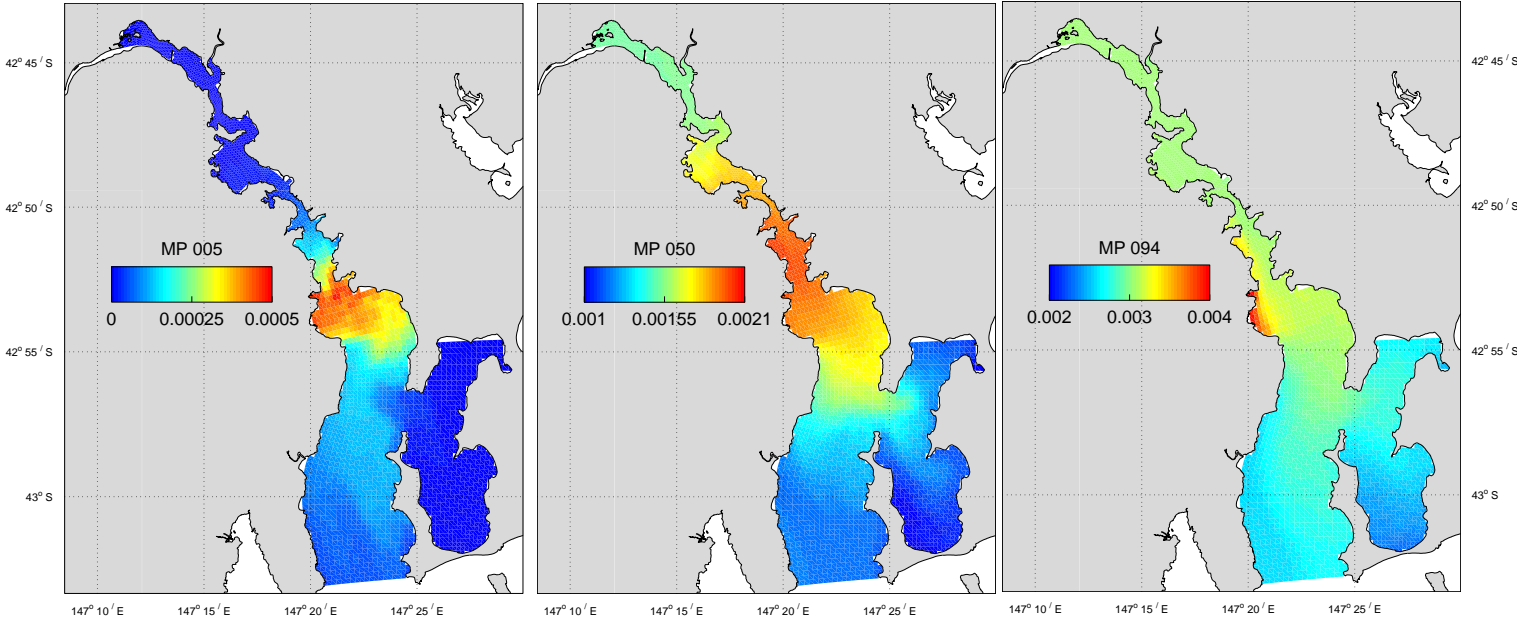


Figure 7.5.5 : Rosny surface percentile distributions

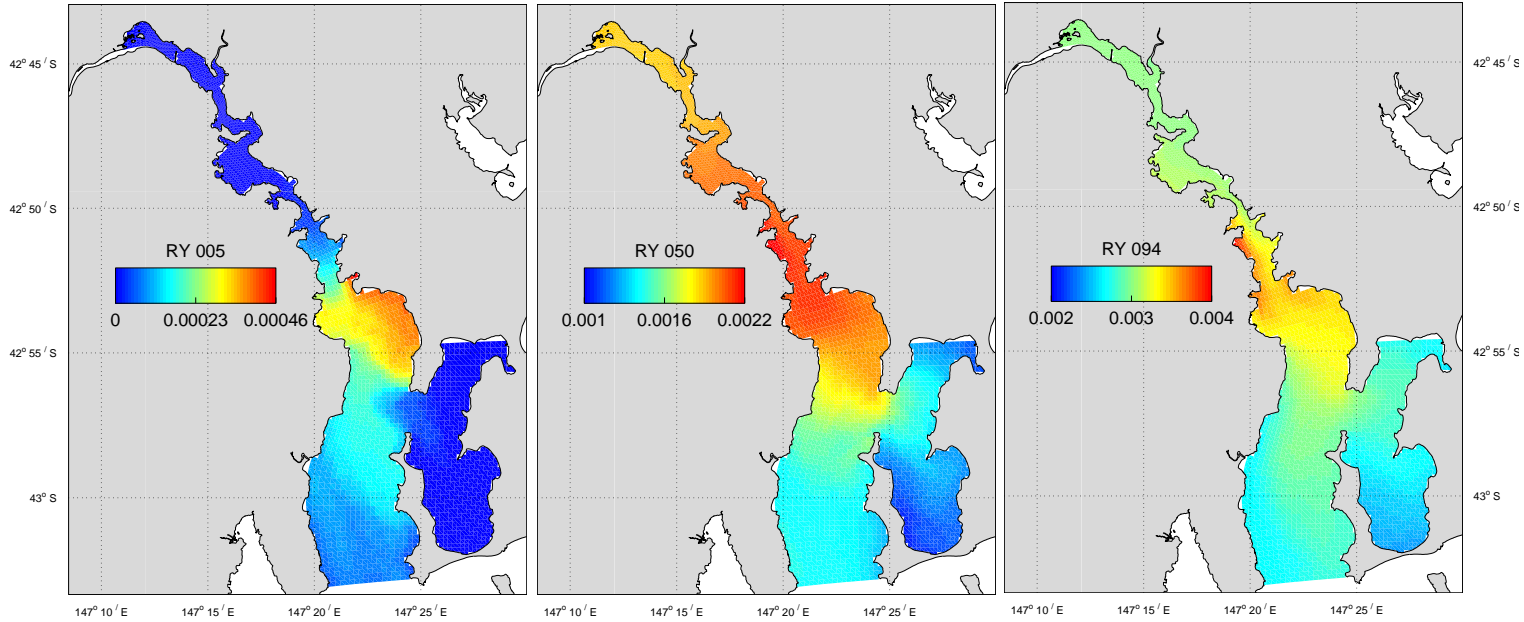


Figure 7.5.6 : Boyer (Norske Skog) surface percentile distributions

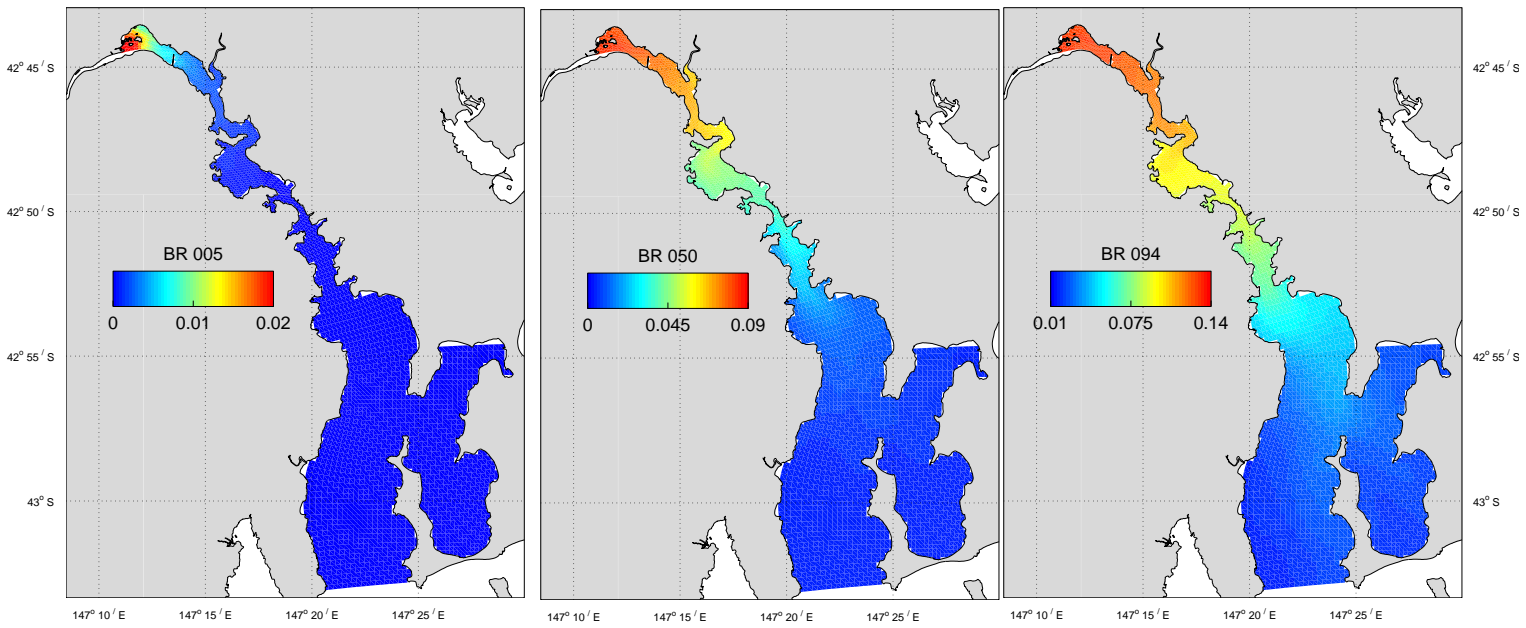


Figure 7.5.7 : Prince of Wales Bay surface percentile distributions

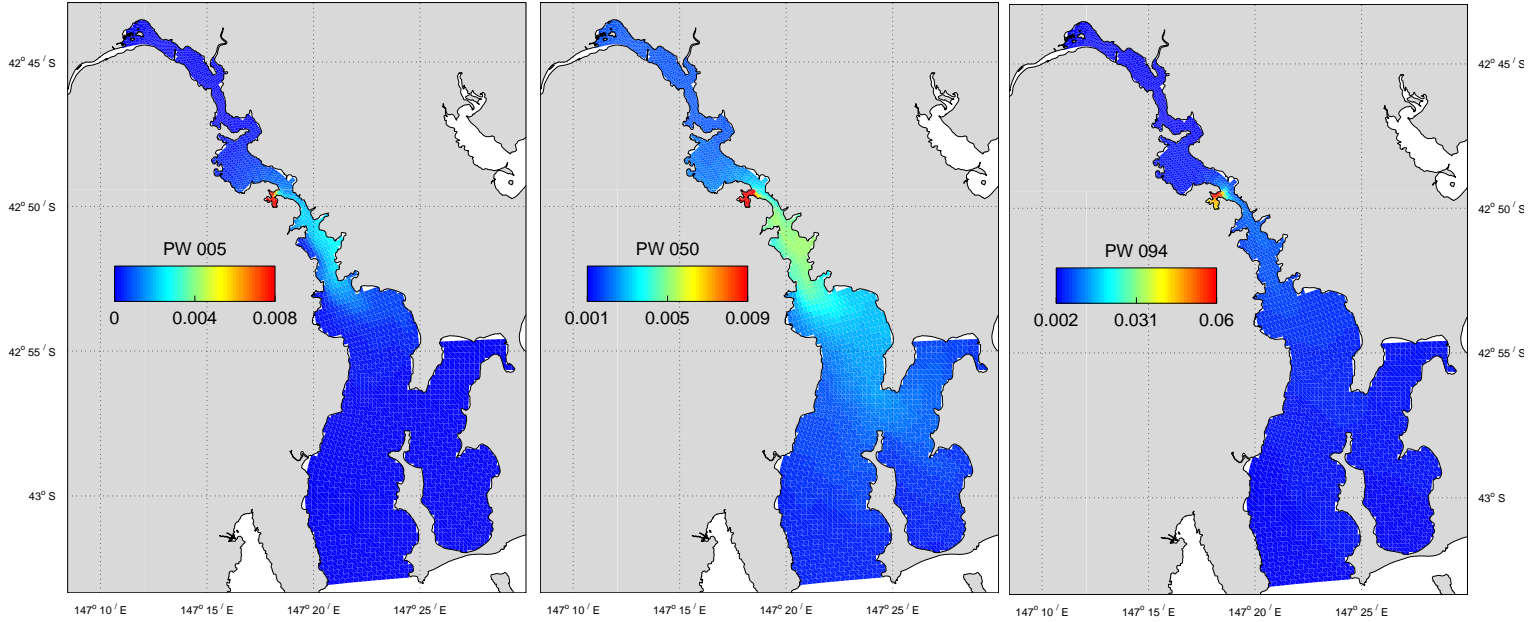


Figure 7.5.8 : Zinifex Smelter surface release surface percentile distributions

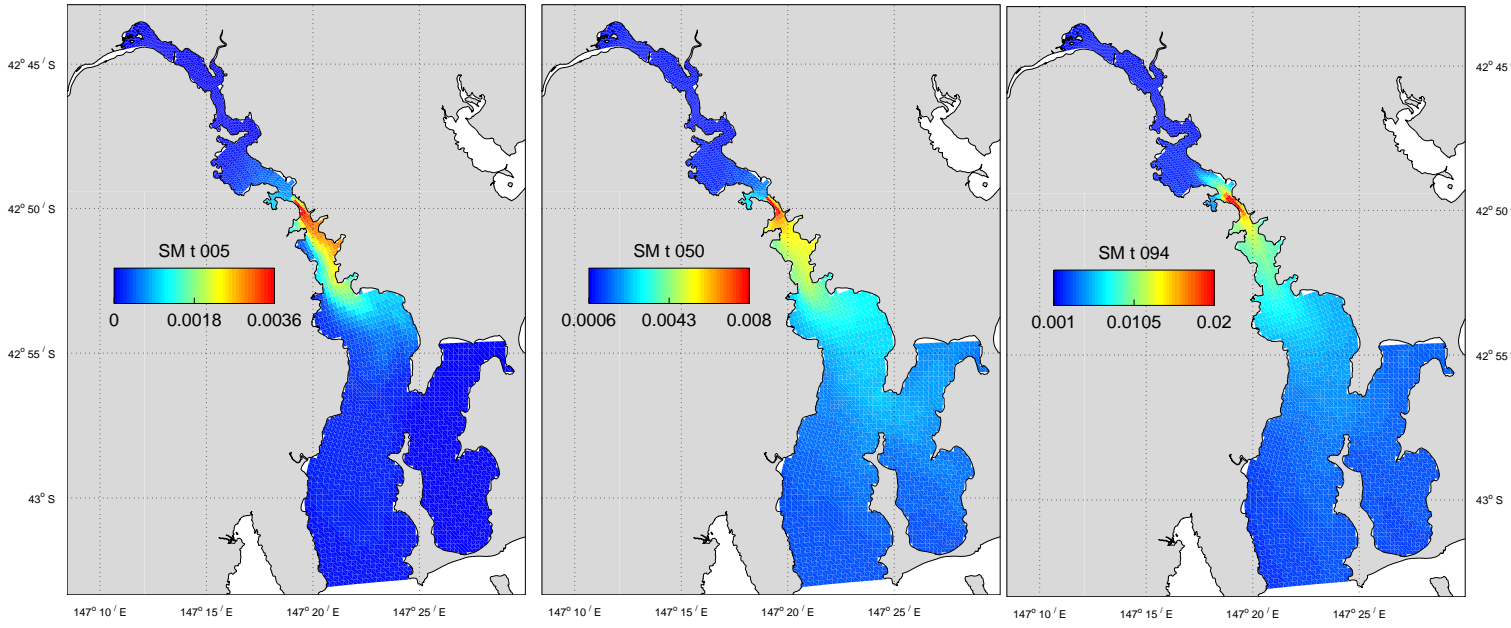
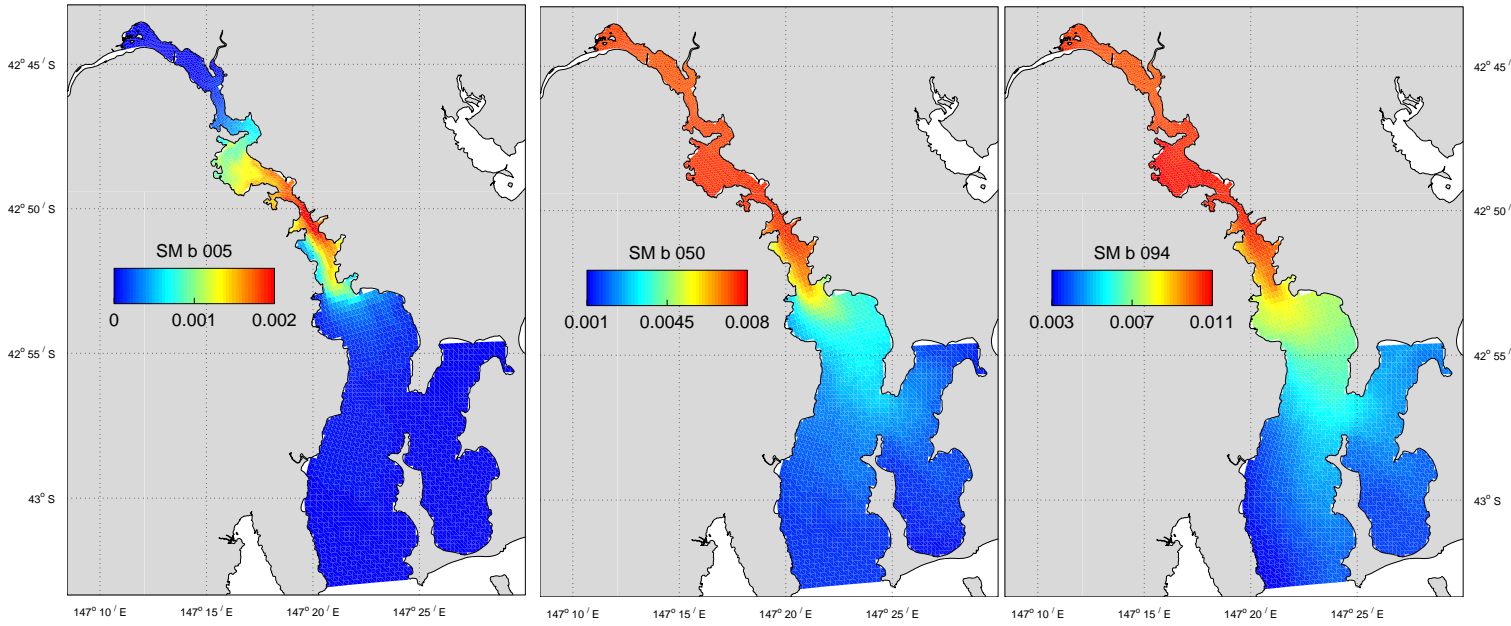


Figure 7.5.9 : Zinifex Smelter bottom release surface percentile distributions



7.6 Connectivity

The connectivity of the domain can be examined by observing the behaviour of neutrally buoyant particles released from the same locations as the point source releases in Section 7.5, and at the same depths. The particles were released at a rate of 2 particles / hour from an initial pool of 10,000 particles. These particles were subsequently advected with the circulation to provide insight into how various regions of the domain are connected. The particles are also subjected to random motion representing the effect of diffusion (i.e. sub-grid scale effects). Therefore, any two particles released from the same place at the same time are expected to undergo different trajectories due to this random motion. When a particle crosses the open boundary at the southern end of the model domain it is placed in the initial pool for subsequent re-release. The particle distributions after 3 months of simulation are displayed in Figures 7.6.1 to 7.6.8. This distribution is the projection of particles at all depths onto the surface. Particles are colour coded according to their age since being released over the range 0 – 7 days (i.e. blue particles are 0 days old, red particles are > 7 days old).

Particles are reasonably evenly distributed throughout the whole estuary from each release site, indicating the estuary is well connected. The release sites in deeper bottom waters within the salt wedge especially support this trend, whereas the shallower or surface releases (Prince of Wales Bay, Boyer and Zinifex surface) result in distributions predominantly downstream of the source. This is consistent with the residual flow analysis which suggests a net flow up-stream flow in the salt wedge and downstream flow in the surface layer. In the long term particles are expected to follow trajectories corresponding to this mean flow. Few of the particles released at Blackmans Bay in the lower estuary were found in the upper estuary, whereas a release further upstream in the lower estuary (Sandy Bay) resulted in larger numbers of particles finding their way into the upper reaches of the estuary. Distributions resulting from releases at Sandy Bay, Rosny and Macquarie Point were all similar. The bottom Zinifex release and the Boyer release resulted in the greatest connectivity within the domain. It can be seen that many of the particles have ages greater than 7 days. Of all particles released from all sites, there existed 27297 particles that were lost through the open boundaries, and the mean age of these particles was 11.7 days which is comparable to the lower flow ($56 \text{ m}^3 \text{ s}^{-1}$) whole-estuary flushing estimate.

Note that the images presented below are a snapshot of the particle distribution at the end of the simulation, and will vary in accordance with the forcing in effect. Due to this an animation of the particle trajectories best conveys the connectivity of the region, although observation of isolated particle trajectories does supply insight into the dynamics of the system. The trajectories of particles were traced during high flow (Jan 31, Figures 7.6.8 & 7.6.9, flow $\sim 180 \text{ m}^3 \text{ s}^{-1}$) and low flow (Dec 17, Figures 7.6.10 & 7.6.11, flow $\sim 30 \text{ m}^3 \text{ s}^{-1}$) conditions. The tide during these periods was mid neap-spring cycle and spring tide respectively, with variable wind conditions. Note that circles correspond to the start of the trajectory and squares to the end in these figures. Particle trajectories are superimposed on the surface from all depth levels, hence an upstream particle trajectory is most likely a result of the particle residing in the bottom layer. Trajectories of particles in the surface layer (i.e. downstream) were attempted to be identified. The high flow conditions show downstream trajectories during the ebb tide, and downstream in the upper and mid-estuary with upstream in the lower estuary during the flood tide. This reflects the net downstream motion during high flow conditions. In comparison, the low flow conditions show downstream trajectories during the ebb and upstream during the flood tide over the whole estuary. Tidal excursions may be as large as 8km.

Figure 7.6.1 : Blackmans Bay

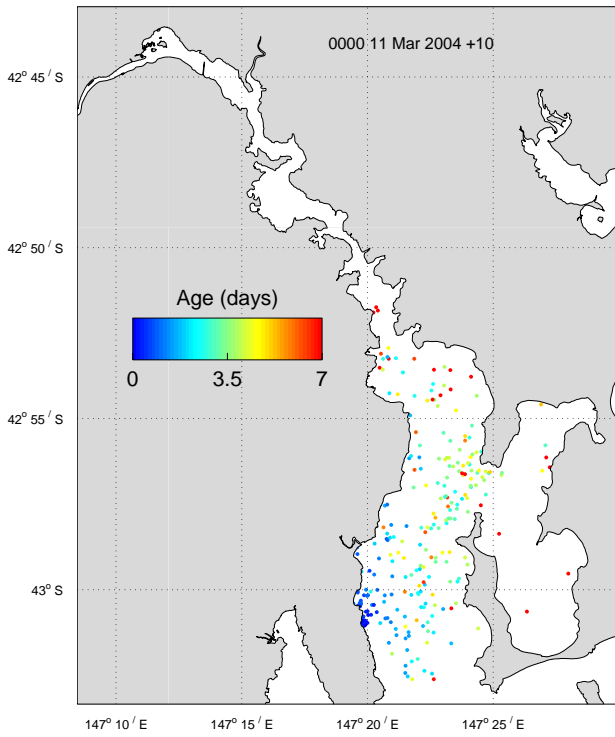


Figure 7.6.2 : Sandy Bay

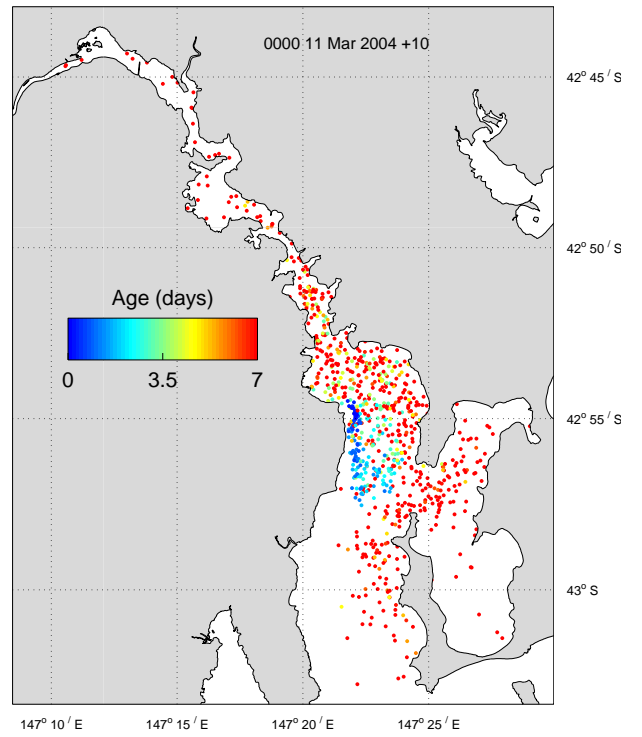


Figure 7.6.3 : Macquarie Point

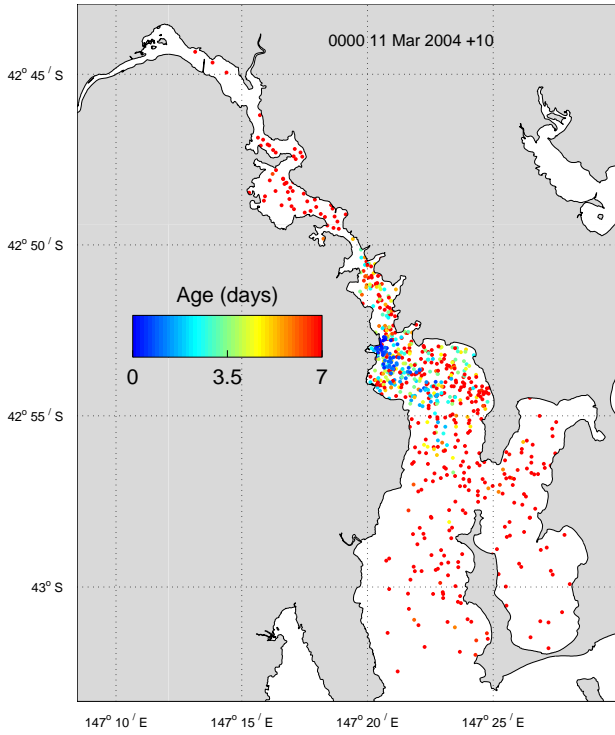


Figure 7.6.4 : Rosny

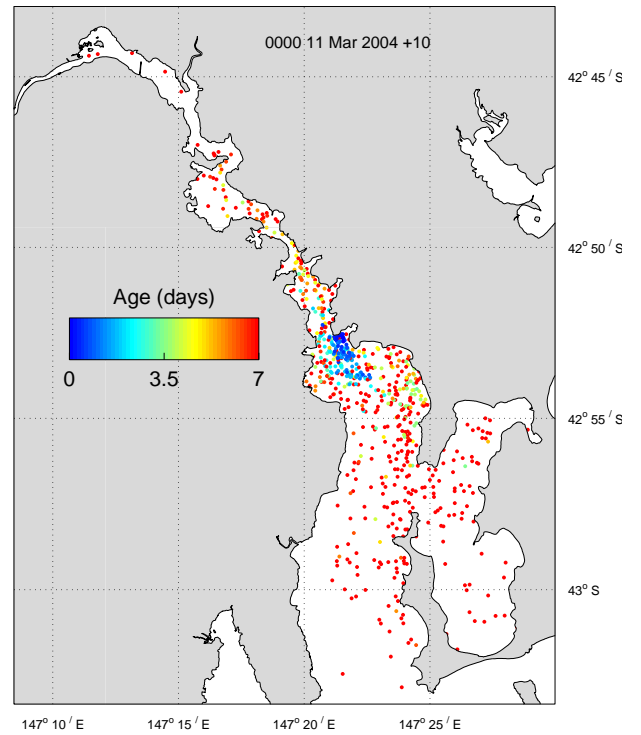


Figure 7.6.5 : Boyer

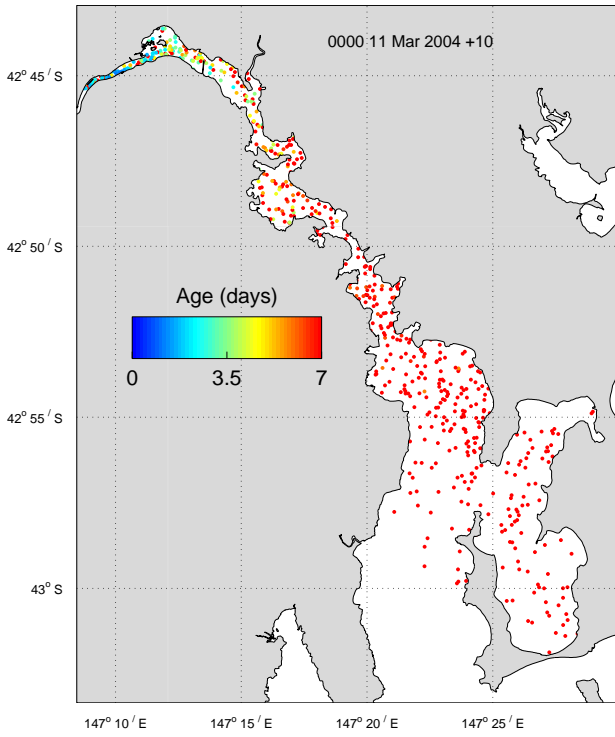


Figure 7.6.6 : Prince of Wales Bay

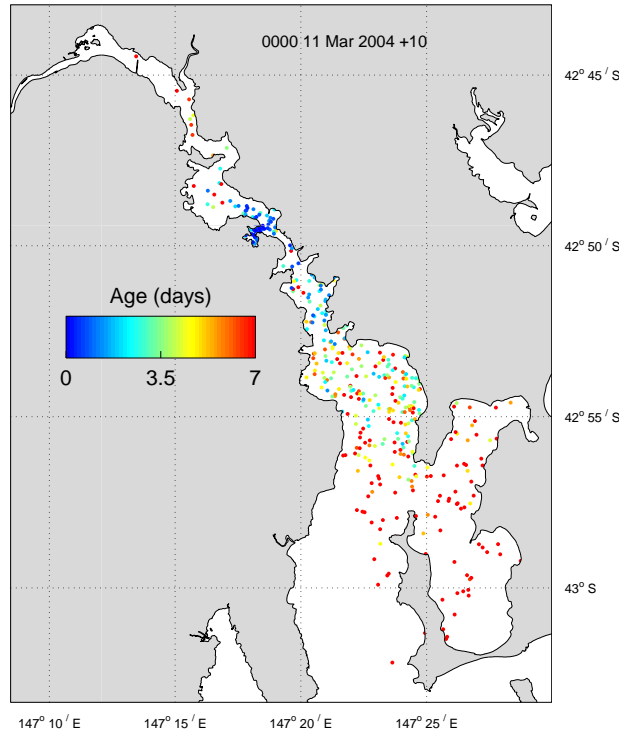


Figure 7.6.7 : Zinifex Smelter, surface

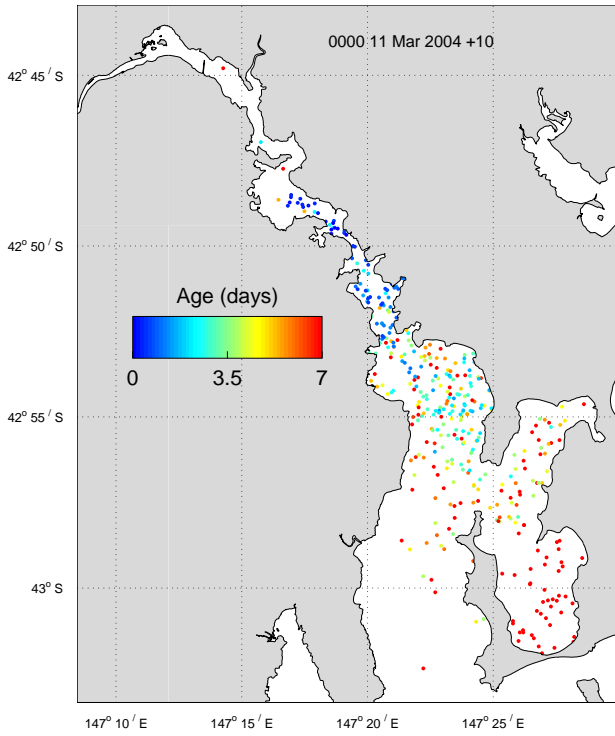


Figure 7.6.8 : Zinifex Smelter, bottom

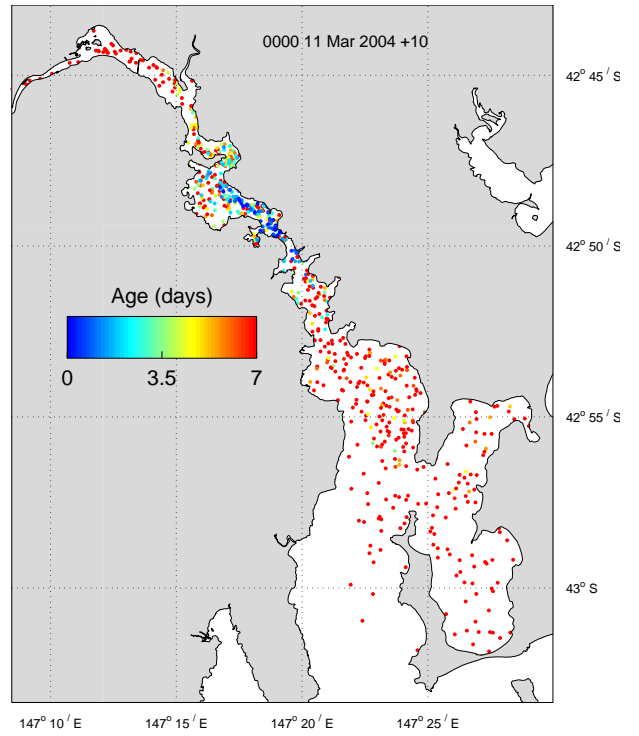


Figure 7.6.8 : Jan 31
 High flow conditions ($\sim 180 \text{ m}^3\text{s}^{-1}$)
 Ebb tide (range = 0.87m)

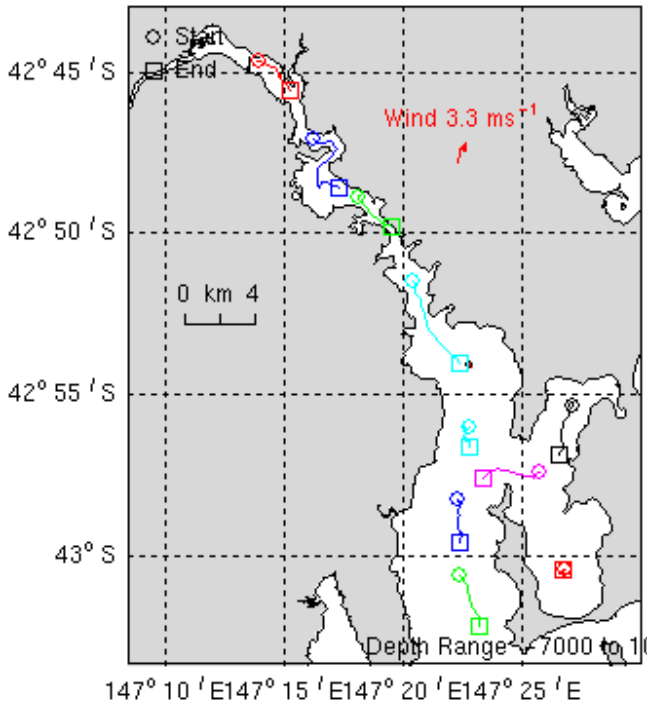


Figure 7.6.9 : Jan 31
 High flow conditions ($\sim 180 \text{ m}^3\text{s}^{-1}$)
 Flood tide (range = 0.99m)

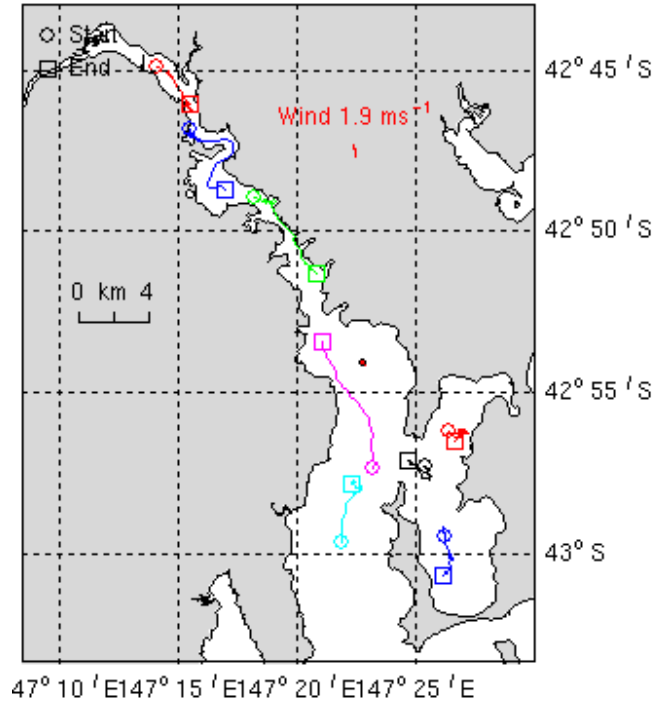


Figure 7.6.10 : Dec 27
 Low flow conditions ($\sim 30 \text{ m}^3\text{s}^{-1}$)
 Ebb tide (range $\sim 1.16\text{m}$)

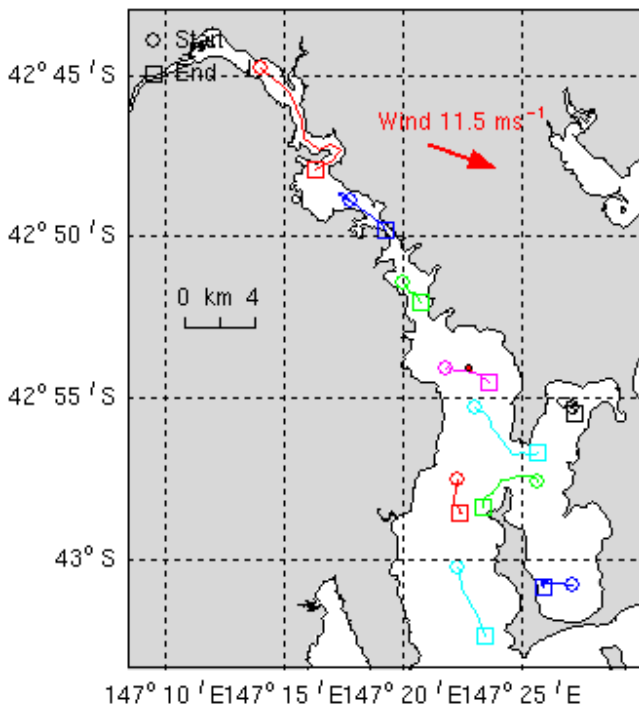
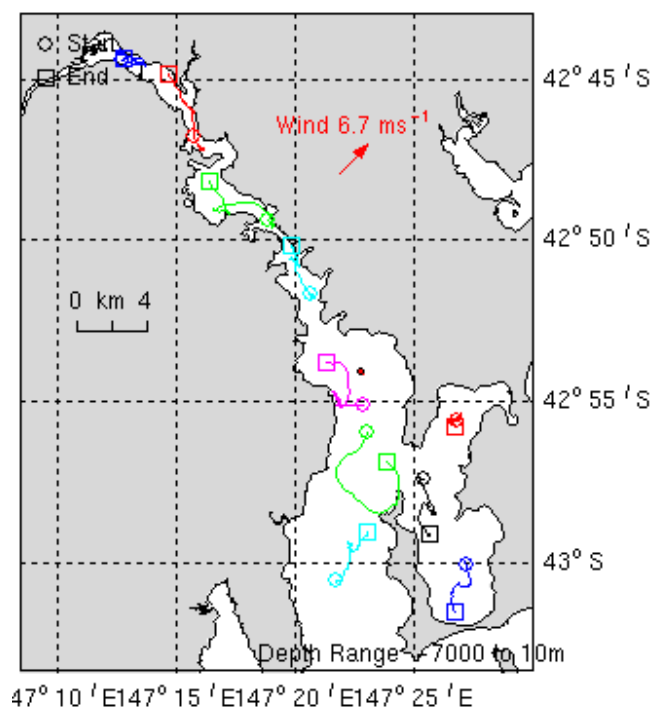


Figure 7.6.11 : Dec 27
 Low flow conditions ($\sim 30 \text{ m}^3\text{s}^{-1}$)
 Flood tide (range $\sim 1.1\text{m}$)



8. Conclusions

A 3D primitive equation model was applied to the Derwent Estuary to examine the hydrodynamics of the region. Using a nesting process the region was represented with high resolution while incorporating forcing due to wind stress, tides, low frequency sea level oscillations and pressure gradients due to temperature and salinity distributions. Major forcing consists of river flow, which may approach $200 \text{ m}^3\text{s}^{-1}$, wind which had a mean speed of 6.7 ms^{-1} from the south west over the simulation period and tide which had a range of $\sim 1\text{m}$ during the spring tide. The period Dec 17 2003 to March 11 2004 was simulated and calibrated to data collected during the project.

Temperature and salinity (T/S) data was collected at the mouth of the estuary (Iron Pot) at the surface on either side of the estuary and the bottom. These data were used to force the seaward open boundary in the model. Additionally an ADCP and CTD were deployed at 4 sites at the bottom along the length of the estuary (Iron Pot, Sandy Bay, Elwick Bay and Bridgewater) and these data formed the basis of model calibration. The salinity and temperature data from Elwick Bay and Bridgewater exhibited a large oscillation at the tidal period, where salinities and temperature near the bottom varied by as much as 20 psu and 2°C respectively, becoming fresher and warmer on the ebb tide. This effect was most pronounced on the spring tide and was diminished closer to the river bed. Comparison of the T/S data from the 4 sites showed the river becomes fresher and warmer with more variability observed in the salinity towards Bridgewater. At Iron Pot bottom water is colder and saltier than surface water and variability is observed between the western and eastern sides of the estuary. The ADCP revealed that tidal currents of several 10s of centimeters occur at Elwick Bay and strong currents of up to $\sim 0.5 \text{ ms}^{-1}$ occur at Bridgewater.

The length of the record of collected data effectively set the period the model could be simulated, although monthly temperature and salinity samples collected by DPIWE were used as boundary conditions to produce a simulation of 15 months duration with a slight loss in accuracy of the model in the lower estuary. The calibration procedure highlighted several physical processes that the model proved sensitive to. Surface heat fluxes played a crucial role in regulating temperature in the region. The salt wedge propagation was sensitive to the depth of the main channel in the upper estuary. Background vertical viscosity and horizontal mixing impacted both stability and accuracy of the solutions.

The model results confirm that the Derwent Estuary behaves as a salt wedge estuary with marine flow in bottom waters directed upstream in the estuary and a fresh water surface flow heading downstream. The head of the salt wedge is located above Bridgewater under low flow and is pushed downstream under high flow conditions. Surface salinities may be less than 20 psu in the lower estuary under high flow. On diurnal timescales the tidal flow dominates the region, with flow directed up-river during the flood tide, and vice versa during the ebb. Under low flow conditions a surface reversal of the currents is seen in the upper and middle estuary during the tidal period but this is absent under high flow since the river discharge overwhelms the tidal flow. The Derwent Estuary is micro-tidal with tidal range $\sim 1\text{m}$ and having diurnal mixed character with a form factor of ~ 1.5 (i.e. the tide is a mixture of diurnal and semi-diurnal). The tide undergoes a neap-spring cycle of ~ 14 days. Tidal excursions in the estuary are variable in time and space, with an average of $\sim 4\text{km}$ and with excursions reaching double this value under favourable wind and river flow conditions. The tide is asymmetrical with ebb tide shorter and associated with stronger currents than the flood. On the stronger ebb tide the pycnocline underwent vertical displacement that lead to the observed large salinity fluctuation near the bottom. It is hypothesized that this displacement is the result of advection due to secondary cross-river circulations enhanced by a compound bathymetry and river curvature. Due to the large diurnal variability of the density structure, an instantaneous snapshot of the salt wedge at any given time may not be representative of the average salinity distribution of the system. Also, interpretation of a salinity snapshot sampled over a period of time comparable to the tidal cycle may be difficult due to aliasing.

The mean flow over a neap-spring cycle exhibits downstream flow at the surface with magnitudes less than 0.2 ms^{-1} and up-estuary flow at the bottom with magnitudes less than 0.05 ms^{-1} . The surface flow appears to favour the eastern bank of the river in the lower estuary. Surface mean flow is into Ralphs Bay, while bottom mean flow is generally out of the Bay. A cyclonic gyre is observed at the bottom in the vicinity of Howrah in the lower estuary. The mean flow over the spring tidal cycle is similar to the long term mean but having a more pronounced gyre occupying the channel off Howrah. This gyre is absent at the bottom and appears at the surface when mean neap tidal flow is observed, and outflow from Ralphs Bay appears stronger during mean neap flow than mean spring tide flow.

Analysis of the balance of forces indicates that, at any given place and time, motion in the estuary is driven predominantly by tide and density effects. The mean flow is a balance between density forcing and Coriolis where the salt wedge is driven up-estuary in the bottom layers by density forcing. Water is entrained into the surface layer along its length where it returns down-estuary. These flows are balanced by the Coriolis force. Bottom friction acts to retard the flow near the bottom, and at the surface the wind contributes a mean westerly component. The non linear components show no coherent pattern and are small except for isolated locations in the estuary where become locally important in perturbing the stratified structure.

The calculation of flushing times can be subjective depending on the method used to compute the flushing. Using an e-folding rate based on depletion of total mass in a region the flushing times varied from less than 1 day for many of the side bays to ~11 days for the whole domain. A flushing estimate for the whole domain based on the average time for neutrally buoyant particles to exit the domain was computed as ~12 days.

Statistical representations of surface distributions of passive tracers resulting from releases at various locations in the estuary generally showed a mixing zone of high concentration with lower concentration throughout the remaining estuary, although there were exceptions. Tracers released in surface waters resulted in distributions of higher concentration, predominantly downstream of the release site. Tracers released in bottom waters generally impacted much of the surface estuary waters. Due to computational constraints statistics of distributions in sub-surface waters was not attempted, but it is anticipated that the bottom releases would be associated with larger concentrations at depth.

Particle tracking analysis was performed where particles were released from the same sites as were the passive tracers. Particles were fairly evenly distributed throughout the whole estuary from each release site, indicating the estuary is reasonably well connected. Particles released in the salt wedge in deeper water were more evenly distributed throughout the domain in comparison to those released in surface waters, whose distributions were predominantly confined to downstream from the source (consistent with motion expected due to the residual flow). Release sites in the vicinity of the Tasman Bridge resulted in more uniform distribution of particles throughout the middle and lower estuary than release sites in the lower estuary. The most uniform particle distributions resulted from the bottom Zinifex release site and the Boyer release site in the upper estuary. The mean age of all particles released from all sites to exit the domain was comparable to the $56 \text{ m}^3\text{s}^{-1}$ flow whole-estuary flushing estimate (11.7 days). Particle trajectories followed the diurnal tidal forcing, with particles exhibiting up-estuary movement on the flood tide, and down-estuary on the ebb, except in the upper and middle estuary under high flow conditions when particle trajectories were oriented down-estuary on both flood and ebb tide.

9. References

- Cartwright, D.E. and R.D. Ray (1990)** Oceanic tides from Geosat altimetry. *J. Geophys. Res.*, 95 C3, 3069-3090.
- Dyer, K.R. (1997)** Estuaries, a physical introduction. *J. Wiley & Sons, Chichester.*
- Farmer, H.G. and G. W. Morgan (1953)** The salt wedge. In: *Proceedings of the 3rd conference on coastal engineering*, ASCE, Washington DC, 54 – 64.
- Gill, A. E. (1982)** Atmosphere-Ocean Dynamics. *Academic Press Inc.*
- Green, G. and C. Coughanowr (2003)** State of the Derwent Estuary 2003: a review of pollution sources, loads and environmental quality data from 1997 – 2003. Derwent Estuary Program, DPIWE, Tasmania.
- Ippen, A.T. and D.R.F. Harleman (1961)** One dimensional analysis of salinity intrusion in estuaries. *Tech. Bull. 5*, Comm. Tidal Hydraul. Corps Eng. US Army.
- Keulegan, G.H. (1966)** The mechanism of an arrested saline wedge. In *Estuary and coastline hydrodynamics*, Ed. T. Ippen. McGraw-Hill, New York, 744pp.
- Kondo, J. (1975)** Air-sea bulk transfer coefficients in diabatic conditions. *Boundary-Layer Meteorology*, **9**, 91-112.
- Leonard, B.P. (1979)** A stable and accurate convective modelling procedure based on quadratic upstream interpolation. *Computer methods in applied Mech. and Eng.*, **19**, 59 – 98.
- Leonard, B.P. (1991)** The ULTIMATE conservative difference scheme applied to unsteady one-dimensional advection. *Comp. Methods in Appl. Mech. and Eng.*, **19**, 17 – 74.
- Mellor, G.L. and T. Yamada (1982)** development of a turbulence closure model for geophysical fluid problems. *Rev. Geophys.*, **20**, 851 – 875.
- Prandle, D (1981)** Salinity intrusion in estuaries. *J. Phys. Oceanogr.*, **11**, 1311 – 1324.
- Prandle, D. (1985)** On salinity regimes and the vertical structure of residual flows in narrow tidal estuaries. *Estuarine, Coastal and Shelf Science*, **20**, 615 – 635.
- Ridgway K. R., J. R. Dunn and J. L. Wilkin (2002)** Ocean interpolation by four-dimensional least squares -Application to the waters around Australia, *J. Atmos. Ocean. Tech.*, **19**, 1357-1375.
- Tompson, J. D. and J. S. Godfrey (1985)** Circulation dynamics in the Derwent Estuary. *Aust. J. Mar. Freshw. Res.*, **36**, 765 – 772.
- Umlauf, L., H. Burchard and K. Hutter (2003)** Extending the k- ω turbulence model towards oceanic applications. *Ocean Modelling*, **5**, 195 – 218.
- Walker, S.J. and Waring, J.R., (1998)** A multiple grid, 3-dimensional, non-linear, variable-density hydrodynamic model with curvilinear horizontal coordinates and level (z) vertical coordinates, CSIRO Marine Research, Report OMR-118/120.